Indexing Cerebrovascular Health Using Near-Infrared Spectroscopy: A Multi-Model Analysis

Rashid Ghorbani Afkhami
MSc (Electrical Engineering)

A thesis submitted in fulfilment of the requirements for the degree of

Doctor of Philosophy

School of Electrical Engineering and Computing
The University of Newcastle, Australia

July 2020

This research is supported by an Australian Government Research Training Program (RTP) Scholarship

Statement of Originality

I hereby certify that the work embodied in the thesis is my own work, conducted under normal supervision. The thesis contains no material which has been accepted, or is being examined, for the award of any other degree or diploma in any university or other tertiary institution and, to the best of my knowledge and belief, contains no material previously published or written by another person, except where due reference has been made. I give consent to the final version of my thesis being made available worldwide when deposited in the University's Digital Repository, subject to the provisions of the Copyright Act 1968 and any approved embargo.

Rashid Ghorbani Afkhami

Abstract

Cerebrovascular health is of great concern, especially in the ageing population, as stiff vessels are linked with diseases such as stroke, dementia, and age-related disabilities. Data from brain imaging techniques, including magnetic resonance imaging (MRI) and transcranial Doppler ultrasound (TCD), can be used to infer information regarding the health of underlying arteries. Such health assessments are commonly based on an index that is dependent on the properties of the device and can be related to known vascular health factors by a mathematical model.

The contribution of this thesis to the field of cerebrovascular health and brain imaging is twofold: First, we develop a timing index (TI) as a measure of cerebrovascular health. The relationship between TI and vascular health factors is derived in the context of pressure waveforms using transmission line theory and Windkessel model models. The proposed formula for TI matches data reported in the literature and helps to understand the flattening behaviour observed in the arrival time of reflected waves in aged subjects. Using similar mathematical modelling we also derive an expression for the relationship between the existing augmentation index (AI) and the same vascular health factors. Together with existing pulsatility index (PI) results, we show mathematically that TI is potentially more strongly related to vessel stiffness than either of the two indices currently used to index cerebrovascular health i.e., PI and AI. This is particularly so in younger to middle-aged subjects where interventions are best applied. We then show that TI can be applied to TCD measurements of blood flow velocity. To our knowledge, this is the first use of wave reflection time to measure vascular health in the brain. Transcranial Doppler Ultrasound Timing Index ($\mathrm{TI_{TCD}}$) shows a significant correlation with age. Furthermore, compared to the existing transcranial Doppler augmentation index ($\mathrm{AI_{TCD}}$) and transcranial Doppler pulsatility index ($\mathrm{PI_{TCD}}$), the $\mathrm{TI_{TCD}}$ show stronger correlations with cardiorespiratory fitness and the magnetic resonance imaging pulsatility index ($\mathrm{PI_{MRI}}$).

The second contribution of this thesis is in its application of near-infrared spectroscopy (NiRS). Firstly, we propose a NiRS signal model capable of producing synthetic NiRS signals comprising low-frequency components, arterial pulsation signals, reflected waves, Mayer and respiratory waves and a haemodynamic response function. The model outputs are compared with measured NiRS signals, and it is shown that the modelled signal is equivalent to the recorded signal as a later set of recordings on the same channel. Then, as an emerging tool for measuring cerebrovascular health, we propose a novel algorithm for locating systolic and reflected peaks on an averaged NiRS signal, thereby applying the TI to NiRS. The new near-infrared spectroscopy timing index ($\mathrm{TI_{NiRS}}$)

shows stronger correlations with age, cardiorespiratory fitness (CRF) and PI_{MRI} than the pulse relaxation function (PReFx) which is an existing NiRS-based vascular health index.

Compared with existing brain imaging techniques, NiRS offers several advantages, such as being inexpensive, portable and easy-to-use. The NiRS-related contributions of this thesis are the development of a NiRS signal model and a NiRS-based cerebrovascular health measure. These will help in the development of a technique for the routine clinical measurement of cerebrovascular health. Such a technique would facilitate early intervention in the progression of vascular stiffness with age and, potentially, vascular-related diseases such as stroke and dementia.

Acknowledgements

First, I would like to thank my supervisor, Professor Sarah Johnson, for her continuous support and guidance throughout my PhD. Her availability despite a busy schedule and her comments and brilliant ideas made this thesis possible.

I would like to extend my thanks to my co-supervisors Professor Rohan Walker and Associate Professor Saadallah Ramadan for their support and insight. Special thanks to Dr Rachel Wong for her detailed comments on the papers.

It should be mentioned that this thesis would not have been possible without the volunteers who participated in the study. I must also express my appreciation to Hamish Evans, Shiami Luchow, Kristen Fisher and Jillian Mason for their help in data collection and recruitment.

Last but not least, I thank my wife Safa for her unconditional love and support during my PhD and the sacrifices she made to be with me on this journey. I also want to thank our family and all our friends who made this wonderful experience in Australia possible for us.

Contents

List of Figures

List of Tables

Abbreviations

AHA	American Heart Association
AI	Augmentation Index
$\mathbf{AI_{TCD}}$	Transcranial Doppler Augmentation Index
$\mathbf{AI^*}$	Augmentation Index, Alternative Definition
AP	Arterial Pulsation
ASL	Arterial Spin Labelling
ba-PWV	Brachial-ankle Pulse Wave Velocity
bf-PWV	Brachial-femoral Pulse Wave Velocity
BOLD	Blood-oxygenation Level Dependent
bpm	Beats Per Minute
BR	Breathing Rate
CBF	Cerebral Blood Flow
cf-PWV	Carotid-femoral Pulse Wave Velocity
CFEn	Cross-fuzzy Entropy
CPP	Cerebral Perfusion Pressure
CRF	Cardiorespiratory Fitness
CSF	Cerebrospinal Fluid
CVR	Cerebrovascular Resistance
DC	Direct Current
DCS	Diffuse Correlation Spectroscopy
ECG	Electrocardiography
EEG	Electroencephalography
fMRI	Functional Magnetic Resonance Imaging
HR	Heart Rate
HRF	Haemodynamic Response Function
ICP	Intracranial Pressure
IIR	Infinite Impulse Response
LF	Low-frequency
MAP	Mean Arterial Pressure
MBP	Mean Blood Pressure
MCA	Middle Cerebral Artery

MRI	Magnetic Resonance Imaging
NiR	Near-infrared
NiRS	Near-infrared Spectroscopy
PC	Phase Contrast
PI	Pulsatility Index
$\mathbf{PI_{MRI}}$	Magnetic Resonance Imaging Pulsatility Index
$\mathbf{PI_{TCD}}$	Transcranial Doppler Pulsatility Index
$\mathbf{PI^{*}{}_{TCD}}$	Transcranial Doppler Pulsatility Index, Alternative Definition
PP	Pulse Pressure
PReFx	Pulse Relaxation Function
PWV	Pulse Wave Velocity
SNR	Signal-to-noise Ratio
std	Standard Deviation
SVD	Small Vessel Disease
$\mathbf{T_{refl}}$	Reflection Time
TCD	Transcranial Doppler Ultrasound
TI	Timing Index
$\mathbf{TI_{NiRS}}$	Near-infrared Spectroscopy Timing Index
$\mathbf{TI_{TCD}}$	Transcranial Doppler Ultrasound Timing Index
TL	Transmission Line
TOST	Two One-sided T-tests
TPR	Total Peripheral Resistance
VLF	Very Low Frequency
WGN	White Gaussian Noise
WK	Windkessel Model
WK2	Two-element Windkessel Model
WK3	Three-element Windkessel Model
WK4	Four-element Windkessel Model

Symbols

Symbol	*Definition*	*Units*
C	Compliance	m^3/Pa
P	Pressure	Pa (1 Pa $\approx$ 1/133 mmHg, or N/m^2)
Q	Flow	m^3/s ($1m^3/s = 10^3 l/s$)
R	Resistance	Pa/m^3
V	Velocity	m/s
$\mathcal{V}$	Volume	m^3 ($1m^3 = 10^3 l$)
Z	Impedance	Pa/m^3
β	Phase Constant	rad/m
Γ	Reflection Coefficient	unitless
γ	Propagation Constant	rad/m
ω	Angular Velocity	rad/s

Chapter 1

Introduction

1.1 Problem Statement & Motivation

In the human body, the arteries have the vital task of carrying oxygenated blood from the heart toward arterioles and capillaries, which supply nutrition to cells around the body. While the blood pressure at the beginning of the arterial system; i.e., the left ventricle, is highly pulsatile, the arteries smooth out this pressure to protect downstream arterioles and capillaries. Arteries stretch during systole, when high-pressure blood is forced from the left ventricle, and recoil during diastole, when the heart is resting, which damps fluctuations in blood pressure. This ability of the arteries is referred to as *compliance*. Arteries lose their compliance and become stiffer with low physical activity [1] and with ageing even in the absence of other vascular disease or risk factors [2]. Arterial stiffening is an important risk factor in cardiovascular mortality [3] and the European guidelines for managing arterial hypertension recommend arterial stiffness measurement to evaluate target organ damage [4].

Cerebrovascular diseases were categorized as the fifth most common cause of death in the United States in 2017 [5], and lead to cognitive impairment, stroke and dementia. Stiffening of cerebral arteries which is an inevitable consequence of ageing [2], contributes to compromised cerebrovascular health by increasing pressure fluctuations and, therefore, damaging arterial wall structures over time [6].

Measuring vascular health is especially difficult inside the brain, which is enclosed by the skull and floats in cerebrospinal fluid (CSF). Currently accepted technologies for the assessment of cerebrovascular health are magnetic resonance imaging (MRI) and transcranial Doppler ultrasound (TCD), which can either measure compliance or produce a vascular health index. Among them, MRI has relatively poor temporal resolution and is costly and time consuming to use for simple and routine monitoring of vascular health in the general population. Meanwhile, TCD is criticized for being highly operator-dependent and unable to be used with up to one-fifth of the population due

to temporal bone thickness [7–9]. In addition to the technological difficulties inherent in these devices, a commonly accepted measure of cerebrovascular health is lacking. Instead, various indices are proposed for each device without a clear explanation of their connection to vascular health factors.

Near-infrared Spectroscopy (NiRS) is a relatively new technology that measures regional blood volume changes through the absorption of near-infrared (NiR) light, mainly by oxygenated blood inside cerebral arteries [10, 11]. NiRS offers high temporal resolution and is sufficiently sensitive to detect changes in blood volume during cardiac cycles. Therefore, NiRS allows local studies of cerebrovascular behaviour and possible assessment of cerebrovascular health [10].

In this thesis, first, we aim to clarify the relationships between commonly used indices and vascular properties using mathematical models. Although correlations between such indices and health factors are frequently reported in the literature, we believe that the true relationship between these indices and blood and vascular haemodynamics are more complex. Nonetheless, formulating the commonly used indices will help us explain how these indices change with age and other health indicators and also help us define a new index more suitable for the NiRS. We hypothesize that a timing-based index is a strong cerebrovascular health indicator. A pure timing index is in particular practical for NiRS signals they tend to be heavily affected by noise and have incomparable intensities across channels. Therefore, we propose a new timing index (TI) by studying pressure waveforms and showing that TI is related to vascular health factors. Then, we test our hypothesis using blood flow velocity data and showing TI correlation with age and other health indicators. Finally, we extend the application of the proposed index to assessment of cerebrovascular health using NiRS. Using experimental NiRS data we mathematically model NiRS signals and then assess the performance of a NiRS-based TI for estimating cerebrovascular health.

1.2 Thesis Outline and Contributions

The thesis is organized into the following chapters: background, a mathematical model of wave reflection, indexing cerebrovascular health using TCD, a mathematical model of the NiRS signal, indexing cerebrovascular health using NiRS, and conclusions and future research directions. Here, we will have an overview and the contributions of each chapter and related publications and conference presentations (see Section 1.2.1 for the list of references used in this section).

Chapter 2 provides an extensive literature review of vascular health indicators, mathematical models of the vascular system, devices used for the assessment of vascular health and current indices and measures of vascular health.

In Chapter 3, we use a transmission line (TL) and a Windkessel model (WK) to simulate blood waveform propagation and derive a mathematical expression for the reflection time (T_{refl}), which is the time it takes for the blood wave to reach a bifurcation site (or anywhere that reflection may happen), reflect back and hit the forward travelling wave. We next derive a mathematical expression for the augmentation index, a commonly used pressure and flow velocity health index. The derived formulas are then successfully applied to data from the literature and the results confirm the dependency of both indices on the vascular ageing indicators such as compliance, pulse wave velocity (PWV) and systemic vascular resistance. Finally, we use the new mathematical expressions to interpret commonly observed trends in T_{refl} and AI, such as the flattening with age, changes with heart rate and the phenomenon known as "distal movement of the reflected site". The main contribution of this chapter is the mathematical expressions derived for T_{refl} and AI and their benefit in explaining commonly observed experimental phenomena. Part of the material in this chapter is published in [J2].

The model developed in Chapter 3 motivated us in proposing a new timing-based index of cerebrovascular compliance. Based on our modelling in Chapter 3, we hypothesize the new TI, which is the inverse of T_{refl}, is strongly related to the vascular health factors effected by CRF. In Chapter 4, this hypothesis is tested using two sets of experimental data of TCD blood flow velocity waveforms collected in a healthy adult population. The experimental results show that TI_{TCD} has a stronger correlation with cardiorespiratory fitness (CRF) than the existing AI_{TCD} and PI_{TCD}. We also make note that PI_{TCD} as the most commonly used TCD index, should be interpreted with caution due to its complex relationships with cerebrovascular resistance (CVR) and vascular stiffness. This is because each of these components has opposite effects on this index, resulting in PI_{TCD} having a weak correlation with age and no correlation with CRF. The main contribution of this chapter is the proposed TCD-based vascular health index, TI_{TCD} which is shown experimentally to have several advantages over the existing TCD-based indices of vascular health. The material in this chapter is published in [J3] with preliminary results presented in [P2].

Moving towards the goal of estimating cerebrovascular health using NiRS, in Chapter 5 we propose a mathematical model for NiRS signal which is capable of producing synthetic data. The model includes all the known elements of the NiRS signal such as low-frequency (LF) components, arterial pulsation (AP) signals, reflected waves, and Mayer and respiratory waves and can be used to provide ground-truth NiRS signals to facilitate the assessment of new and existing NiRS signal processing algorithms. More importantly, the proposed model can help to better understand the components of NiRS signals with the aim of designing a new NiRS-based cerebrovascular health index. The accuracy of the model is assessed using the cross-fuzzy entropy (CFEn) measure, which indicates high similarity between the synthetic and in vivo data. The model is then

used to assess TI and AI changes with age and HR. Later in this chapter, we propose a NiRS peak-detection algorithm and use the model to examine the effects of system parameters on the accuracy of the algorithm. The main contribution of this chapter is the new mathematical model of the NiRS signal and the new NiRS peak-detection algorithm. A preliminary version of the model is published in a conference proceedings [C1] and the final version is published in [J1].

In Chapter 6 we propose a TI measure of cerebrovascular health for NiRS called $\mathrm{TI}_{\mathrm{NiRS}}$, which builds on the success of $\mathrm{TI}_{\mathrm{TCD}}$ (Chapter 4) and the peak-detection algorithm derived in Chapter 5. We hypothesize that $\mathrm{TI}_{\mathrm{NiRS}}$, similar to $\mathrm{TI}_{\mathrm{TCD}}$, is an indicator of cerebrovascular health. Then, using in vivo data we show that $\mathrm{TI}_{\mathrm{NiRS}}$ correlates significantly with age, CRF and other cerebrovascular health indices derived from TCD and MRI data, indicating it has high performance in tracking changes in the cerebrovascular system. The $\mathrm{TI}_{\mathrm{NiRS}}$ offers a potentially valuable means of indexing vascular health and has superior cost, portability and widespread implementation potential compared with existing techniques. The main contribution of this chapter is the experimental validation of the proposed NiRS vascular health index, $\mathrm{TI}_{\mathrm{NiRS}}$. The material in this chapter is published in [J4] while some of the material covering the application of the existing PReFx index to the current data is presented in [P1] and [P3].

Conclusions and a discussion of future work are provided in Chapter 7.

1.2.1 Publications

Journal Publications

[J1] R. G. Afkhami, F. R. Walker, S. Ramadan, and S. J. Johnson, "A Dynamic Model of Brain Hemodynamics in Near-infrared Spectroscopy," *IEEE Transactions on Biomedical Engineering*, 2019; 67(6) 2103–2109.

[J2] R. G. Afkhami and S. J. Johnson, "Wave reflection: More Than A "Round Trip"," *medRxiv*, 2020. doi: 10.1101/2020.03.30.20048223. Submitted to *Medical Engineering & Physics*.

[J3] R. G. Afkhami, R. Wong, S. Ramadan, F. R. Walker, and S. J. Johnson, "Indexing Cerebrovascular Health Using Transcranial Doppler Ultrasound," *Ultrasound in Medicine & Biology*, 2021; doi: https://doi.org/10.1016/j.ultrasmedbio.2020.12.022.

[J4] R. G. Afkhami, F. R. Walker, S. Ramdan, R. Wong, and S. J. Johnson, "Indexing Cerebrovascular Health Using Near-infrared Spectroscopy," Submitted to *Scientific Reports*, 2020.

Conference Proceedings

[C1] R. G. Afkhami, K. Low, F. R. Walker, S. J. Johnson, "A Dynamic Model of Synthetic Resting-state Brain Hemodynamics," In *26th European Signal Processing Conference*, Rome Italy, Sep. 2018, pp. 96–100.

Other Conference Presentations

[P1] R. G. Afkhami, H. Evans, R. Wong, F. R. Walker, S. Ramadan, K. Low, and S. J. Johnson, "Assessment of NIR Pulse Relaxation Function (PReFx)," In *19th International Council for NIR Spectroscopy Meeting, NIR2019*, Gold Coast Australia, Sep. 2019.

[P2] R. G. Afkhami, S. J. Johnson, R. Wong, S. Ramdan, and F. R. Walker, "An Investigation of Transcranial Doppler Ultrasound Techniques to Measure Cerebrovascular Compliance," In *The Australian chapter of the Organization of Human Brain Mapping (OHBM)*, Newcastle Australia, Oct. 2019.

[P3] R. G. Afkhami, S. J. Johnson, S. Ramdan, and F. R. Walker, "An Investigation of Near-infrared Brain Imaging Techniques to Measure Cerebrovascular Compliance," In *The Australian chapter of the Organization of Human Brain Mapping (OHBM)*, Newcastle Australia, Oct. 2019.

Chapter 2

Background

In this chapter, we first provide a concise medical overview of the structure and functioning of the vascular system and define vascular compliance, resistance and pulse wave velocity. Then, we review mathematical models of the vascular system, imaging technologies and current approaches to measuring arterial stiffness and indexing arterial health.

2.1 Biological Viewpoint

As we know, the heart is the main organ of the cardiovascular system, pumping blood repeatedly throughout the entire body. Each cardiac cycle has a relaxation phase, or *diastole*, which starts with the closure of the aortic valve. During diastole, the heart fills with blood. The diastole is followed by a contraction phase, or *systole*, which starts with the closure of the Mitral valve (connecting the left atrium to the left ventricle) and continues by ventricle ejection, sending out the blood to the aorta and lungs. Figure 2.1 shows the change in aortic pressure during a single cardiac cycle. Large arteries carry blood away from the heart and along the way, the arteries branch into smaller and smaller vessels until they become microscopic arteries called *arterioles*, which provide the main vascular resistance to blood flow. After the arterioles, blood enters the *capillaries*, which are only 5-10µm in diameter and connect the arterioles to the *venules*. Capillaries and small post-capillary venules are the main sites of exchange of water, oxygen and other nutrients. The de-oxygenated blood is then carried back to the heart by the *veins*.

2.1.1 Vascular Resistance & Compliance

Blood vessels, depending on their characteristics, offer a kind of resistance to the blood flow. This phenomenon can be formulated by Poiseuille's law [12], which shows that the resistance is inversely proportional to the 4th power of vessel radius. Total Peripheral

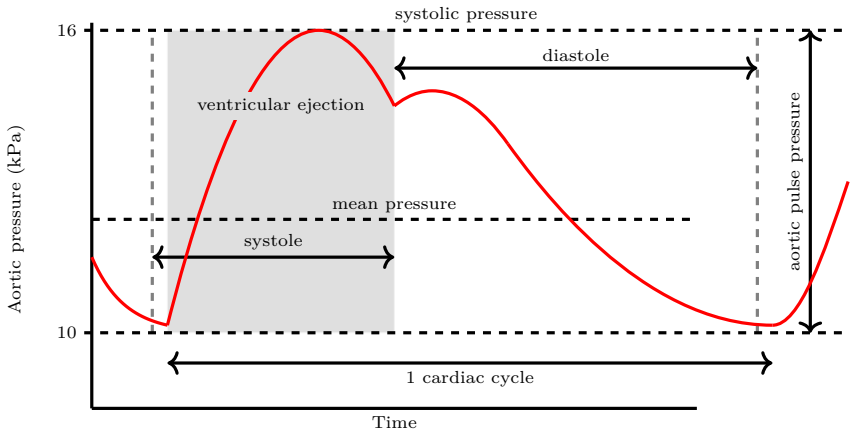

FIGURE 2.1: Aortic pressure wave during one cardiac cycle of systole and diastole

Resistance (TPR), also known as systemic vascular resistance, is the resistance of the entire circulatory system to the blood flow.

Arteries and veins have the ability to expand and contract with changes in pressure; this feature of the blood vessels is measured in terms of *stiffness* or *compliance*. Compliance is especially important in the larger arteries and helps regulate highly pulsatile blood pressure before blood reaches the small arteries and arterioles. Compliance (C) is inversely proportional to stiffness and is defined as changes in the blood volume ($\mathcal{V}$) for a given change in pressure (P) that is,

$$C = \frac{d\mathcal{V}}{dP}. \tag{2.1}$$

Compliance is expressed in $\mathrm{cm}^3\,\mathrm{kPa}^{-1}$. Calculating C is difficult because even if one injects a known volume of blood into the arterial system, the losses of blood in the periphery are unknown. Therefore, several methods for estimating compliance have been proposed in the literature. Higher compliance for a blood vessel means that it deforms more easily when pressure is applied, in that sense, compliance of the veins is around twenty times higher than that of arteries [13].

It is known that both vascular resistance and vascular compliance change with age [14, 15]. Even with no underlying disease, ageing itself is associated with structural and functional changes in the cardiovascular system [16]; specifically, a reduction in the elastic component and increase in the inelastic (collagen) component of the arterial wall [15]. TPR increases slightly with age which, in part, elevates arterial stiffening [16].

2.1.2 Pulse Wave Velocity

Pulse Wave Velocity (PWV) is the speed of the blood waves and is measured in $\mathrm{m\,s}^{-1}$. It is known for its strong association with stiffness, and the carotid-femoral pulse wave velocity (cf-PWV) is considered to be the gold standard for measuring aortic stiffness

[4, 15]. PWV is inversely proportional to arterial radius and, as arteries lose their stiffness, the PWV increases. PWV is commonly measured by applanation tonometry, which uses a high-fidelity strain gauge pressure transducer to record pressure waveforms from common carotid, brachial or femoral arteries. Often, a transfer function is used to estimate pressure in the aorta. The Cf-PWV is considered the gold standard for measuring arterial stiffness [15], whereas other PWV measures, such as brachial-ankle pulse wave velocity (ba-PWV) and brachial-femoral pulse wave velocity (bf-PWV) are also commonly reported in the literature. It has been shown that PWV is inversely proportional to the square root of total arterial compliance [17] and changes positively with vascular resistance [18]. The relationship of PWV with the structural properties of the arterial system, such as compliance and resistance, makes it ideal for tracking vascular health. This is due to the fact that although health related structural changes in the arteries are well-known, direct measurement of vascular compliance or resistance is not readily feasible.

The PWV is closely related to the concept of wave reflection. It is known that after a blood wave travelling from the heart hits vascular bifurcation points, a portion of the wave reflects back towards the heart eventually augmenting the incident waveform. In a healthy vascular system where PWV is low, both incident and reflected waves travel at low speed and, therefore, the reflected wave joins the incident wave later during the diastole, thereby decreasing the pulse pressure (PP). However, with increased PWV, the augmentation of the two waveforms occurs in late systole, increasing the systolic pressure and PP and putting arterial walls under stress. Based on the location of measurement, the pressure waveform can have two distinct peaks for the systole and the reflected wave or either peaks might be in the form of an inflection point (see Fig. 2.2). Hence, analysing the time of occurrence of the systolic and reflected peaks and the start of the systolic phase can provide indications of PWV and vascular health [2, 19].

2.1.3 Vascular Resistance & Compliance in The Brain

Age related changes in vascular structure are of great importance especially in the brain where elevated cerebrovascular stiffness can lead to vessel damage called *small vessel disease (SVD)* that can lead to cognitive decline and Alzheimer's disease [20]. Nonetheless, the impracticality of measuring cerebral haemodynamics like blood flow, blood pressure or vascular wall properties makes it difficult for scientists to validate methods of estimating cerebrovascular compliance.

In our body, elastic arterial walls have a storage mechanism for flow pulsatility, converting pulsatile arterial blood flow to steady peripheral flow. The brain, however, is enclosed in a rigid container and any pulsation from the arterial walls is felt immediately everywhere throughout the cranium. The overall compliance of the cerebral

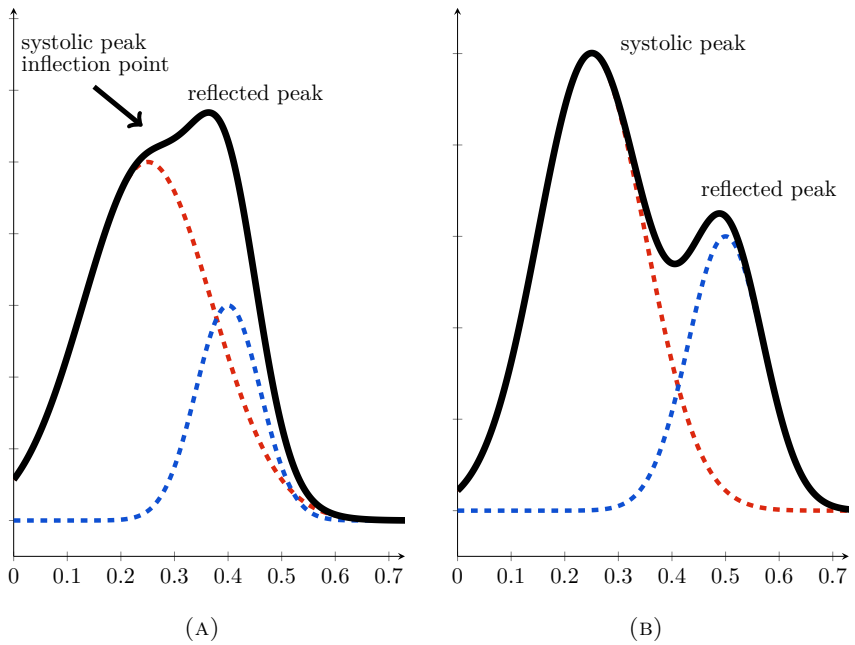

FIGURE 2.2: Sample (a) aorta and (b) radial pressure waveforms (simulated). Red lines represents incident waves and blue lines represent reflected waves.

arteries provides a steady blood supply for the brain [21]. As the most complicated part of the human body, the brain needs a massive blood supply which is provided by two pairs of arteries the internal carotid arteries and the vertebral arteries. These four arteries deliver around $12.5\,\mathrm{ml\,s^{-1}}$ of blood to the brain [22]. After supplying the brain with oxygen and nutrients, de-oxygenated blood finds its way to the heart through the veins. The brain is surrounded by the cranium, which is filled with an incompressible fluid called *cerebrospinal fluid (CSF)*. The CSF is produced in cerebral ventricles and is found in the brain and spinal cord. In adults, the CSF volume is typically 125-150ml and is produced at a rate of $25\,\mathrm{ml\,h^{-1}}$ [23]. The CSF helps reduce the effective brain weight from 1500g to 50g, allowing the brain to maintain its density without being damaged by its own weight, and also acts as a shock absorber. Besides, it provides a medium for transferring nutrients and waste products to and from the brain tissue. After circulation, CSF is reabsorbed in the suer sagittal sinus [23, 24]. The pressure inside the cranium is called the *intracranial pressure (ICP)* and ranges between 1kPa and 2kPa in healthy adults in a lying position. Other than its clinical importance, the ICP controls the *cerebral perfusion pressure (CPP)*, which is defined as:

$$\mathrm{CPP} = \mathrm{MAP} - \mathrm{ICP} \tag{2.2}$$

where MAP is the *mean arterial pressure*. The CPP is the pressure gradient that causes blood flow to the brain at a rate of:

$$\mathrm{CBF} = \mathrm{CPP}/\mathrm{CVR}. \tag{2.3}$$

In which CBF is the cerebral blood flow and CVR is the cerebrovascular resistance. The Monro-Kellie hypothesis states that the brain is surrounded by a non-expandable bone, the brain tissue is nearly incompressible and the volume inside the cranium is constant. Therefore, the total volume of the cranial elements, blood (arterial and venous blood volumes, i.e., $\mathcal{V}_{\mathrm{a}} + \mathcal{V}_{\mathrm{v}}$), brain tissue ($\mathcal{V}_{\mathrm{tiss}}$) and CSF ($\mathcal{V}_{\mathrm{CSF}}$) are fixed and increases in any of them must be compensated for by an equivalent decrease in another, i.e., [22, 25, 26]

$$\frac{d\mathcal{V}_{\mathrm{a}}}{dt} + \frac{d\mathcal{V}_{\mathrm{v}}}{dt} + \frac{d\mathcal{V}_{\mathrm{CSF}}}{dt} + \frac{d\mathcal{V}_{\mathrm{tiss}}}{dt} = 0. \tag{2.4}$$

Both cerebrovascular compliance and the compliance of the CSF space and brain tissue contribute to pulsation absorption, which helps the blood to flow more steadily into the brain. Invasive pressure-volume measurements of the brain show that there is an exponential relationship between ICP and brain volume [21, 26]. Figure 2.3 shows that the pressure pulsatility increases (low compliance) with increasing mean pressure. Under normal physiological conditions (blue area in the figure), the high intracranial compliance allows only small changes in ICP for a given change in volume. However, with elevated ICP levels, the intracranial volume compensatory capacity becomes exhausted and compliance drops, causing huge increases in intracranial pressure with small increases in volume.

As the cerebral arteries become stiffer, the cerebrovascular system loses its ability to cushion the arterial blood pulsations. As a result, highly pulsatile pressure waves reach small arteries and arterioles and, over time, damage arterial walls [27]. This condition is called *small vessel disease (SVD)* which reduces cerebral blood flow and damages the function of the blood-brain barrier, a system that protects the brain from circulating pathogens [27–29]. SVD is a type of age-related loss of brain health causes cognitive decline and non-cognitive disorders [28].

From vascular resistance point of view, compliance of a vessel means it can reduce its resistance by stretching to allow for a smooth pressure change. Age progression builds up collagen fibres in the vascular wall, which increases stiffness and decreases the overall resistance of the vascular system. In addition, ageing causes thickening of arterial walls and reduces the interior arterial cross-sectional area, thus increasing TPR [30]. The age-related changes in vascular resistance are coupled with stiffening of the vessels and increases in PWV [16, 30]. Therefore, the general health of the vascular system is a function of many changes in vascular structure and an index of cerebrovascular health should consider all these factors.

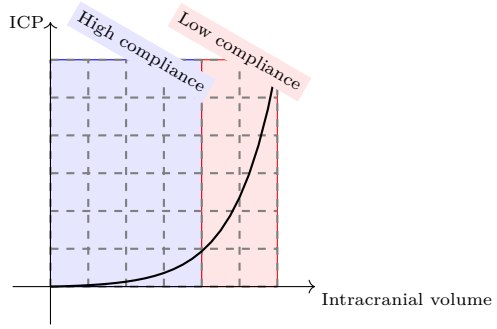

FIGURE 2.3: Relationship between intracranial pressure and volume in the human brain showing regions of high and low compliance

2.2 Mathematical Viewpoint

Here, we review the earliest mathematical models of arteries, called WKs. We examine how they were improved over time and the reasoning behind including the new elements added to them. Then, we cover TL models and see how they make the study of wave reflection possible. Finally, we review existing devices that are used to provide data for brain models, discussing the limitations and advantages of each. In parallel, we highlight existing research gaps in the estimation of cerebral arterial health.

2.2.1 Windkessel Models

Windkessel Models (WKs) are the simplest models used to represent the arterial system by means of electrical elements. TPR can be represented as a resistor, R, and compliance can be represented as a capacitor, C. These sets of arterial models get their name from the well-known WK effect, as large arteries act as elastic reservoirs.

- *Two-element Windkessel Models (WK2s):* Fig. 2.4 shows a WK2 model. R and C represent the total peripheral resistance and total arterial compliance, respectively. The governing equation for the model in Fig. 2.4 is:

$$C\frac{d}{dt}P(t) + \frac{1}{R}P(t) = F(t). \tag{2.5}$$

  In which F is blood flow. During each cardiac cycle, after the aortic valve closes and before ventricular ejection starts (Fig. 2.1), the inflow of blood is zero. Thus,

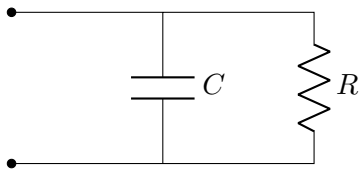

FIGURE 2.4: Schematic diagram of a Two-element Windkessel Model of the circulatory system

for any time during diastole

$$P(t) = P_1 e^{-\frac{(t-t_1)}{RC}}. \tag{2.6}$$

Where (t_1, P_1) is a reference point in the pressure signal during the diastole phase. Equation (2.6) implies that the pressure decreases exponentially during diastole with a time constant, τ, equal to $R \times C$. Therefore, one way of estimating C is to fit the pressure-time signal with an exponential function and find the time constant of decay. Then, TPR is estimated as the mean blood pressure (MBP) over mean flow, and C can be extracted from $\tau = RC$. This method of estimating compliance using a WK2 and exponential fitting is called the *decay time method*.

Another method for estimating C is to apply an integration over (2.5) during diastole [31].

$$C = \frac{1}{R\,(P_1 - P_2)} \int_{t_1}^{t_2} P(t)dt, \tag{2.7}$$

where (t_1, P_1) and (t_2, P_2) are two reference points on the diastolic pressure curve. The method is known as the *area method*.

It has been shown that the WK2 cannot model the high-frequency (>5Hz) features of the pressure wave in the arterial tree. It also cannot describe the model parameters during systole [12]. The input impedance for the WK2 (Fig. 2.4) is

$$Z_{\text{in}} = \frac{R}{1 + j\omega RC}, \tag{2.8}$$

and the modulus and phase of input impedance for the model approach zero and $-90°$, respectively at high frequencies. For measured pressure wave values, however, the input impedance reaches a constant value and the phase hovers around zero at high frequencies [12]. Therefore, the WK2 is only a good predictor of the gross features of the pressure waveform.

The *pulse pressure method* uses the low-frequency (LF) accuracy of the WK2 to get a better estimate of compliance. Pulse pressure is defined as the difference between the systolic and diastolic pressures. The method adjusts C in the model to get the best match between the predicted and measured pulse pressures at a certain point in the arterial tree [31].

- *Three-element Windkessel Models (WK3s):* The shortcomings of WK2 at high frequencies and in describing the pressure-flow relationship in systole led to the introduction of WK3 (Fig. 2.5). Frequency analysis of pressure and flow measurements showed that, at higher frequencies, the impedance module reaches the characteristic impedance of the proximal arteries (i.e., arteries closer to the heart). The third element in the new model, Z_{c}, is this characteristic impedance. However,

large arteries are usually modelled as a lossless TL and therefore, Z_c is replaced by a resistor [12, 32].

The most accepted method of estimating compliance with WK3 is the *fit method* which minimizes the error between the measured pressure (or flow) and modelled output by adjusting the three unknown parameters (in some studies R is set as the MBP over mean flow and is held constant during the fitting procedure) [32].

The input impedance for WK3 is:

$$Z_{\text{in}} = \frac{R + Z_c + j\omega R Z_c C}{1 + j\omega RC}. \tag{2.9}$$

On the other hand, the characteristic impedance is defined as the ratio of pressure to flow when there is no reflected wave. Hence, some papers estimate the characteristic impedance as the average of 6 to 8 instantaneous PP amplitudes to flow during the earliest ejection phase, when there are no reflected waves [33]. That being said, the characteristic impedance is most commonly estimated with high-frequency components of input impedance (e.g., averaging the input impedance module between 3 and 10Hz [34]). Theoretically, wave reflection causes input impedance to oscillate around the characteristic value [35, 36]. If Z_c and R are estimated by the mentioned methods, C is the only unknown parameter in (2.9) and is usually determined at the fundamental frequency (heart rate). The method is called the *low-frequency impedance method* [32, 36].
The governing equation for WK3 is

$$P(t) + RC\frac{d}{dt}P(t) = (R + Z_c)F(t) + Z_c RC\frac{d}{dt}F(t). \tag{2.10}$$

Integrating over (2.10), C can be found as

$$C = \frac{\int_{t_1}^{t_2} P(t)dt - (R + Z_c)\int_{t_1}^{t_2} F(t)dt}{R(P(t_1) - P(t_2)) - RZ_c(F(t_1) - F(t_2))}. \tag{2.11}$$

The *integral method* was proposed by [33] and applied during the ejection period to account for the interaction of Z_c and C, because in the diastolic phase $F(t) = 0$.

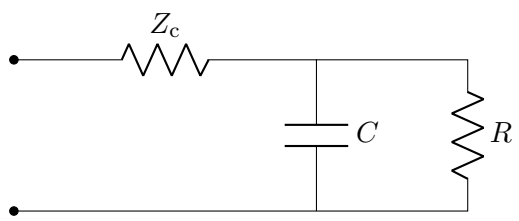

FIGURE 2.5: Schematic diagram of a Three-element Windkessel Model of the circulatory system

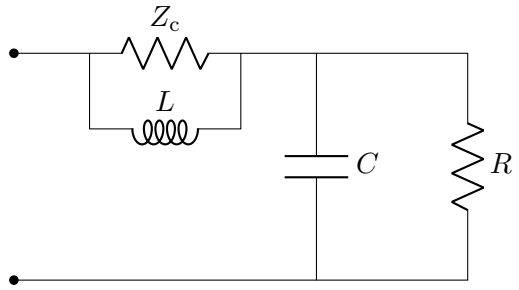

FIGURE 2.6: Schematic diagram of a Four-element Windkessel Model of the circulatory system

- *Four-element Windkessel Models (WK4s):* Although WK3 results show a good fit to pressure and flow data, it has been reported in the literature that the characteristic impedance is underestimated and the total arterial compliance is overestimated by this model [32, 37]. In order to overcome this issue, a forth element was added to the model, as shown in Fig. 2.6. The inductor in the new model represents the total arterial inertance. It helps in direct current (DC) interpretation of input impedance, $Z_{\mathrm{dc}} = R$ (Z_{c} was only added to improve the model performance at high frequencies). For this method, the measured pressure (or flow) is used as the input and parameters are fit to minimize the output flow (or pressure) error. WK4 has provided more accurate estimates of compliance than previous methods [12, 37].

- *Note on Lumped Models:* Note that a lumped element electrical model, such as a Windkessel model model, is valid when the circuit length is much smaller than the circuit's operating wavelength. Therefore, Windkessel model models assume an infinite velocity for blood flow to increase the operating wavelength and maintain the validity of the model. In addition, when we represent compliance with a fixed capacitor, then according to (2.1) we imply linearity between volume and pressure. However, the assumption of a linear pressure-volume relationship does not exactly hold in practice, and methods have also been developed for a pressure-dependent calculation of compliance. An exponential relationship of $\mathcal{V} = ae^{bP} + c$ is a common choice for this purpose, which can be applied to WK models [38].

2.2.2 Transmission Line Models

One of the main assumptions in the WK models is an infinite PWV, which does not allow for the study of wave propagation and wave reflection. TL models, on the other hand, consist of tubes, representing wave propagation in large conduit arteries, and loads, representing wave reflection sites of distal arterial beds. Figure 2.7 shows a single TL model, where R, L, G and C are the distributed resistance, inductance, conductance and capacitance of the line, respectively, all defined per unit length. In most cases, R

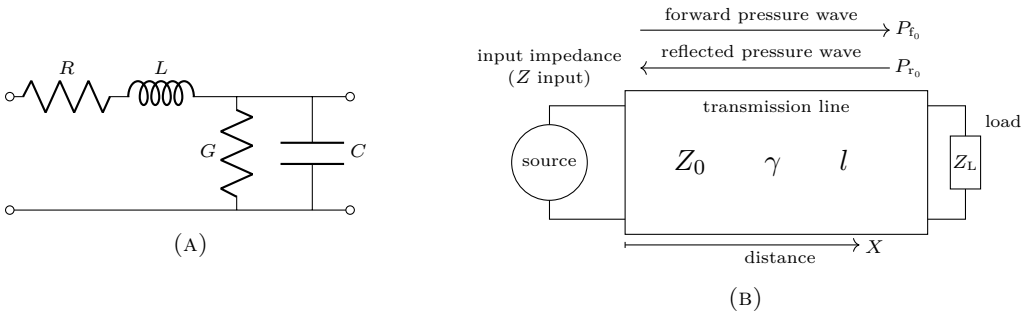

FIGURE 2.7: Transmission Line models. (A) Electrical equivalent (per unit length) of an arterial segment. (B) Transmission segment where Z_{L}, Z_0, l and γ represent load impedance, characteristic impedance, length and propagation constant, respectively; and P_{f_0} and P_{r_0} are the forward and backward travelling pressure waves at the source, respectively.

and G are set to zero, simplifying calculations and assuming a lossless TL for the arterial tree [34, 39]. Nevertheless, knowing the structural properties of the arterial wall, one can calculate these parameters.

$$R = \frac{8\mu}{\pi r^4}, \quad L = \frac{9\rho}{4\pi r^2}, \quad C = \frac{3\pi r^3}{2Eh}, \tag{2.12}$$

in which μ is the blood velocity, r is the internal radius of the arterial segment, ρ is the blood density, E is Young's modulus of the arterial wall and h is wall thickness. A detailed model of the human arterial tree with anatomical data for 128 discrete tubes was presented by [40], which is used as a mathematical reference for validating model performance. The loads, Z_L, are usually a WK3 but other types of loads can also be found in the literature [39]. Using the wave equations [41] to represent voltage and current in an electrical TL, characteristic impedance (Z_0), propagation constant (γ), voltage (P) and current (Q) can be calculated as:

$$Z_0 = \sqrt{(R + j\omega L) \,/\, (G + j\omega C)}, \tag{2.13}$$

$$\gamma = \sqrt{(R + j\omega L) \cdot (G + j\omega C)}, \tag{2.14}$$

$$P(x) = P_{\mathrm{f}_0} e^{-\gamma x} + P_{\mathrm{r}_0} e^{\gamma x}, \tag{2.15}$$

$$Q(x) = \frac{1}{Z_0} \left(P_{\mathrm{f}_0} e^{-\gamma x} - P_{\mathrm{r}_0} e^{\gamma x} \right). \tag{2.16}$$

In which P_{f_0} and P_{r_0} are forward and reflected pressure waves, respectively (Fig. 2.7). The input impedance, Z_{in}, unlike the characteristic impedance, accounts for the reflected waves. Z_{in} is measured at the source and is expressed as:

$$Z_{\mathrm{in}} = Z_0 \frac{Z_{\mathrm{L}} + Z_0 \tanh(\gamma l_0)}{Z_0 + Z_{\mathrm{L}} \tanh(\gamma l_0)}. \tag{2.17}$$

The reflected wave caused by the impedance mismatch, $Z_{\mathrm{L}} \neq Z_0$, in the model, can be characterized using a reflection coefficient. The coefficient is defined as the amplitude of the reflected pressure wave normalized to that of the incident wave. Thus, at the source end, the reflection coefficient is calculated as:

$$\Gamma_{\mathrm{in}} = \frac{Z_{\mathrm{in}} - Z_0}{Z_{\mathrm{in}} + Z_0}. \tag{2.18}$$

Using the reflection coefficient, the forward voltage wave can be linked to the total voltage at the source, $P(x = 0)$, as

$$P_{\mathrm{f}_0} = \frac{P(0)}{1 + \Gamma_{\mathrm{in}}}, \tag{2.19}$$

and the reflected wave is

$$P_{\mathrm{r}_0} = P_{\mathrm{f}_0} \Gamma_{\mathrm{in}}. \tag{2.20}$$

The parameters of the TL model are found by fitting the measured and estimated pressure/flow values, given flow/pressure as the input. However, all the parameters should be within their physiological boundaries (e.g., the characteristic impedance must be lower than the total peripheral resistance). Using common local search methods like steepest descend or Levenberg-Marquardt without an initial guess near the global optimum rarely works; therefore, multiple initial guesses are usually applied [39].

Transmission Line models account for the wave reflection phenomenon from the distal arteries; however, (2.15) also has the assumption that the source impedance matches the characteristic one (i.e., there are no reflected waves from the source). On the other hand, setting $R = 0$ (good approximation for the proximal arteries according to (2.12)) and $G = 0$, implies a lossless TL i.e., γ is purely imaginary and represents the propagating time delay throughout the tube [39].

2.2.3 Applications

The simplicity and accuracy of using electrical models to describe the cardiovascular system have made them the standard approach for non-invasive analysis. Here we mention some recent applications of these models:

Oscillometric blood pressure meters are non-invasive, commercially available devices that calculate pressure with mathematical algorithms applied to pressure sensor measurements. Although these devices return results similar to those of conventional methods for patients with normal blood pressure, for hyper- and hypo-tensive patients, there is a big discrepancy. Use of a WK2 model for calibration has been shown to greatly improve for the accuracy of the results [42, 43].

Pulse Wave Velocity and pulse transit time are important indicators of arterial compliance and a useful cardiovascular clinical markers and can be studied using TL models

[44, 45]. Ageing is associated with an increase in central PWV; however, there is debate over whether impedance matching of central and peripheral arteries occurs and whether reflection sites change with age. Clarification of this issue involves the study of wave propagation using TL models [46, 47].

The pulmonary system which carries blood from the right ventricle to the lungs and back, has 8 to 10 times fewer peripheral vessels than the systemic arterial system. Thus, its high compliance is distributed more evenly over the system. Studies of pressure and flow waves using WK show that the loss of arterial pulmonary compliance in hypertensive patients heightens the risk of myocardial infarction and stroke [48, 49].

2.2.4 Cerebral Arterial Compliance

Here, we review non-invasive approaches to estimating cerebral arterial compliance or determining similar cerebrovascular health indices defined by the type of device used for the estimation.

- *Transcranial Doppler Ultrasound:* TCD ultrasonography is a non-invasive portable technique with high temporal resolution, which estimates blood flow velocity from accessible cerebral arteries, mainly the middle cerebral artery (MCA) [8]. The basic principle is that when ultrasonic waves of known frequency are reflected back from moving red blood cells, their new frequency, called the *Doppler shift frequency*, contains information about the blood flow velocity. The equation relating the parameters in the Doppler method is:

$$\text{Reflector speed} = \frac{(\text{Doppler shift}) \times (\text{propagation speed})}{2 \times (\text{incident frequency}) \times cos(\theta)}. \tag{2.21}$$

  Where θ is the angle of the emitted wave in respect to the direction of the blood vessel [9].

  TCD indices such as AI_{TCD} and PI_{TCD} are commonly used to assess cerebrovascular health [50–53]. The AI quantifies the augmentation of the reflected wave on the incident wave and is defined as

$$\text{AI}_{\text{TCD}} = \frac{V_{\text{refl}} - V_{\text{dia}}}{V_{\text{sys}} - V_{\text{dia}}}. \tag{2.22}$$

  Where V_{refl}, V_{sys} and V_{dia} are the blood flow velocities measured at peak reflection, peak systole and peak diastole, respectively. PI_{TCD}, however, measures the pulsatility of the blood flow velocity as [54]

$$\text{PI}_{\text{TCD}} = \frac{V_{\text{max}} - V_{\text{min}}}{\overline{V}}. \tag{2.23}$$

Where $V_{\max}$, $V_{\min}$ and $\overline{V}$ are the maximum, minimum and mean blood flow velocities, respectively. Conventionally, PI is assumed to describe the CVR distal to the point of measurement [55–57]. However, a more comprehensive study in 2012 showed that in cases of ICP plateau waves, i.e. an abrupt elevation in ICP, PI increases where CVR drops as an auto-regulatory vasodilation mechanism kicks in [58]. This happens because the cerebral auto-regulation system tries to keep the cerebral blood flow (CBF) constant, which is defined in (2.3) as the ratio of CPP (see (2.2)) to CVR. Therefore, when ICP elevates, CPP drops, and based on (2.3), in order to keep the blood flow constant, CVR has to decrease, which will happen with vasodilation. While PI and CVR change in opposite directions with elevated ICP, they both tend to increase in the case of hypercapnia [58].

The parameters $\mathrm{AI_{TCD}}$ and $\mathrm{PI_{TCD}}$ have been shown to have significant correlations with health indicators (see Tables 2.1 and 2.2 for a list of literature reporting Pearson's correlation coefficients for $\mathrm{PI_{TCD}}$ and $\mathrm{AI_{TCD}}$) such as age [50, 53, 59–61], arterial stiffness (or PWV) [51, 52, 59, 62, 63], cerebral white matter diseases and abnormalities [59, 64, 65], cognitive performance and dementia [57, 60, 61, 66, 67], SVD [65, 67] and CRF [68]. Based on the values reported in the literature, although $\mathrm{AI_{TCD}}$ has a stronger correlation with age than $\mathrm{PI_{TCD}}$ and a similar level of correlation with stiffness (as seen Tables 2.1 and 2.2), the pulsatility index is more frequently reported due to its easy calculation. Nonetheless, there are cases reported with lower correlations for $\mathrm{AI_{TCD}}$ [63] and higher correlations for $\mathrm{PI_{TCD}}$ [51].

A method of directly estimating cerebral arterial compliance has been proposed in the literature [72, 73]. The method transforms measured blood velocity into blood volume and uses arterial blood pressure (P) to apply (2.1) . The process is explained here. Assuming a sampling interval of Δt for the device, over each cardiac cycle, cerebral arterial blood volume ($\mathcal{V}$) can be estimated by the difference in arterial inflow and venous outflow:

$$\mathcal{V}(n) \approx \sum_{i \in \text{cardiac cycle}} \left[V(i) \cdot S - V_{\mathrm{v}}(i) \cdot S_{\mathrm{v}}\right] \Delta t. \tag{2.24}$$

Where V is cerebral arterial blood flow velocity with an arterial cross-sectional area of S, and V_{v} is the cerebral venous blood flow velocity with a venous cross-sectional area of S_{v}. Note that we do not use any subscripts for the arterial blood because we commonly use the term *vessel* to refer to the arteries and the measurements from different devices are often obtained from the arteries. It is also assumed that the venous outflow has low pulsatility over the cardiac cycle and can be approximated

Correlating factor reference	Correlation	Age range (population size) /mean age in years
Age [52]	0.25	19–81 (334)/ 50.93
HR [52]	-0.22	"
cf-PWV [52]	0.12	"
ba-PWV [52]	0.23	"
Age [62]	0.32	NA (245)/ 57.7
ba-PWV [62]	0.42	"
Age [51]	0.33	22–86 (165)/ 56.70
cf-PWV [51]	0.45	"
Age [61]	0.27	50–70 (160)/ 59.28
Age [69]	0.36	47–90 (148)/ 66.3
Age [70]	0.05	9–12 (59)/ 10.14
Age [60]	0.32	22–80 (83)/ 49.15
cf-PWV [60]	0.46	"
Pressure AI [60]	0.26	"
CRF [68]	0.41	NA (27)/ 67.0

NA: Data not reported
": as above

TABLE 2.1: Reported $\mathrm{PI}_{\mathrm{TCD}}$ correlations with arterial health factors

Correlating factor reference	Correlation	Age range (population size) /mean age in years
Age [71][1]	0.88	NA (25)/ 40.85
Age [59]	0.54	20–84 (286)/ 54
cf-PWV [59]	0.35	"
Age [53]	0.65	20–72 (56)/ 48.2
Pressure AI [53]	0.91	"

NA: Data not reported
": as above
[1] A different definition of AI is used

TABLE 2.2: Reported $\mathrm{AI}_{\mathrm{TCD}}$ correlations with arterial health factors

as the mean arterial inflow ($\overline{V}$); i.e.,

$$V_{\mathrm{v}}(n) \cdot S_{\mathrm{v}} \approx \overline{V} \cdot S. \tag{2.25}$$

Using (2.25) and reported values of S for MCA, the $\mathcal{V}$ is calculated from (2.24). Then, the TCD-based cerebral arterial compliance, C_{TCD}, is estimated as

$$C_{\mathrm{TCD}} = \frac{\mathcal{V}_{\mathrm{sys}} - \mathcal{V}_{\mathrm{dia}}}{P_{\mathrm{sys}} - P_{\mathrm{dia}}}. \tag{2.26}$$

Where superscripts *sys* and *dia* indicate the peak systolic and diastolic measurements, respectively. The mathematical model that estimates the blood volume for TCD measurements (2.24), assumes that the cerebrovascular diameter does not change, which is inconsistent with the definition of compliance for these vessels.

Measurements by TCD is known to be highly operator-dependent and requires considerable skill and experience. Moreover, the temporal bone thickness prevents TCD measurements of MCA in approximately 20% of patients [7–9].

- *Magnetic Resonance Imaging:* The MRI technique captures dynamic motions and is a non-invasive method of imaging blood and CSF flows in the cranium. The most commonly reported MRI index is the $\mathrm{PI_{MRI}}$, which is calculated from blood flow waveforms. Cerebral blood flow is usually measured via MRI phase contrast (PC) sequences and provides changes in blood flow over a single cardiac cycle. $\mathrm{PI_{MRI}}$ is defined as [74]:

$$\mathrm{PI_{MRI}} = \frac{Q_{\mathrm{sys}} - Q_{\mathrm{dia}}}{\overline{Q}}, \tag{2.27}$$

where Q is the cerebral arterial blood flow measured by MRI. $\mathrm{PI_{MRI}}$ is known to correlate with age [75] and cerebral SVD [74, 76].

A new approach has been recently proposed that uses arterial spin labelling (ASL), which is a non-ionizing MRI technique for measuring blood flow/volume based on tagged (labelled) and control (unlabelled) images. In this method, arterial blood water is magnetically tagged with a radio frequency pulse by saturating or inverting the photons before it enters the area of interest. Subtracting tagged images from controls images removes statistical signals, and the remaining signal contains information about the cerebral blood volume [77]. After extracting the arterial blood volume, [8] used the following equation to calculate compliance normalised to arterial blood volume in diastole. We denote this index as $\mathrm{C_{MRI\text{-}ASL}}$; however, it does not have the same units as compliance.

$$\mathrm{C_{MRI\text{-}ASL}} = \frac{\mathcal{V}_{\mathrm{sys}} - \mathcal{V}_{\mathrm{dia}}}{\mathcal{V}_{\mathrm{dia}}(P_{\mathrm{sys}} - P_{\mathrm{dia}})} \times 100. \tag{2.28}$$

Since the labelled inflow blood is only 0.5% to 1.5% of the total blood reaching the tissue, ASL has a low signal-to-noise ratio (SNR). Also, ASL follows a subtraction technique, which means it is very sensitive to subject movements. On the other hand, the inherently low temporal resolution of ASL (repetition time of 1.4s in [8]; i.e., tag-control image pairs are acquired every 2.8s) combined with the low SNR results in low contrast-to-noise ratio images [77].

Arterial compliance can also be estimated using MRI PC images [78]. Blood flow velocity and vascular cross-sectional area are calculated by manually placing a region of interest on PC sequences. Over a single cardiac cycle, the interception points of the horizontal mean velocity line and the flow velocity waveform mark the beginning and end of the systole (see Fig. 2.8). Then, the mean systolic velocity

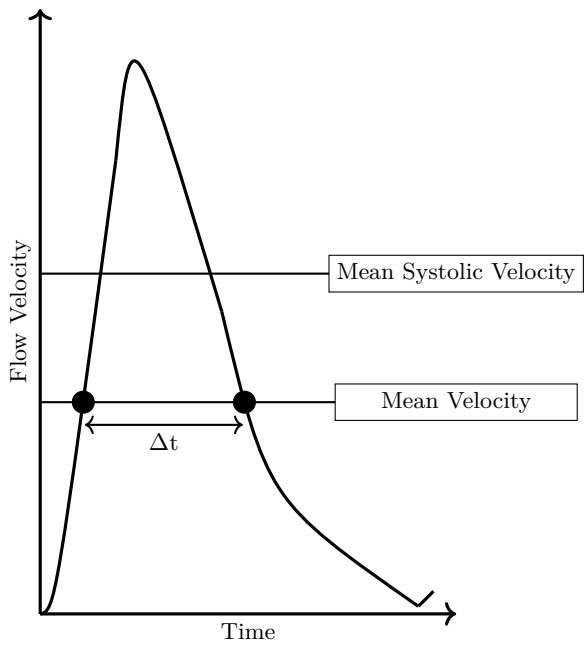

FIGURE 2.8: MRI PC flow velocity waveform (simulated) with mean velocity and mean systolic velocities

which is the mean of the flow velocity waveform during the systole, is multiplied by the duration of the systole, Δt, to give an estimation of the arterial pulse volume. The arterial pulse volume is then divided by PP to calculate compliance using (2.1). A similar approach was taken in [79], where time resolved 3D MRI flow pulsations were compared with 2D PC sequences.

- *Diffuse Correlation Spectroscopy (DCS):* A diffuse correlation spectroscope is an inexpensive, portable device that provides a measure of cerebral blood flow by illuminating the brain surface with NiR light. Diffuse Correlation Spectroscopy (DCS) uses long coherence length continuous wave NiR lasers to provide a constant phase both spatially and temporally. The blood flow information is carried in the electric field of the diffused light, $E(\vec{r}, t)$ (where r denotes position and t is time), and can be extracted with an autocorrelation function as $G_{\mathrm{E}}(\vec{r}, \tau) = \langle E(\vec{r}, t)E^*(\vec{r}, t+\tau)\rangle$ where $\langle\cdot\rangle$ denotes the ensemble average. However, in an experiment, G_{E} is derived from the normalized intensity autocorrelation, $G_{\mathrm{I}}(\vec{r}, \tau) = \langle I(\vec{r}, t)I(\vec{r}, t+\tau)\rangle / \langle I(\vec{r}, 0)\rangle^2$ (I is the measured intensity), using the Siegert relation as

$$G_{\mathrm{I}}(\vec{r}, t) = 1 + \beta \frac{|G_{\mathrm{E}}(\vec{r}, t)|^2}{\langle I(\vec{r}, t)\rangle^2}, \tag{2.29}$$

where β is a numerical factor depending on the detector geometry. G_{E} satisfies a diffusion equation modelled by Brownian motion in a semi-infinite, homogeneous medium. G_{E} is then analytically solved to provide a blood flow index [80]. Based

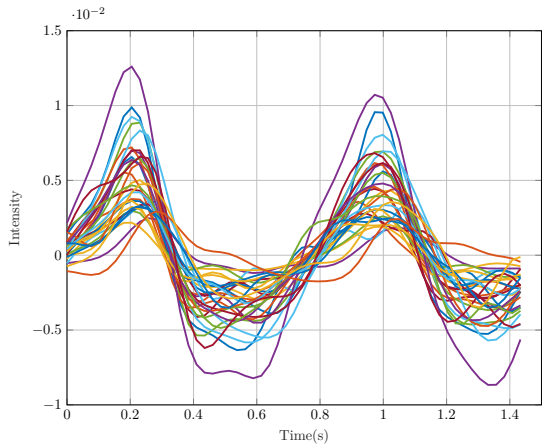

FIGURE 2.9: Averaged NiRS signals for selected channels of a single subject.

on the semi-infinite, homogeneous assumption used in solving the diffusion equation, the DCS index reflects not only blood flow from the skeletal muscle but also that from skin and fat. Calculation of the blood flow index or relative blood flow with DCS requires knowledge of tissue properties like absorption coefficient, reduced scattering coefficient and Brownian diffusion coefficient, and as DCS requires a continuous-wave light source, it is incapable of measuring those parameters. Although constant values from other studies are usually applied, hybrid use of DCS with NiRS has also been proposed to overcome this issue [81, 82]. DCS is known to be more sensitive to blood flow in arterioles than the blood flow in arteries. The reason is that the infrared light is highly absorbed by the arteries so the blood flow index calculated from the autocorrelation function becomes less precise [83].

An interesting approach to estimating cerebral arteriole compliance was taken in [83]. Assuming a WK2 for the arteriole system, they calculated the resistance and compliance by comparing the amplitude and phase of the input impedance using (2.8); i.e., $\measuredangle Z_{\text{in}} = \arctan(-\omega\tau)$, to those of measured data based on pressure and flow.

- *Near-infrared Spectroscopy:*

NiRS is an emerging technique in the field of brain study. Using the NiR portion of the electromagnetic spectrum (690nm to 900nm), NiRS relies on scattering and reflection of NiR light that reaches several centimetres into the brain. The emitted light is scattered and a very small portion (approximately one out of 10^9 photons) finds its way to light detectors placed 2–5cm away from the source [84]. Over this spectrum oxygenated and de-oxygenated haemoglobins are the main absorbers of light and some NiR light is able to pass through several centimetres of tissue before being reflected [85]. Using at least two wavelengths one can separate these elements as indicators of brain activation [84]. NiRS has several advantages compared to other methods of brain study. Its low cost,

Reference/ publication year	Correlation with Age	Correlation with CRF	Sample size	Age range/ mean (years)
[10]/2014	-0.39	0.42	53	55–87/69.53
[86]/2017	-0.43	0.32	48	18–75/47.8
[90]/2017	-0.46	NA	48	18–75/47.8 same as [86]
[91]/2019	-0.60	NA	93	18–87/58.8 combination of [10] & [86]
[92]/2019	0.61	NA	30	28–39 /33 (weeks)
[93]/2019	-0.41	NA	48	18–78/NA same as [86]

NA: Not reported

TABLE 2.3: Reported PReFx correlations with age and CRF. Note that despite using the same dataset, the differences in correlation coefficients reported in [86], [90] and [93] are not clear. In [90], it is stated that the highest and lowest calculated PReFx values are 0.237 and 0.021, whereas the scatter plot of PReFx against age in [86] shows PReFx values as high as ≈0.28.

portability and high temporal resolution make it a worthy alternative to the well-known functional magnetic resonance imaging (fMRI) technique. NiRS also offers higher spatial resolution than electroencephalography (EEG), thereby allowing regional studies. NiRS has gained popularity in the fields of cerebrovascular disease, cerebral arterial pulsation, functional connectivity, cerebrovascular reactivity, brain computer interfacing and event-related fast optical signals [86–89].

To the best of our knowledge, only one research group has addressed the issue of estimating cerebral compliance with NiRS technology, [94]. Changes in blood volume over each cardiac cycle leave a periodic shape in the measured NiRS intensity signal, referred to as the *arterial pulsation (AP)* signal. A sample of averaged NiRS signal from different channels of a single subject showing the arterial pulsation (AP) signal is presented in Fig. 2.9. The NiRS signal has always been analysed to extract haemodynamic responses; i.e., changes in blood flow in relation to neural activation, with the AP signal treated as an unwanted component that needs to be filtered out. In [10], the authors proposed using the AP signal to estimate brain health factors. To this end, it has been assumed that during diastole, the pressure and, therefore, volume decays exponentially and, in cases of high arterial compliance, reflected waves are observed earlier, leaving deformation in the decaying portion of the signal. Therefore, the method uses this deformation in the AP signal that occurs between the systolic and diastolic peaks as an index of vascular compliance called *pulse relaxation function (PReFx)*. To calculate the PReFx, first, an AP signal is calculated by dividing a channel by its mean and then bandpass filtering the signal (0.5-5.0Hz). The signal then rotated around the x-axis to represent light absorption (see Fig. 2.10) where two diastolic peaks and a systolic peak are visible. In Fig. 2.10 the time is assumed to start at the electrocardiography (ECG) R peak occurrence. Then, a rectangle is imagined with the systolic peak and second

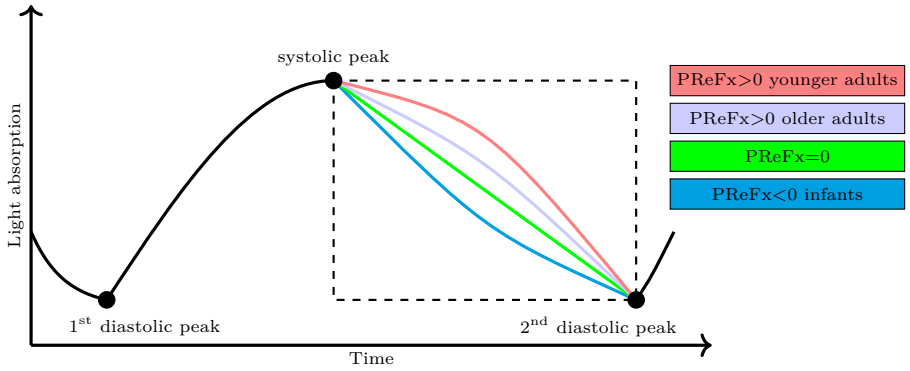

FIGURE 2.10: PReFx calculation and range for different age groups

diastolic peak at its diagonals with an area of B. Next, the area enclosed by the NiRS signal and the left and lower sides of the rectangle is calculated as A. Finally,

$$\text{PReFx} = \frac{A}{B} - 0.5. \tag{2.30}$$

PReFx has been reported to correlate with age and CRF. See Table 2.3 for a list of reported correlation coefficients. PReFx was first labelled as *arterial compliance* but later was named *pulse relaxation function* due to the belief that it reflects "a combination of arterial elasticity and peripheral resistance" [90]-page 200. Although it is generally shown that PReFx correlates negatively with age [10, 86, 90], a strong positive correlation was reported in [92] in a study on preterm infants, where higher PReFx values are thought to represent higher cerebrovascular development. This, is consistent with studies on central arteries stating that arterial stiffness decreases sharply with age in the first decade of life and increases thereafter [95]. As mentioned in the literature [90, 92] and illustrated in Fig. 2.10, younger adults have the highest PReFx values, whereas older adults have positive and low PReFx values and infants show negative PReFx values as their systolic-to-diastolic curve lays under the straight line of PReFx=0.

2.3 Health Implications of Vascular Stiffening

Central and cerebral arteries become stiffer with age, causing structural and functional changes in the arterial wall that lead to SVD [6, 96]. These changes contribute to increased PP and hypertension among other effects [97]. In the brain, cerebral SVD reduces CBF and vasodilator reserve, reduces PO_2 and O_2 transport, causes lacunes (3-15mm CSF-filled cavities in the white matter), microinfarcts (microscopic lesions of cellular death or tissue necrosis), microbleeds, white matter abnormalities and brain atrophy. These can lead to cognitive impairment such as dementia and Alzheimer's disease, and non-cognitive impairment such as loss of balance and metabolic dysfunction [28].

Although these disadvantageous changes seem to be an unavoidable outcome of ageing, it has been shown that physical activity can slow age-related progression of arterial stiffening [98, 99]. In a longitudinal study of 5196 participants it was concluded that moderate-to-vigorous activities are associated with slower progression of aortic stiffness (measured via aortic-femoral PWV) over time and that sports are particularly effective in slowing arterial ageing [99]. Similar results are reported for the brain, showing that physical activity improves cerebrovascular and cognitive functioning [100]. Nonetheless, physical activity does not show a long-lasting effect on arterial compliance. Studying the effects of a single 30-minute bout of cycling exercise, it was found that the overall arterial compliance was elevated at 30 minutes post-exercise and then declined to baseline 60 minutes after the exercise [101]. This emphasizes the importance of developing easy-to-use devices for routine measurement of cerebral arterial health that help the ageing population track and maintain their brain health and facilitate early intervention for related diseases.

Chapter 3

A Mathematical Model of Wave Reflection

3.1 Introduction

Vascular ageing is a prominent factor in major cardiovascular events including stroke, heart failure and coronary artery disease [102]. Vascular health is studied through pulsatile arterial haemodynamics and several key indicators of vascular ageing have been identified in pulsatile pressure readings such as pulse wave velocity (PWV), reflection time (T_{refl}), and augmentation index (AI) [102, 103].

In particular, reflected waves are frequently studied to infer cardiovascular properties [103]. Reflected waves occur when forward-travelling pressure waves hit an effective reflection site (which, in practice, is a superimposition of several sites) and are reflected back towards their source (in this case the heart). In elastic arteries appropriately timed reflected waves help maintain pressure during diastole, however, they can have an ill-effect as age progresses and PWV increases. With increased PWV, which more than doubles in the aorta between the ages of 17 and 70 [104], reflected waves advance into the systole and add to the systolic pressure [105]. This increases the peak-systolic, end-diastolic and mean arterial pressures [106] and contributes to stress on the vessels [103].

The concept of reflection time, pulse transit time or pulse return time has been defined as the timing of the *nflection point* on the central pressure waveform [46]. This is a visible curvature in the waveform caused by a forward-travelling pressure waveform from the left ventricle combining with a reflected wave. Similarly, on more distal pressure waveforms, the *pulse transit time* is defined as the time difference between the first (systolic) and second (reflected) peaks [107]. Both definitions aim to capture the same phenomenon; the latter measures the peak-to-peak difference of the forward and reflected waves, whereas the former measures the foot-to-foot time differences. Here, we will call

this time interval as T_{refl}, which is commonly formulated as:

$$T_{\text{refl}} = \frac{2d_0}{\text{PWV}} \tag{3.1}$$

where d_0 is the distance from the measurement site to the reflection site, multiplied by two to account for a round trip. The equation simply calculates the travel time by dividing distance by travel speed. This equation is commonly used to assess vascular compliance or to estimate d_0 [2, 19, 46, 106, 108–114] and here will be referred to as the existing T_{refl} model. It should be noted that (3.1) holds only when a resistive load is assumed; i.e., a real load (in a mathematical sense) impedance [46, 114, 115]. However, a purely resistive load can not sufficiently model distal arteries [115]. In elderly populations (>65 years), T_{refl} reaches a plateau state whereas, PWV still increases and the first conclusion from (3.1) is increased d_0. This is referred to as the apparent distal shift of the reflection site after age of 65 years [2, 106] which contradicts with the accepted opinion [116]. Debate about changes in d_0 has been the topic of several publications [2, 46, 106, 115]. In this chapter, we will examine the controversy surrounding moving reflection sites and other observations of T_{refl} and AI values by understanding these indices from a mathematical viewpoint using a model of the vascular tree.

As mentioned in Chapter 2, a number of models have already been developed to study the vascular system. Two-element Windkessel Models (WK2s) in the form of an *RC* circuit were the first generation [103]. Later, a third element was added in series to model the characteristic impedance of the arterial tube in a three-element Windkessel model (WK3) [12, 36, 117]. The WKs, although popular and efficient for parameter estimation due to their simplicity, are unable to reflect the finite PWV and thus the wave propagation phenomenon and the presence of reflected waves in the arterial system. Thereby, TL equations and models have been adopted to understand changes in flow and pressure at the pace that they advance in the arteries [39, 117].

In Section 3.2, we assume a WK3 at the load and use the TL theory to formulate T_{refl} and AI in terms of the model parameters. Then, in Section 3.3 we use values reported in the literature for each parameter and compare measured T_{refl} and AI values to the model outputs. After validating our models of T_{refl} and AI, we use them to gain insights into commonly observed measurements.

3.2 Method

In this section we will first briefly review the TL theory then define T_{refl} and AI in terms of the model parameters. Finally, we will show how the model performs in estimating these parameters using various datasets reported in the literature.

3.2.1 Model Derivation

The approach is based on a uniform TL model of the vascular system used in the literature [39, 117] and introduced in Chapter 2 (see Fig. 3.1). The heart is located at $x = -d$ with blood pressure and flow of P_{H} and Q_{H}, respectively. The characteristic impedance of the TL is Z_0 and the reflection site has blood pressure and flow of P_{L} and Q_{L}, respectively, terminated by a WK3 with its third element, Z_0, matching the characteristic impedance of the line. The resistance and compliance are R and C, respectively, which resemble the properties of the vascular system beyond the reflection site. It should be mentioned that a tapered model [118] can be used instead of a uniform model; however, given a fixed measurement distance, the two models can be considered equivalent given appropriate optimization of the parameters [119]. Note that the TL model accounts only for the pulsatile components of the pressure and flow.

Pressure as a function of time and distance can be decomposed into forward and backward travelling elements, i.e.,

$$P(x) = P_{\mathrm{f}}(x) + P_{\mathrm{b}}(x). \tag{3.2}$$

In which $P_{\mathrm{f}}(x)$ and $P_{\mathrm{b}}(x)$ are the forward (incident) and backward (reflected) travelling waveforms. These waveforms are in the form of

$$P_{\mathrm{f}}(x) = p_{\mathrm{f}} e^{-\gamma x}, \quad P_{\mathrm{b}}(x) = p_{\mathrm{b}} e^{\gamma x}, \tag{3.3}$$

where p_f and p_b generally have complex quantities and are calculated using the boundary conditions. Variables γ and x are the propagation constant and distance from the load, respectively. Note that (3.2) and (3.3) are phasor domain solutions to the TL equations with an assumption of steady-state sinusoidal pressure and flow input waveforms. For a lossless case, the time domain solution will be

$$p(x,t) = |p_{\mathrm{f}}| \cos(\omega t - \beta x + \phi_{\mathrm{f}}) + |p_{\mathrm{b}}| \cos(\omega t + \beta x + \phi_{\mathrm{b}}), \tag{3.4}$$

where $|p_{\mathrm{f}}|\, e^{j\phi_{\mathrm{f}}}$ and $|p_{\mathrm{b}}|\, e^{j\phi_{\mathrm{b}}}$ are the amplitude and phase of p_{f} and p_{b} in (3.3), respectively, and β is called the *phase contrast*, which is equal to the imaginary part of γ. The reflection coefficient is defined as the ratio of the reflected pressure wave to the incident pressure wave, i.e.,

$$\Gamma(x) = \frac{P_{\mathrm{b}}(x)}{P_{\mathrm{f}}(x)} = \frac{p_{\mathrm{b}} e^{j\beta x}}{p_{\mathrm{f}} e^{-j\beta x}} = \frac{p_{\mathrm{b}}}{p_{\mathrm{f}}} e^{j2\beta x}. \tag{3.5}$$

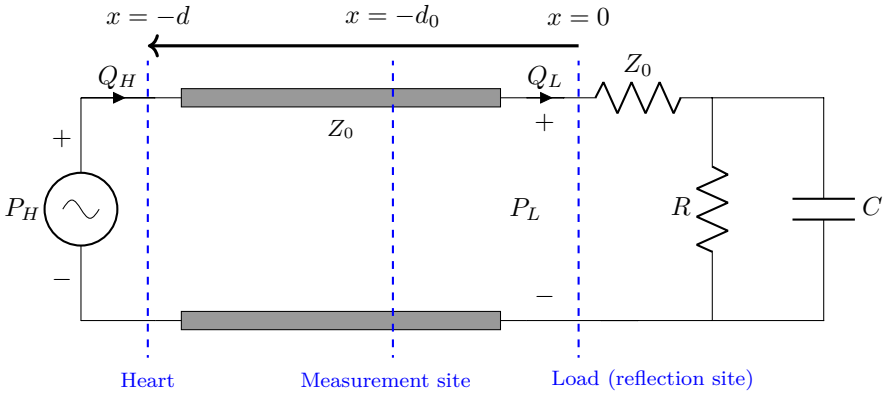

FIGURE 3.1: Transmission Line model of the vascular system

3.2.1.1 Reflection Time

In order to formulate the reflection time using TL theory, let Φ be the phase difference between the forward and reflected waves at $x = -d_0$ along the line, which will be equal to the absolute value of the phase of the reflection coefficient at the same location, $\theta_\Gamma(x = -d_0)$, i.e,

$$\Phi = |\theta_\Gamma(-d_0)| = |\theta_\Gamma(0) - 2\beta d_0| \,. \tag{3.6}$$

To calculate $\theta_\Gamma(0)$, we should first quantify the reflection coefficient at the load, $x = 0$. We have

$$\Gamma(0) = \frac{Z_L - Z_0}{Z_L + Z_0}, \tag{3.7}$$

where $Z_L = P(0)/Q(0)$ (see Fig. 3.1). Also, with a WK3 at the load (see Fig.3.1), we have

$$Z_L = Z_0 + \frac{R}{1 + j\omega RC}, \tag{3.8}$$

inserting into (3.7) gives

$$\Gamma(0) = \frac{R}{R + 2Z_0 + 2j\omega Z_0 RC}, \tag{3.9}$$

with its phase equal to

$$\theta_\Gamma(0) = -\tan^{-1} \frac{2\omega Z_0 RC}{R + 2Z_0}. \tag{3.10}$$

Using the first order Taylor series expansion on (3.10) and inserting it into (3.6), we get

$$\Phi \approx \frac{2\omega Z_0 RC}{R + 2Z_0} + 2\beta d_0. \tag{3.11}$$

The phase constant (β) is related to the PWV (or propagation velocity) as $\beta = \omega/\text{PWV}$. Also, note that we are interested in measuring the time difference between the forward and reflected waves, T_{refl}, which is the phase difference (Φ), divided by the angular

velocity (ω). Inserting these into (3.11) we have

$$T_{\text{refl}} \approx \underbrace{\frac{2Z_0RC}{R+2Z_0}}_{\Delta t_{\text{load}}} + \underbrace{\frac{2d_0}{\text{PWV}}}_{\Delta t_{\text{line}}}, \tag{3.12}$$

which breaks the travel time of the reflected wave into two elements. The delay caused by the line itself is Δt_{line}, which is influenced by the speed on the line and the length of the line. The delay at the load is Δt_{load}, which is forced by the capacitive properties of the load. Thus, the wave reflection is more than a simple "round trip" as there is a delay in between.

It should be noted that the reflection site (Fig. 3.1) in the proposed model is a symbolic reflection location which represents reflections from various reflection and re-reflection sites [120]. Therefore, d_0, the distance between the measurement and reflection sites, does not indicate a specific location in the arterial system with reference to the measurement site and, in fact, it can have a value larger than what one would expect based on the vascular structure. The reason is there are re-reflection sites that are closer to the heart than the measurement point and reflect back the already reflected waves [120]. These waves with much larger d_0 values also add to the measured pressure contributing to the reflected pressure waveform.

3.2.1.2 Augmentation Index

The augmentation index (AI) is defined as:

$$\text{AI} = \frac{P_{\text{refl}} - P_{\text{dia}}}{P_{\text{sys}} - P_{\text{dia}}}, \tag{3.13}$$

in which P_{refl}, P_{dia} and P_{sys} are the peak reflection, end-diastolic and peak systolic blood pressures, respectively [121]. A transcranial Doppler augmentation index was defined similarly in (2.22). This definition is commonly used to report AI for arteries distal to the heart and features two distinctive peaks in the waveform. For proximal arteries where reflected and incident waves often overlap, another definition is used.

$$\text{AI}^* = \frac{P_{\text{refl}} - P_{\text{sys}}}{P_{\text{max}} - P_{\text{dia}}}, \tag{3.14}$$

where $P_{\text{max}} = \max\{P_{\text{refl}}, P_{\text{sys}}\}$ [108, 112, 122–124]. Augmentation Index, Alternative Definition (AI^*) can be expressed in terms of AI as:

$$\text{AI}^* = \begin{cases} 1 - 1/\text{AI} & P_{\text{refl}} > P_{\text{sys}}\,(\text{i.e., } P_{\text{max}} = P_{\text{refl}}) \\ 0 & P_{\text{refl}} = P_{\text{sys}} \\ \text{AI} - 1 & P_{\text{refl}} < P_{\text{sys}}\,(\text{i.e., } P_{\text{max}} = P_{\text{sys}}) \end{cases} \tag{3.15}$$

It is known that the reflected waves make a negligible contribution during the period between end-diastole and peak-systole because of the lossy line properties of the arterial tree. Therefore, in the absence of the reflected wave, we can assume:

$$P_{\text{sys}} \approx \text{MAP} + |p_{\text{f}}| \,. \tag{3.16}$$

In practice, mean arterial pressure (MAP) is closer to the end-diastole than the peak systole, because of the differences in systolic and diastolic durations. For instance the end-diastole, MAP and peak systole are reported in [125] as 77.5, 93.0 and 124.1mmHg, respectively. This shows that the difference between the systolic peak pressure and the MAP is twice as great as that of the end-diastolic peak pressure. Here, for the practicality of the formulation we use the same concept; i.e.,

$$P_{\text{dia}} \approx \text{MAP} - \frac{1}{2}\,|p_{\text{f}}| \,. \tag{3.17}$$

Now, to quantify the reflected peak value, we should be mindful of the phase difference between the forward and backward travelling waves. Based on the approach taken in Section 3.2.1.1, when the reflected wave reaches its maximum value, the incident wave decreases its amplitude by a factor of $\cos\Phi$ or $\cos(\omega T_{\text{refl}})$. This means that:

$$P_{\text{refl}} \approx \text{MAP} + |p_{\text{f}}| \cos(\omega T_{\text{refl}}) + |p_{\text{b}}| \,. \tag{3.18}$$

In which the second term is the amplitude of the forward-travelling wave when the reflected peak occurs and the third term is the maximum value of the backward-travelling wave at the same time. Inserting (3.16), (3.17) and (3.18) into (3.13), our formula of AI becomes:

$$\text{AI} \approx \frac{2}{3}\left(\cos(\omega T_{\text{refl}}) + |\Gamma(0)| + \frac{1}{2}\right), \tag{3.19}$$

The AI^* can be calculated from (3.19) using (3.15). Also, note that in this section we do not assume sinusoidal waveforms except to define T_{refl} in (3.18).

3.3 Model Validation

In this study, we compare values reported in the literature with values derived from our models. It is important to note that we do not "fit" our models to the data. All model parameters are taken from the literature. Among the input variables used to the model the parameters, R and C are load properties which are located far from the heart and compliant vessels regardless of the measurement site. Therefore, location-independent values can be selected for these parameters. However, the characteristic impedance (Z_0) and PWV are both line properties, which can change as the measurement location

becomes more distal from the heart. Here, we will ignore the PWV increase from the aorta to the radial artery (the farthest artery we will examine) as this has been reported to be small [126] and will not affect the model results. Yet, we will try to match Z_0 to its realistic values depending on the artery of interest.

3.3.1 Case I

We used data from a large-scale study [127] of 2026 healthy middle-aged subjects that were divided into four groups with half-decade age ranges with means of 37.5, 43, 48 and 53.5 years. Pressure waveforms were measured from the left common carotid artery using applanation tonometry (flow was measured from the aorta using ultrasound). The mean and standard deviation (std) values for HR, characteristic impedance (we used the frequency-domain method results) and systemic vascular resistance (R) for men and women are reported for each age group [127] in Table 3.1.

Although total arterial compliance values are provided in the study [127], we are interested in load compliance values, which are much smaller than when measurements from the proximal compliant vessels are involved in the calculations. Therefore, we used the mean compliance values of the arteries distal to the heart (referred to as *oscillatory compliance* in [14]), which were measured by invasive methods in [14] (4.852 and 2.670 in units of $10^{-1}\mathrm{kPa}^{-1}\cdot\mathrm{cm}^3$ for men and women, respectively) to downscale the values reported in [127] (see Table 3.1). That is, the compliance values (calculated from the pulse pressure method) reported for each age group were scaled so that the total mean value for each gender would be same as that reported in [14]. We have set $d_0 = 40$ cm for men and $d_0 = 35$ cm for women which covers an approximate distance from the arch of the aorta to the end of the internal carotid artery. The values were approximated based on a distance of 38.6 cm, which was calculated from the data in [40].

The final carotid $\mathrm{T_{refl}}$ model for this case was calculated according to our formula (3.12), with load compliance values derived from [14] and [127], d_0 of 40cm and 35cm for men and women, respectively, and PWV, Z_0 and R as reported in [127] for each gender and age group. The values in Table 3.1 were also used to calculate the model estimates of $\mathrm{T_{refl}}$ in (3.1).

Next, to estimate the augmentation index the values of the reflection coefficient at the load site, i.e., $|\Gamma(0)| = |p_\mathrm{b}| \,/\, |p_\mathrm{f}|$, are needed. These values were calculated in [127] as the amplitude of the reflection coefficient at the heart rate frequency. Using the measured $|\Gamma(0)|$ and estimated $\mathrm{T_{refl}}$ values in (3.19) and then (3.15) gives us the model-estimated AI^* values.

Parameter	Gender	Mean ± std value of the age group				Unit
Age range		$35-40$	$41-45$	$46-50$	$51-56$	years
HR	M	61.1 ± 9.1	61.2 ± 9.2	63.1 ± 10.3	61.8 ± 9.9	bpm
	F	65.3 ± 9.0	65.8 ± 8.8	65.2 ± 8.5	65.4 ± 8.1	
Z_0	M	155	136	135	134	10^{-4}kPa·cm^{-3}·s
	F	155	150	145	145	
R	M	1654	1690	1688	1713	10^{-4}kPa·cm^{-3}·s
	F	1650	1677	1722	1804	
C	M	4.785	5.010	4.875	4.740	10^{-1}kPa^{-1}·cm^3
	F	2.781	2.726	2.642	2.531	

TABLE 3.1: HR, Z_0 and R values as reported in [127] (age groups of case I) for men (M) and women (F). Scaled C values are based on [127] and [14].

3.3.2 Case II

For this case we used the data of 266 healthy participants (age range of 18-78 years and mean ± std of 37.9 ± 18.9 years) reported in [107]. Radial arterial pressure was measured using applanation tonometry and the time interval between the first and the second systolic peaks was calculated as $\mathrm{T_{refl}}$. None of the model inputs are reported in [107] and therefore, for this case, we used values reported in other literature as follows. Values of C were measured with invasive methods in 115 healthy volunteers in [14]. Although a linear relationship between C and age was derived in [14], non-linear changes are noticeable in the scatter-plot and thus we digitized the data to fit an exponential function as:

$$C = 12.39 \times \exp\left(-0.0277 \times \mathrm{Age}\right) + g_{\mathrm{c}}. \tag{3.20}$$

Where g_{c} is a gender correction parameter, set to +0.77 and -0.70 for men and women, respectively, to satisfy $C_{\mathrm{men}}(\mathrm{age} = 40) = 4.85$ and $C_{\mathrm{women}}(\mathrm{age} = 47) = 2.67$, as reported in [14] for the mean age of each group (the same units used in Table 3.1 are used here). To model R in healthy volunteers aged less than 50 years, we used the linear increase reported in [14] in the first line of (3.21). However, for ages more than 50 years, we propose an exponential relationship, the second line of (3.21).

$$R = \begin{cases} 8.1 \times \mathrm{Age} + 926.9 + g_{\mathrm{r}} & \mathrm{Age} \leq 50 \\ 333.4 \times \exp(0.0277 \times \mathrm{Age}) + g_{\mathrm{r}} & \mathrm{Age} > 50 \end{cases}. \tag{3.21}$$

This is based on a comprehensive blood pressure study of 2036 participants stating that the estimation of the vascular resistance using MBP underestimates the actual resistance value at ages above 50-60 years [128]. The exponential factor is set to a similar rate as the observed exponential rate in C; i.e., 0.0277, and the amplitude of 333.4 is used to avoid discontinuity at age = 50. The gender correction factor, g_{r}, is set to -32 and +105 respectively, for men and women to satisfy $R_{\mathrm{men}}(\mathrm{Age} = 40) = 1219$ and $R_{\mathrm{women}}(\mathrm{age} = 47) = 1413$ [14] (same units used in Table 3.1 are used here).

Pulse wave velocity has the form of

$$\mathrm{PWV} = 10 \times \mathrm{Age} + 300 \quad \left(\mathrm{cm} \cdot \mathrm{s}^{-1}\right) \tag{3.22}$$

as reported in [129] and was measured in the ascending aorta and matches the results in [130]. Finally, we estimated the characteristic impedance as $Z_0 = 1.185$ kPa·cm^{-3}·s with a WK3 fit to the synthetic data provided in [131]. Based on the results reported in [127], Z_0 either does not change with age or changes negligibly; thus, we used a constant $Z_0 = 1.185$ for all ages. We also set $d_0 = 20$ cm and $d_0 = 16$ cm, respectively, for men and women corresponding to the length of the radial artery (a mean of 18cm was reported in [132]).

Putting mentioned the values for each parameter into (3.12) and (3.1), we obtain radial $\mathrm{T_{refl}}$ estimates for our model and the existing model, respectively.

3.3.3 Case III

A radial augmentation index was reported in [121] for 632 healthy subjects, where AI was defined as in (3.13). Age-independent heart rate values were reported as 70.6 ± 11.0 and 71.5 ± 9.5 (mean $\pm$ std, beats per minute (bpm)) for men and women, respectively [121]. For this case, all other inputs were selected as described in Section 3.3.2. First, $\mathrm{T_{refl}}$ was calculated as per (3.12) and then, using (3.9), $|\Gamma(0)|$ was calculated. Substituting into (3.19) provides the modelled AI for the radial artery.

3.3.4 Case IV

Changes in aortic $\mathrm{T_{refl}}$ with PWV in 73 outpatients (age range 17-95 years, mean age 51.8 years) were reported in [133]. In this study, pressure waveforms were recorded with non-invasive methods from the carotid artery and were assumed to be similar to the pressure values in the ascending aorta and central arteries. Reported values were not separated by gender and so we used (3.20) and (3.21) to obtain gender-independent estimates of C and R with $g_\mathrm{c} = 0$ and $g_\mathrm{r} = 0$, respectively. We set $d_0 = 40$ cm and $Z_0 = 0.136$ kPa·cm^{-3}·s, estimated for the carotid artery using a WK3 fitted to the synthetic data of [131]. Results are gender-independent carotid reflection times for the new and existing models using (3.12) and (3.1), respectively calculated using the same age range as in [133]; i.e., 17-95 years.

3.4 Results

The formulas derived from the model were validated numerically against the numbers reported in the literature. For cases I-III the results are shown in Fig. 3.2 and Fig. 3.3 and for case IV the results are in Fig. 3.4. Note that case I reports AI^* values, whereas

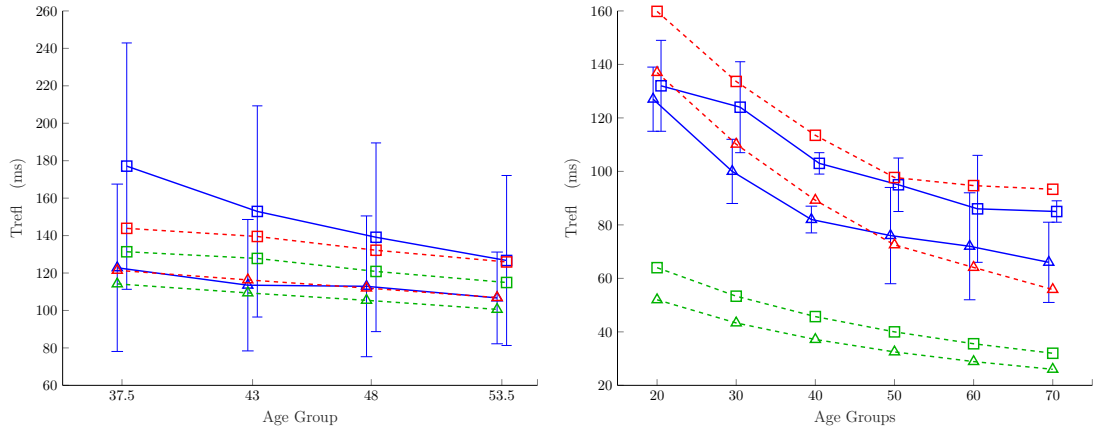

(A) (B)

FIGURE 3.2: T_{refl} in (a) carotid artery, case I and (b) the radial artery, case II for men (squares) and women (triangles). Measured data (blue) is from the literature [107, 127] and estimated values are from the proposed model (red) and existing model (green). Values are means ± std.

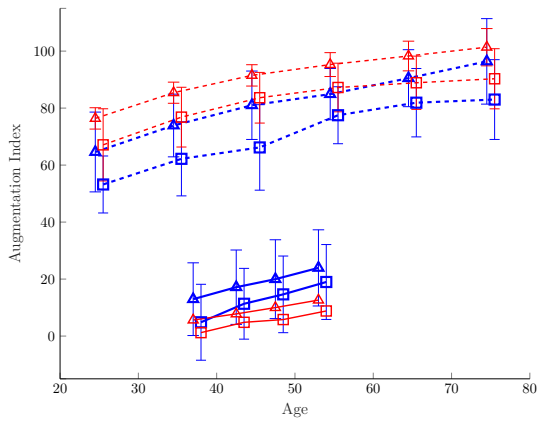

FIGURE 3.3: Measured (blue) and estimated (red) augmentation index for men (squares) and women (triangles) in carotid (solid lines, case I) [127] and radial arteries (dashed lines, case III) [121]. Values are means ± std.

case III reports AI values. The AI* values reported in [127] are in the form of means and standard errors of the mean, which have been converted into mean ± std in the present study. Error bars for estimated AI in case III are only due to heart rate variability and no other variation has been taken into account. The results show high similarity between the modelled and measured T_{refl} and AI values and that the reflected wave estimates are much improved compared to those of the existing model, especially those of the radial artery.

Carotid AI* for young adults is reported to be negative but becomes positive as age progresses [53, 134]. Based on our model $P_{refl}/P_{sys} = \cos \omega T_{refl} + |\Gamma(0)|$ gives estimated P_{refl}/P_{sys} values ranging from 1.02 to 1.14 and from 1.09 to 1.22 for men and women, respectively for case I. With a linear regression of the model outputs, we speculate that at the ages of 34.0 and 24.9 years in men and women, respectively, we will obtain

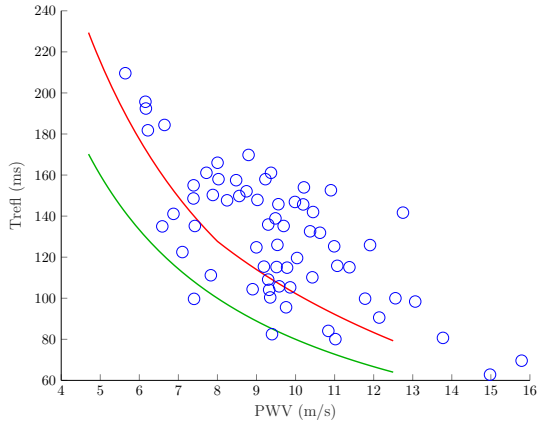

FIGURE 3.4: Estimated carotid T_{refl} against PWV using the proposed model (red) and existing model (green) compared with measured values from [133] (case IV; blue).

$P_{refl} = P_{sys}$ and, thus, AI^*=0 for this case (see Fig. 3.3). Carotid AI^* zero crossing has been reported at the ages of 31.7 years (for 38 male and 18 female participants in [53]) and 23.7 years (for 74 male and 60 female participants in [134]). This is another prediction of the model that is confirmed in the literature.

3.5 Discussion

In this chapter a TL model is used to formulate T_{refl} and AI in terms of both line and load properties. Through several case studies we compared our models for T_{refl} and AI against published measured data and showed that we can closely match the observed data. Thus, we can apply these models to gain insights into several observed phenomena, which are discussed in this section.

Several studies have reported a strong correlation between T_{refl} and age [106, 107, 110]. Based on our model we can see that the load site delay of the reflection time, Δt_{load}, is primarily influenced by the compliance of the load, as the resistance properties, R and Z_0, are found in both the numerator and denominator of the model in (3.12), and so cancel out to some extent. In addition, PWV itself is a function of the line compliance (the compliance of the arteries between the measurement and reflection sites, which is commonly used as an index of vascular compliance [135]) and, combined with the influence of load compliance (the WK3 compliance at the load) makes T_{refl} a strong index of overall vascular compliance with only weak effects from vascular resistance. It is well known that compliance decreases with age; therefore, based on our model the correlation of reflection time with age is due to a strong dependence on changes in compliance and PWV with age.

It is reported in the literature that T_{refl} does not decrease linearly with age in elderly populations and, in fact, almost flattens after the age of 65 years [46, 106, 115]. The flattening effect is reflected in our model (Fig. 3.2) through three main components.

1) Model (3.20) indicates that there is a non-linear relationship between load compliance and age. Based on the data reported in [14], measured load compliance does not decrease as sharply with age in older populations as it does in younger ones. 2) Vascular resistance, R, increases exponentially after the age of 50 years (see (3.21)), which contributes to an increase in Δt_{load} and thus T_{refl}. This ultimately stops Δt_{load} from dropping which weakens the dependency of T_{refl} on age and compliance in older populations. 3) The influence of characteristic impedance makes the effect highly dependent on the site of measurement. Based on our estimates from the data in [131], the value of Z_0 increases almost ten-fold as the measurement site is moved from the carotid to the radial artery. The small Z_0 values in proximal arteries heighten the flattening effect on T_{refl}. As an example, with all three elements in effect, based on the model for case IV, carotid T_{refl} decreases by 37ms between the ages of 10 to 20 years and only 9ms from 80 to 90 years. Thus, based on our model, the flattening of the reflection time curve is due to exponential changes in compliance and vascular resistance with age. Also, the effect is more noticeable in proximal arteries due to the decreased impedance in large vessels.

It has been reported that the effective reflection site moves distally after the age of 65 years [2, 106], although this view is challenged in several studies [46, 115]. Our model is able to explain this phenomenon by shedding light on the delay in the reflected wave at the load site, Δt_{load}. Note that the Δt_{load} portion of T_{refl} is usually ignored in analyses [2, 46, 106, 108, 109, 112, 113, 115], despite the hints given in [118] and [115]. Based on our model Δt_{load} can account for up to 25% (case IV) and 62% (case II) of T_{refl} in the carotid and radial arteries, respectively. Δt_{load} becomes larger relative to Δt_{line} with movement distal from the heart for two main reasons: a decrease in d_0 and an increase in Z_0. Figures 3.2 and 3.4 provide examples of radial and carotid T_{refl} estimates acquired from (3.1) for cases II and IV, respectively. Thus, the results reported in [2, 106] using (3.1) should be treated with care and our model (3.12) can be used for more accurate interpretations of the location of the reflection site. Nonetheless, the model seems to underestimate T_{refl} in case IV (Fig. 3.4) when PWV changes between 8 and 9 $\text{m}\,\text{s}^{-1}$ which correspond to only seven collected data points in case IV. Although the proposed model vastly improves the accuracy of T_{refl} estimation compared to the existing model, a more comprehensive recorded dataset may be required to investigate the data points that do not align with the proposed model.

It is reported in the literature that reflection time does not notably change with HR; only a 10ms drop in radial T_{refl} was reported for HRs of 60-80 bpm for the data in case II [107]. Our model confirms the independence of HR and T_{refl} as HR does not affect the T_{refl} calculated by (3.12).

The AI has been shown to have negative correlations with T_{refl} [136] and HR [137] and a positive correlation with age [2, 53, 121]. Our model also shows these effects and describes AI as a function of T_{refl}, heart rate and reflection coefficient (see (3.19)). Even

in extreme cases, $\max(\mathrm{T_{refl}}) < 0.25$s and $\max(f_{\mathrm{HR}}) < 0.5$Hz ($f_{\mathrm{HR}}$ being HR frequency) and, therefore, $0 < \omega T_{\mathrm{refl}} < \pi/2$, suggesting that the cosine function is monotonically decreasing and AI will always increase with decreases in $\mathrm{T_{refl}}$ or HR, explaining the negative correlation. Thus our model suggests that the positive correlation of AI with age is due to decreases in $\mathrm{T_{refl}}$ with ageing and the negative correlation between AI and HR is due to the presence of the cosine function.

A flattening effect of the AI has repeatedly been reported [2, 111, 123]. It has been observed that $\mathrm{AI/AI^*}$ flattens after the age of 55 years [123] or can even decline [2]. Although no decline in $\mathrm{AI/AI^*}$ was predicted by the proposed model, flattening was noticeable in the model outputs with age progression: there were only 1.3% and 2.8% increases in radial AI (case III) between 65-75 years for men and women, respectively. This $\mathrm{AI/AI^*}$ flattening is due to the flattening of reflection time, since the other influence on AI is the reflection coefficient, which only increases slightly with age [127]. Thus, our model suggests that the observed flattening in $\mathrm{AI/AI^*}$ is due to age-related increases in vascular resistance and more importantly, a slowing of the rate of decrease in compliance with age.

3.5.1 Study Limitations

The proposed model is based on a set of theoretical assumptions that describe simplified relationships between desired vascular ageing indices and comprehensible model elements. As such, the model is subject to practical limitations that hinder its validity.

Theoretical Assumptions: The Taylor series expansion in (3.11) only holds for small values of the arctangent argument, x, i.e., $|x| < 1$. However, based on published values [121], we have $\max(x) = 0.50$ radians, making this assumption reasonable for our model.

By assuming a lossless TL, we do not account for reductions in pressure as the pressure wave propagates along the vessel. In reality, the reflected waves lose power as they travel towards the heart. Thus, we may overestimate $|\Gamma(0)|$ in estimating the augmentation index. Nonetheless, the results are less affected in distal arteries, as $|\Gamma(0)|$ is not a dominant factor in the calculation of AI. This is because 1) Z_0 increases 2) the reflection time is shorter and, thus, $\cos \omega T_{\mathrm{refl}}$ becomes the dominant influence on the AI.

Practical Limitations: In practice, calculation of the peak-to-peak time difference between the forward and backward waves is difficult, especially in proximal arteries where forward and backward waves do not have separate peaks. Accordingly, various methods have been developed for calculating the return of reflected waves. $\mathrm{T_{refl}}$ is calculated in [127] (case I) using the 4th derivative method [138], which is referred to as the *shoulder time* T_{sho} in [110]. Whereas [133] (case IV) uses the timing of the inflection point, T_{inf}, as described in [110]. Wave separation analysis can also be used to calculate the

time difference of the forward and backward waves using the zero-crossing point of each waveform, which is called $T_{\text{f-b}}$ in [110]. The theoretical approach used in this chapter uses the peaks of the forward and backward waves to calculate $\mathrm{T_{refl}}$, which is different to the definition of $T_{\text{f-b}}$ as each wave shows different rise time from the zero-crossing point to the peak. However, the modelled $\mathrm{T_{refl}}$ best matches the definitions of T_{sho} and T_{inf} in [110].

The study is limited by scarcity of reported measurements that could be used as model input parameters. In particular, age-related increases in systemic vascular resistance have only been reported in a small number of papers. Although linear increases in R with age were reported in [139] and [14], it was suggested that R values are underestimated in older subjects [128]. More investigation is required to accurately model changes in R with age.

3.6 Conclusion

In this chapter, $\mathrm{T_{refl}}$ and AI, the two widely used pressure waveform indices, are formulated using a TL model. Derived formulas were successfully applied to data from the literature. The results confirm the dependency of both indices on the vascular ageing indicators of compliance, PWV and systemic vascular resistance. The model is able to explain the flattening of $\mathrm{T_{refl}}$ that has been repeatedly reported in the literature, as well as the moving of the reflection site, which is a subject of ongoing controversy. We also showed that a larger portion of $\mathrm{T_{refl}}$ might be due to the delay caused at the load by the compliance at the reflection point. Overall, our results suggest that $\mathrm{T_{refl}}$ is strongly influenced by vascular compliance and represents a useful index of it in populations younger than 65 years. In older populations $\mathrm{T_{refl}}$ remains influenced by vascular compliance but to a lesser degree as there is an exponential increase in vascular resistance after 50 years, which has an opposite effect on $\mathrm{T_{refl}}$. AI is itself inversely dependent on $\mathrm{T_{refl}}$ and so shows similar flattening with age; however, it is also strongly affected by HR, which influences AI values independently of vascular compliance.

Chapter 4

Indexing Cerebrovascular Health Using TCD

4.1 Introduction

Due to the well-documented association between changes in compliance and serious brain pathology, as outlined in Chapter 2 there has been considerable research into techniques that measure changes in cerebrovascular compliance. In the cerebral vessels the pressure wave cannot be measured directly, however, indices based on the pressure wave, such as AI, have been applied to blood flow and blood flow velocity waveforms which can be measured in the brain. Currently, the most common method to assess changes in cerebrovascular compliance is TCD. As mentioned in Chapter 2, TCD is a non-invasive technique that has been preferred because it is considered to be safe, cost-effective and relatively fast to perform. TCD is based on the *Doppler effect*: ultrasonic waves of a given frequency as emitted into the body and reflected at a different frequency by blood cells moving within vessels. This difference in frequency is directly proportional to the speed of the blood cells [140]. TCD is recognized to have excellent temporal resolution, making it ideal for capturing information on blood flow dynamics.

Importantly, TCD can not measure compliance directly. However, several indirect indices have been developed, including the PI, explicitly derived for the TCD waveform, and AI, based on the pressure wave AI measure, which are considered to provide reasonable approximations, see (2.23) and (2.22), respectively. The pulsatility index is the most commonly reported indirect measure of vascular health in the literature. $\mathrm{PI}_{\mathrm{TCD}}$, first defined by Gosling and King in 1974, is derived from the peak-to-peak height of the flow velocity waveform divided by the mean flow velocity (see (2.23)) [54]. Consistent with the idea that $\mathrm{PI}_{\mathrm{TCD}}$ is an index of vascular health, it has been shown to correlate robustly with age [52, 58, 69] and aortic PWV [52]. Studies have reported correlations between $\mathrm{PI}_{\mathrm{TCD}}$ and white matter disease [64, 65], diabetes mellitus [62] and dementia

[57].

There have been different interpretations of which particular vessel properties influence PI_{TCD} measurements. Some have proposed that PI_{TCD} measures CVR at the reflection site [21, 55–57, 65], while other studies have reported inconsistent results [141–144]. Following the discovery of vascular compliance, it has been hypothesized that as vessels lose their compliance and become stiffer, the peak systolic (maximum) flow velocity increases and the end-diastolic (minimum) flow velocity decreases, which elevates the calculated PI_{TCD} values [64]. More recently, PI_{TCD} has been modelled as a combination of resistance, compliance, PWV and HR [58]. Consequently, PI_{TCD} is now often reported as a general index of cerebrovascular health.

The second commonly used index of compliance is the augmentation index. AI was initially defined for the pressure waveform [108] and has been correlated with vascular ageing and aortic PWV [121]. AI captures the reflected wave augmentation of the peak pressure by calculating the ratio of the reflected wave amplitude to the systolic wave amplitude with higher values said to result from earlier arrival of the reflected wave due to stiffer arteries. The AI index has been applied to TCD flow velocity waveforms in several studies [53, 145], and a significant positive correlation between MCA AI_{TCD} and age has been reported ($r = 0.54$, $n = 286$ [59]; see Table 2.2 for more age correlations). However, several studies have questioned the reliability of using AI as an indicator of vascular compliance [2, 63, 146]. Studies have shown that AI also correlates with numerous biological factors not directly related to vessel properties including sex, heart rate, food intake, hydration status, height, weight and body composition [2].

An alternative TCD index to PI and AI, which may provide a more direct measure of vessel health, is a time-based index directly measures the reflection time. In Chapter 3, we provided mathematical proof that a timing index can accurately reflect vascular properties, has a clear relationship with vascular resistance, vascular compliance and PWV, and is not influenced by biological factors that are independent of vessel properties. In this chapter, we define a TI_{TCD} as the inverse of the interval between the systolic and reflected waveform peaks in a TCD signal. Thus, TI_{TCD} will track the timing of the blood waves in a similar way to PWV, which is the gold standard for quantifying vascular stiffness in central arteries. After introducing the new TI, we investigate the correlations between three TCD indices (PI, AI and TI) and other accepted measures of vascular ageing such as the PI_{MRI}, age and CRF.

4.2 Methods

Data from two different sets of experiments have been used in this study. Experiment one is a new study including Doppler, MRI and CRF whereas the second experiment uses Doppler recordings from an existing dataset.

4.2.1 Experiment 1

Data from 38 adult volunteers (23 female and 14 male, age range = 24-66 years, mean age = 41.7 years) were recorded, which we will refer to as dataset D1. Participants were recruited from the local community of Newcastle, Australia and provided informed consent prior to assessment. The study protocol was approved by the University of Newcastle Human Research Ethics Committee and registered in the Australian New Zealand Clinical Trials Registry (ACTRN12619000144112). Height, weight, age, gender and resting HR were recorded and participants completed a physical activity questionnaire. Data acquisition was carried out over two imaging sessions on two consecutive days for each participant. Participants were asked to refrain from caffeine consumption before their scans. However, it was not an exclusion criterion of the study.

TCD ultrasound (DopplerBox X; Compumedics DWL, Singen, Germany) at a sampling rate of 100Hz was used to record cerebral blood flow velocity from the right and left MCAs. Participants wore a headpiece with bilateral Doppler probes which stayed in place for the 300 seconds of resting-state recording. In this session, the resting-state HR was measured using an HR monitoring device (Omron HEM-7320 HR). Participants were in a sitting position for approximately five minutes during headpiece setup before recording took place. During TCD recording, HR was measured once per minute for three minutes. The average of the three HR measurements was used as the resting-state HR.

The participants were also scanned on a 3T MRI scanner (Magnetom Prisma, Siemens Healthineers, Erlangen, Germany), equipped with 64-channel receive-only head coil, while a standard built in dual channel body coil was used for radio frequency (RF) transmission. Blood flow was quantified using a PC flow quantification sequence (TR = 26.5ms, TE = 6.9ms, slice thickness = 5mm, matrix 256 $\times$ 256). A single excitation with a velocity encoding value of 120cm s^{-1} was used to quantify blood flow in MCAs [147, p. 161-175]. The TCD and MRI scan sessions were held on two consecutive days.

Two subjects did not produce usable Doppler recordings and were excluded from further analysis. Another three did not produce MRI data and were excluded from the Doppler versus MRI comparison.

4.2.2 Experiment 2

This experiment was carried out using data from previous TCD experiments examining cognitive performance, some of which has been published in [148, 149]. The aim of using this dataset, which we will refer to as D2, was to uncover the relationships between TCD indices and age in a sample with a wide age range that included older participants, as consistently lower correlations have been reported between PI_{TCD} and age in samples comprising narrower, younger age ranges. [51, 52, 61, 62, 69, 70]. Sample D2 had 55

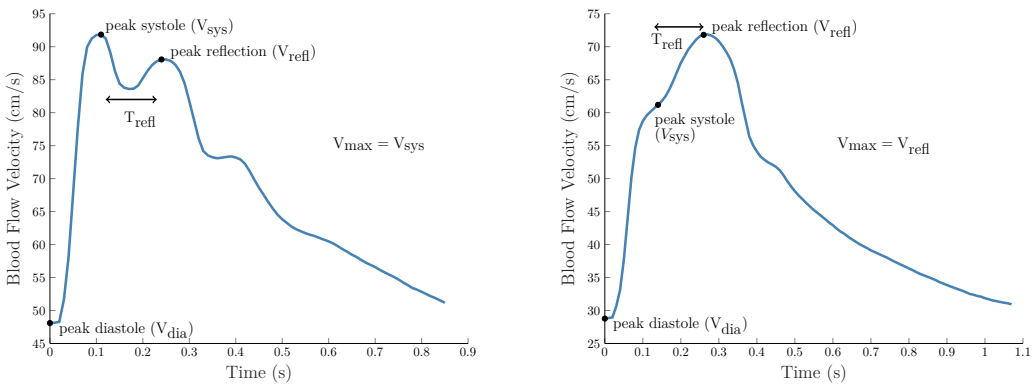

(A) (B)

FIGURE 4.1: Two different TCD flow velocity samples from D1. (a) Averaged MCA, subject #22, age 25 years (b) Averaged MCA, subject #17, age 66 years

subjects (34 female 21 male, age range = 21-80 years, mean age = 45.8 years). The data was recorded with the same device as used in Experiment 1. The recording time was shorter than Experiment 1 and varied between subjects. Data were inspected manually for each subject and a 10-second-long segment with the highest quality was selected for further analysis. During manual inspection three subjects were excluded from the initial dataset as peak detection was not possible due to excessive noise levels during their recordings.

4.2.3 Calculated Indices

$\mathbf{PI_{TCD}}$: Indices were calculated for both D1 and D2 using the same algorithms. The $\mathrm{PI_{TCD}}$ was output by the device, with values averaged per subject. The device calculated $\mathrm{PI_{TCD}}$ as defined in (2.23) [54]; i.e:

$$\mathrm{PI_{TCD}} = \frac{V_{\max} - V_{\min}}{\overline{V}}, \tag{4.1}$$

where $V_{\max}$, $V_{\min}$ and $\overline{V}$ are the maximum, minimum and mean flow velocities, respectively. A transcranial Doppler pulsatility index, alternative definition ($\mathrm{PI^*_{TCD}}$), uses $V_{\mathrm{sys}} - V_{\mathrm{dia}}$ in the numerator which are the peak systolic and end-diastolic velocities, respectively. Both indices provide the same values in most cases. Differences arise when V_{sys} and $V_{\max}$ have different values (see Fig. 4.1b for an example). This is the case in older populations and in stiffer arteries, where the forward and the reflected waves meet early and V_{sys} is in the form of an inflection point, whereas $V_{\max}$ becomes the reflected wave peak V_{refl} (see Fig. 4.1b). Nonetheless, we compared $\mathrm{PI_{TCD}}$ values output by the device with manually calculated $\mathrm{PI^*_{TCD}}$ values derived from our experimental data and found no notable differences. Therefore, only $\mathrm{PI_{TCD}}$ values directly calculated by the device are reported in this chapter.

$\mathbf{AI_{TCD}}$: In order to calculate the augmentation index, first end-diastolic points were extracted automatically using Matlab software by finding the end-diastolic points (minimum flow velocity points) in each 300- or 10-second-long signal for Experiment 1 and 2, respectively. The end-diastolic points were used to determine each cardiac cycle which were then averaged to produce a short, single-heartbeat-long waveform measurement per vessel. Next, the systolic peak, V_{sys}, and reflected peak, V_{refl}, were located manually on the waveform and AI_{TCD} was calculated as per (2.22); i.e.:

$$\text{AI}_{\text{TCD}} = \frac{V_{\text{refl}} - V_{\text{dia}}}{V_{\text{sys}} - V_{\text{dia}}}. \tag{4.2}$$

AI_{TCD} values were averaged across both MCAs, providing a single value per subject.

$\mathbf{PI_{MRI}}$: The magnetic resonance imaging pulsatility index is defined similarly to the transcranial Doppler pulsatility index as mentioned previously in (2.27) which is [79, 150]

$$\text{PI}_{\text{MRI}} = \frac{Q_{\text{max}} - Q_{\text{min}}}{\overline{Q}}, \tag{4.3}$$

where Q is blood flow ($\text{ml}\,\text{s}^{-1}$) and the bar sign indicates the mean value. MRI scanner software (Siemens Syngo) was used to quantify flow values by placing a region of interest around the MCA. The flow values for every repetition time (TR) produced waveforms for the length of the heart beat, for which the maximum, minimum and mean values were used to calculate PI_{MRI} following the method in [150]. Unlike TCD, for which only flow velocity is available, MRI measures of PI consider flow (which combines flow velocity with vascular cross-sectional area) and are more closely tied to the definition of compliance. From the 33 subjects of D1, PI_{MRI} was calculated either for both MCAs ($n = 20$) or a single MCA ($n = 13$) based on data quality. All the indices from the right and left MCA were averaged for each subject.

CRF: CRF was estimated based on a non-exercise method developed by [151], using information such as age, gender, body mass index, resting-state HR and physical activity score. CRF was acquired in two steps: 1) A physical activity questionnaire (Table 4.1) and 2) Equation (4.4), as listed below.

$$\begin{aligned}\text{CRF} = &+ 2.77 \times (0 \text{ for women, } 1 \text{ for men}) \\ &- 0.10 \times (\text{Age in years}) \\ &- 0.17 \times \left(\text{Body mass index in kg/m}^2\right) \\ &- 0.03 \times (\text{Resting HR in bpm}) \\ &+ 1.00 \times (\text{Physical activity score}) \\ &+ 18.07\end{aligned} \tag{4.4}$$

Physical Activity Description	**Score**
Inactive or little activity other than usual daily activities	0.00
Regularly (≥5 d/wk) participate in physical activities requiring low levels of exertion that result in slight increase in breathing and heart rate for at least **10 minutes** at a time	0.32
Participate in aerobic exercises such as brisk walking, jogging or running, cycling, swimming, or vigorous sports at a comfortable pace or other activities requiring similar levels of exertion for **20 to 60 minutes** per week	1.06
Participate in aerobic exercises such as brisk walking, jogging or running at a comfortable pace, or other activities requiring similar levels of exertion for **1 to 3 hours** per week	1.76
Participate in aerobic exercises such as brisk walking, jogging or running at a comfortable pace, or other activities requiring similar levels of exertion for **over 3 hours** per week	3.03

TABLE 4.1: Physical activity questionnaire [151]

Proposed Index: The proposed index relies on information from both forward and reflected waves; however, unlike AI, which is amplitude based, the new index only uses the time information. Here, we define the TCD reflection time (T_{refl}) as the time difference between the occurrence of peak systole and the reflected shoulder of peak systole (in cases of augmented waveforms) or the time difference between two distinct positive peaks (in cases of separated forward and reflected waves; see Fig. 4.1). Then, we define TI_{TCD} as:

$$\text{TI}_{\text{TCD}} = \frac{1}{T_{\text{refl}}}, \tag{4.5}$$

so that TI_{TCD} will be an index of vascular stiffness. TI_{TCD} was calculated for both MCAs using custom Matlab® software and then the values were averaged for each subject.

4.2.4 Statistical Analysis

Statistical analysis was conducted using Matlab®. The normality of the data distributions was tested using the Lilliefors test with a 5% significance level. The correlation coefficients were calculated using Pearson's correlation for normally-distributed data and Spearman's correlation for non-normal data. Bonferroni corrections with initial $\alpha = 0.05$ were made for multiple comparisons, resulting in an adjusted level of significance of 0.0056 for Experiment a and 0.0167 for Experiment 2.

4.3 Results

The correlation matrixes for Experiment 1 and Experiment 2 are shown in Table 4.2. Significant correlations have been marked after adjustment for multiple comparisons. Related scatter plots and least square lines are shown in Figs 4.2 and 4.3. For D1, two older subjects with high CRF values for their age are marked by orange arrows (←)

	Age	PI_{MRI}	CRF
PI_{TCD}	$-0.25(0.15)$ $[-0.55, 0.10]$	$0.04(0.87)$ $[-0.33, 0.38]$	$0.10(0.55)$ $[-0.17, 0.36]$
AI_{TCD}	$0.68^*(0.44e{-5})$ $[0.45, 0.83]$	$0.38(0.028)$ $[0.03, 0.64]$	$-0.65^*(0.15e{-4})$ $[-0.80, -0.43]$
TI_{TCD}	$0.70^*(0.19e{-5})$ $[0.49, 0.84]$	$0.53^*(0.002)$ $[0.23, 0.75]$	$-0.79^*(0.14e{-7})$ $[-0.89, -0.58]$

	Age
PI_{TCD}	$0.44^*(0.0009)$ $[0.17, 0.65]$
AI_{TCD}	$0.61^*(0.26e{-5})$ $[0.42, 0.74]$
TI_{TCD}	$0.50^*(0.0001)$ $[0.23, 0.68]$

TABLE 4.2: Correlation matrix for experiment one (left) and experiment two (right) reported as $r(p\text{-value})[95\%$ confidence interval$]$. Correlations found to be significant after Bonferroni correction for multiple comparisons are marked by an asterisk.

in Figs 4.2 and 4.3. Figure 4.2 shows that, unlike AI_{TCD} and PI_{TCD}, TI_{TCD} is able to distinguish these subjects from other aged individuals. These cases suggest that TI may better reflect the age-independent impact of CRF on vessel health, which is one of the key aim of vessel health measures.

In Experiment 1, PI_{TCD} did not have any significant correlation with age, CRF or PI_{MRI}, and the observed weak correlation with age was negative. The AI_{TCD} and TI_{TCD} both correlated significantly with age. Although the correlations with age are similar, TI_{TCD} has a stronger correlation with CRF. Among the three Doppler indices only TI_{TCD} has a significant correlation with PI_{MRI}.

In Experiment 2, all three Doppler indices PI_{TCD}, AI_{TCD} and TI_{TCD} correlated significantly with age. The correlation coefficients were higher for AI_{TCD} and TI_{TCD} than PI_{TCD}.

In the scatter plots of Fig. 4.2, there seem to be outliers marked by green squares. The data for these subjects were carefully re-analysed but we found no reason to remove them. However, if these subjects were removed the correlation coefficients would be $r_{D1} = -0.12$ (not significant) and $r_{D2} = 0.53$ for PI_{TCD} and age.

4.4 Discussion

The PI_{TCD} is the most commonly used and easy-to-calculate Doppler index. To understand the controversy in the interpretation of PI_{TCD}, it is useful to consider the mathematical model developed in [58] that extends the single-element model of [152] to a WK3 which describes PI_{TCD} as:

$$PI_{TCD} = \frac{p_{HR}}{CPP} \times \sqrt{1 + (2\pi f_{HR} \times CVR \times C)^2}, \tag{4.6}$$

where PI_{TCD} is defined as the fundamental harmonic of the flow velocity divided by the mean flow velocity. Variable p_{HR} is the fundamental harmonic of arterial pulse pressure,

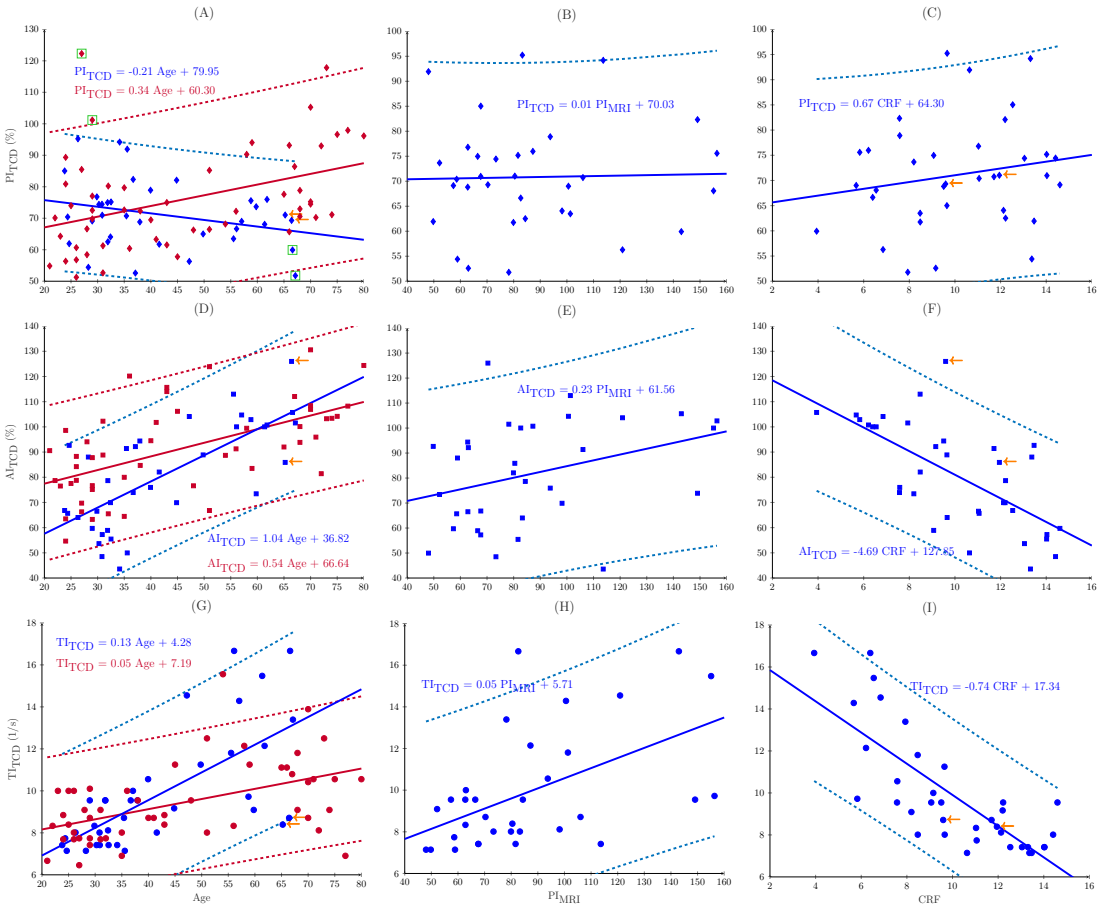

FIGURE 4.2: TCD indices plotted against health indices. The solid lines show least-square fits, and the dashed lines show the 95% confidence bounds, D1 is in blue and D2 is in red.

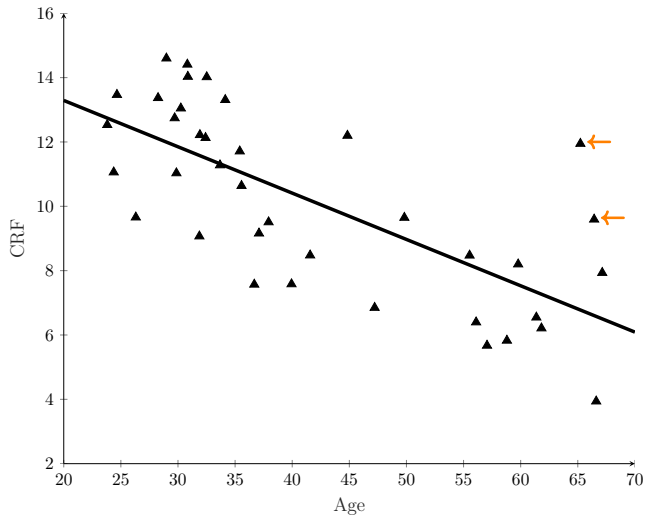

FIGURE 4.3: CRF changes with age in D1 with linear least-square fitted.

f_{HR} is HR frequency, C is cerebrovascular compliance and CPP is cerebral perfusion pressure (the driving source of blood inside the cerebrum) [58, 153]. The main point to consider in (4.6) is that although CVR and C affect $\mathrm{PI}_{\mathrm{TCD}}$ positively, they each change in different directions with age; i.e., CVR increases whereas C decreases. In younger adults, these effects may cancel each other out; hence, the lower correlations between $\mathrm{PI}_{\mathrm{TCD}}$ and age ($r_{\mathrm{D1}} = -0.25$, insignificant) and CRF ($r_{\mathrm{D1}} = 0.10$, insignificant). However, in older adults, the increased stiffness, or decreased C, may have a dominant effect, resulting in a strong decrease in $\mathrm{PI}_{\mathrm{TCD}}$ even when CVR is increasing. This can explain the low correlations of $\mathrm{PI}_{\mathrm{TCD}}$ with age in younger adults reported in the literature [61, 70]. Our results confirm this for D1, which comprised a relatively young population, where the correlation between $\mathrm{PI}_{\mathrm{TCD}}$ and age is negative ($r_{\mathrm{D1}} = -0.25$, insignificant). For D2 ($r_{\mathrm{D2}} = 0.44$), $\mathrm{PI}_{\mathrm{TCD}}$ exhibits a greater increase after the age of 65, as shown in Fig. 4.2.

The $\mathrm{PI}_{\mathrm{MRI}}$ is a different predictor of vascular ageing than $\mathrm{PI}_{\mathrm{TCD}}$ that considers blood volume changes rather than blood velocity changes. Compliance is the change in blood volume relative to changes in pressure. An MRI, which measures blood flow (i.e., volume per unit time), can more accurately track volume changes than TCD. If the vascular cross-sectional area was known, or if it was constant, it would be possible to derive blood flow from blood velocity. However, changes in vascular cross-sectional area can not be assumed to be constant, as it is these changes that actually define compliance. In fact, a subtle assumption used in deriving (4.6) is that the vascular cross-sectional area is constant, which is particularly problematic in younger subjects with compliant arteries. Thus, the uncorrelated $\mathrm{PI}_{\mathrm{TCD}}$ and $\mathrm{PI}_{\mathrm{MRI}}$ results ($r_{\mathrm{D1}} = 0.04$, insignificant) can be explained by the younger composition of D1 and also the lack of cross-sectional area information in $\mathrm{PI}_{\mathrm{TCD}}$.

The AI is strongly related to vascular ageing factors [154]. Assuming a TI with a WK3 as the load, the AI in the pressure waveform can be formulated as [154]:

$$\mathrm{AI} \approx \frac{2}{3}\left(\cos\left(2\pi f_{\mathrm{HR}} T_{\mathrm{refl}}\right) + |\Gamma(0)| + \frac{1}{2}\right), \tag{4.7}$$

where $\Gamma(0)$ is the *reflection coefficient*, which equals the amplitude of the reflected wave divided by the amplitude of the forward wave, measured at the load site [154]. As seen in (4.7), the AI includes T_{refl} and the reflection coefficient, where are both reported to change significantly with age [105, 127]. For AI calculated using the Doppler-based velocity waveform these factors are assumed to contribute in the same way as we have shown significant correlations of $\mathrm{AI}_{\mathrm{TCD}}$ with age ($r_{\mathrm{D1}} = 0.68$ and $r_{\mathrm{D2}} = 0.61$), CRF ($r_{\mathrm{D1}} = -0.65$) and $\mathrm{PI}_{\mathrm{MRI}}$ ($r_{\mathrm{D1}} = 0.38$, insignificant). However, HR is another contributing factor to $\mathrm{AI}_{\mathrm{TCD}}$ (see (4.7)), a dependency that has also been reported in practice [155]. This is a factor that may affect AI independently of vascular compliance or resistance [146].

The timing-based index TI has a strong relationship with vascular compliance. In the context of the pressure waveform, evidence of change in the time of reflected waves with age have been presented on practical [105] and theoretical bases [154]. As initially suggested in [118] and then mathematically modelled in [154], the time difference between the forward- and the backward-travelling pressure waves (i.e., $\mathrm{T_{refl}}$) can be given as:

$$T_{\mathrm{refl}} \approx \underbrace{\frac{2Z_0 \times \mathrm{CVR} \times C}{\mathrm{CVR} + 2Z_0}}_{\Delta t_{\mathrm{load}}} + \underbrace{\frac{2d_0}{\mathrm{PWV}}}_{\Delta t_{\mathrm{line}}}, \tag{4.8}$$

where Δt_{line} is the time delay between the two waves caused by the length of the arteries, Δt_{load} is the delay at the reflection site due to the compliance of the vessels beyond that point and Z_0 is the characteristic impedance. The line delay is inversely proportional to the pulse wave velocity; i.e., $\Delta t_{\mathrm{line}} \propto 1/\mathrm{PWV}$. In addition, the load delay is proportional to the compliance of the vascular bed (i.e., $\Delta t_{\mathrm{load}} \propto C$) and will also decrease as the compliance of the vessels distal to the measurement site decreases with ageing. Therefore, we would similarly expect $\mathrm{TI_{TCD}}$ to be highly dependent on vascular compliance. The significant correlations of $\mathrm{TI_{TCD}}$ with age ($r_{\mathrm{D1}} = 0.70$ and $r_{\mathrm{D2}} = 0.50$), CRF ($r_{\mathrm{D1}} = -0.79$) and $\mathrm{PI_{MRI}}$ ($r_{\mathrm{D1}} = 0.53$) support this assumption. We can examine the stronger correlation of TI with CRF than age by considering older subjects with higher CRFs (see the two subjects tracked by arrow signs in Figs 4.2 and 4.3). We hypothesize that the timing index is a predictor of vascular health that is independent of age, while AI more closely predicts age than CRF. An ideal index of vascular health would not necessarily have a strong correlation with age as lifestyle choices can significantly affect vascular health over time. Specifically, age related progression of aortic and carotid stiffness has been shown to be slower in old participants with a history of high cardiovascular fitness than in those with a history of low fitness [99].

It should be noted that indices that are influenced by the reflected wave (TI and AI explicitly, and PI in some cases) implicitly assume that the distance of travel of the reflected wave is consistent across subjects, such that differences in the timing and amplitude of the reflected wave solely reflect differences in compliance. In the aorta, the gold standard measure of aortic stiffness explicitly estimates the travel distance along the aorta, through external measurement and modelling, then calculates the PWV as the ratio of distance to time difference. This is more difficult to do in the brain.

In general, the application of pressure waveform indices to the Doppler waveform must be done with care due to the differences between the two waveforms. While we often think of a single reflected wave, in reality there are many reflected and re-reflected waveforms that comprise an observed signal. In order to investigate the influences of these factors, a simulated flow waveform is shown in Fig. 4.4 (a simpler form of the ones reported in the literature [156]) which illustrates the underlying reflected and re-reflected

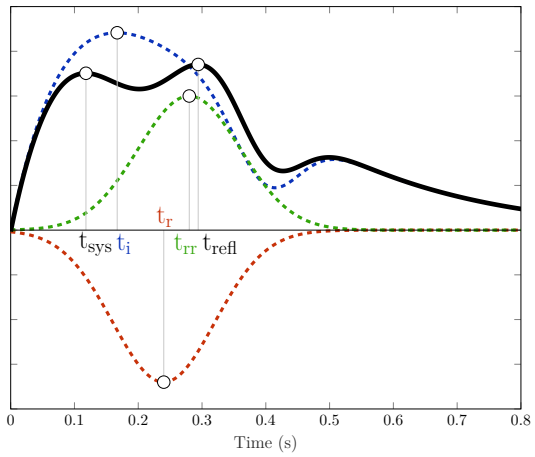

FIGURE 4.4: Simulated flow velocity signal to demonstrate summation of incident, reflected and re-reflected waves. Blue, green and red dashed lines represent the incident forward traveling wave, the re-reflected wave and the reflected wave, respectively. Solid line is the sum of the three waveforms. t_{sys} and t_{refl} are the time of observed systolic and observed reflected peaks. t_{i}, t_{r} and t_{rr} correspond respectively to time of incident, reflected and re-reflected peaks.

waveforms. The reflected flow velocity (i.e., blood that travels toward the heart) is recorded with a negative amplitude by the Doppler device and thus is subtracted from the forward waves. The re-reflected flow, however, is reflected twice during the cardiac cycle and travels in the same direction as the original forward wave. This waveform has a positive amplitude when its velocity is measured by the Doppler device. Note that both reflected and re-reflected waveforms have positive amplitudes on pressure readings. Therefore, Doppler-measured velocity waves will have a different shape to pressure waves and the use of the Doppler indices taken from pressure studies must be done with care. However, based on Fig. 4.4, we can see that an observed reflected peak is more influenced by the re-reflected wave. In other words, the reflected wave plays a part in forming a negative dip between the observed forward and reflected peaks and V_{refl} is mainly determined by the re-reflected wave. Further, in practice, comparison of simultaneously recorded pressure and flow velocity waveforms has shown that the characteristic time points used in the definitions of AI and TI are similar in both waveforms [53]. This suggests that, in both pressure and flow velocity waveforms, the reflection time, pulsatility index and AI not only account for the reflected wave but also a combination of reflected and re-reflected waves. It also suggests that the stiffness / compliance measured through PI, AI or TI may be equally affected by the upstream and more distal cerebral arteries. Given the similarity of timing of the second peak in the pressure and flow velocity waveforms, we continued to use this second peak for our derivation of both the AI and TI indices. Nonetheless, to our knowledge, there are no TCDs timing indices that consider the effects of the negative reflected wave in the flow velocity waveform. This could be considered in future work.

There are several limitations to the design of the study described in this chapter, which could potentially affect the measured variables. The study was conducted on two consecutive days and the MRI and TCD were measured with the subject in different positions; i.e. supine and sitting, respectively. However, the resting state was established by having the subjects 1) sit for at least 5 minutes during the TCD headpiece set-up and 2) spend at least 5 minutes in the supine position during the MRI session to acquire other sequences. In addition, CRF measurement, which required HR measurements was performed on the day of TCD measurement and was not repeated.

4.5 Conclusion

The most commonly used TCD index, PI_{TCD}, should be interpreted with caution due to its complex relationships with CVR and vascular stiffness/compliance. Each has opposite effects on this index, resulting in PI_{TCD} having a weak correlation with age and no correlation with CRF. On the other hand, AI_{TCD} and the proposed TI_{TCD}, both showed strong correlations with age, thereby linking them with vascular ageing. In addition, of all the Doppler indices, TI_{TCD} had the strongest correlation with CRF and MRI, suggesting that this index may be a suitable replacement for PI_{TCD} and AI_{TCD} for indexing cardiovascular health.

Chapter 5

A Mathematical Model of the NiRS Signal

5.1 Introduction

In Chapters 3 and 4, we used transmission line (TL) theory to prove that the timing of the reflected pressure wave is determined by vascular health factors such as compliance, resistance and PWV. Then, we introduced the same concept to TCD blood flow velocity waveforms to create a new timing index – the TI_{TCD}– and showed it to be strongly correlated with age and PI_{MRI}. Furthermore, its correlation with CRF is even stronger than those of existing indices such as the AI_{TCD} and PI_{TCD}. Our next goal is to assess the feasibility of indexing cerebrovascular health using NiRS.

As discussed in Chapter 2, NiRS uses the near-infrared portion of the electromagnetic spectrum to emit light into the brain. The light is scattered and a very small portion finds its way to light detectors placed $2 - 5$cm away from the source [84]. Over this spectrum light is mainly absorbed by oxygenated and de-oxygenated blood which have different absorption coefficients. Using at least two wavelengths one can separate signals from oxy- and deoxy-haemoglobin as indicators of brain activation [84]. NiRS has several advantages compared to other methods of brain study. Its low cost, portability and high temporal resolution makes NiRS a worthy alternative to the well-known fMRI techniques. NiRS also offers higher spatial resolution than EEG, thereby allowing regional studies.

Due to the large number of biological components (HR, respiration, Mayer waves, reflected waves, haemodynamic responses) and instrumental components in a NiRS signal, various signal processing methods have been used to extract components of interest, such as the haemodynamic response function (HRF) [84] or arterial pulsation (AP) signal [10, 86]. As the true signal (ground truth) of the desired component is not known in any given NiRS dataset, it is difficult to compare the effectiveness of signal processing

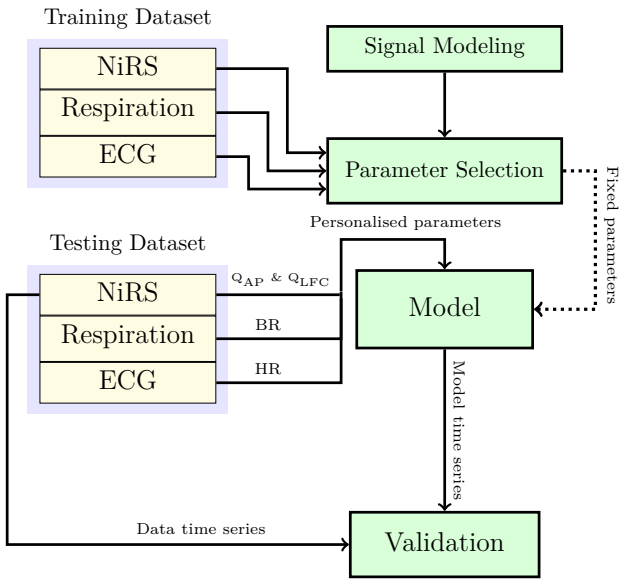

FIGURE 5.1: Flowchart of the processes of the proposed model

algorithm. A common approach is to create a realistic model of the signal of interest, for which the ground truth is known exactly, to facilitate design and analysis of signal processing algorithms. Synthetic models have been proposed for different biomedical signals and their sub-components such as ECG [157], EEG [158] and fMRI [159]. One study [160] proposed a superposition of three sinusoids (HR, respiration and HRF) to reconstruct NiRS scattering and absorption coefficients. However, to the best of our knowledge no stand-alone synthetic signal model has been proposed for use with NiRS signals. Such a model would need to accept basic physiological inputs like HR and breathing rate (BR) and montage related inputs to synthesise realistic NiRS signals.

In this chapter, we study different components of NiRS signals and present a novel model for generating artificial NiRS time series that have the same time and frequency features as intensity-normalized in vivo NiRS signals. We input features like signal power, BR and HR to the model and assess the validity of output using a test dataset (see Fig. 5.1). This way, the model can generate synthetic signals similar to the recorded testing set. Finally, the in vivo and synthetic signals are statistically compared. The results demonstrate a significant similarity between the two. This will be a step towards better understanding all the underlying elements of NiRS signals before constructing a NiRS-based index of cerebrovascular health.

5.2 Protocol and Data Collection

For parameter selection and model validation, NiRS data from 25 adult volunteers were recorded (15 female, 10 male, age range = 24-67 years, mean age = 39.3 years). Participants were recruited from the local Newcastle population and provided informed consent in accordance with the University of Newcastle Human Research Ethics Committee. Participants were instructed to relax and sit still for 300 seconds of resting-state NiRS recording. The setup consisted of four detectors, each crossed with 16 time multiplexed sources (half operating at 690nm and half at 830nm), making a total of 64 channels. A frequency domain NiR spectrometer (ISS Imagent^{TM}, Champaign, Illinois) with a 110MHz modulation frequency operating at a rate of 39.0625Hz was used for data acquisition. Participants were asked to wear an Equivital EQ02 LifeMonitor sensor belt during the recording, which measured their HR and BR.

Data were randomly split into a training set (T1) and test set (E1). The recordings of five randomly selected subjects were assigned to T1 and the other 20 were assigned to E1 and used for validation purposes.

5.3 Signal Modelling

Our proposed NiRS signal model comprises the following components:

$$\mathrm{s} = \begin{bmatrix} \mathrm{a_{AP}} & \mathbf{1} & \mathrm{a_{LFC}} & \mathrm{a_{HRF}} \end{bmatrix} \begin{bmatrix} \mathrm{s_{AP}} \\ \mathrm{s_{GN}} \\ \mathrm{s_{LFC}} \\ \mathrm{s_{HRF}} \end{bmatrix} + \mathbf{1}. \tag{5.1}$$

In which s is an $N \times 1$ NiRS time series vector formed from the AP signal ($\mathrm{s_{AP}}$), additive white Gaussian noise (WGN) ($\mathrm{s_{GN}}$), LF components ($\mathrm{s_{LFC}}$) and HRF ($\mathrm{s_{HRF}}$), with N being the number of realizations. $\begin{bmatrix} \mathrm{a_{AP}} & \mathbf{1} & \mathrm{a_{LFC}} & \mathrm{a_{HRF}} \end{bmatrix}$ is an $N \times 4$ matrix of corresponding amplitudes and $\mathbf{1}$ is a $N \times 1$ vector of ones. Typically, experimental NiRS data is normalized to a mean of 1, which we did for this model. N is selected based on the desired sampling frequency, f_{s}, and the signal length is in seconds.

5.3.1 Arterial Pulsation Signal

Arterial Pulsations (APs) are the most distinguishable components of the NiRS signal as they have the highest power. These signals are the footprint of massive changes in blood volume as the heart pumps and blood is forced into cerebral arteries. This volume of blood absorbs a large portion of the optical signal and a decrease in detected light intensity becomes evident [161]. AP signals are used to extract cerebral arterial health factors because they include signals from the reflected waves [10, 86, 162] that

occur when the systolic blood volume hits arterial branches and is reflected. Reflected waves are studied physiologically via blood pressure and blood flow velocity waveforms and mathematically with TL models [46, 163–165]. NiRS recordings also show these reflected waves [10, 86, 162], which are included in our model. There are several factors that can alter AP-related variables, such as the environment temperature, body position, emotional state, exercise and medicine use. In our model, we assume a stationary participant and no changes in these factors. However, two additional key elements continuously influence HR, even in stationary participants. Firstly, it is known that HR accelerates during inspiration and slows down during expiration. This phenomenon is referred to as *respiratory sinus arrhythmia* [166]. Secondly, Mayer waves, the cause of which is debatable, result in small frequency drifts in ECG signals [157]. Due to the similar nature of AP signals in ECG and NiRS signals, we assume that these frequency drifts are also present in NiRS signals.

Ignoring reflected waves for now, we first model the respiratory and Mayer wave drifts in the AP signal. For this purpose, we use a similar concept to the "RR interval" used in ECG signal analysis. R peaks are the most distinguishable peaks in an ECG signal. An RR peak-to-peak interval is defined as the time between consecutive R peaks. Similarly, we define $p(m)$ as an RR interval time series. Now, respiratory and Mayer drifts can be modelled based on an established method that was proposed to produce synthetic ECG signals [157]. The power spectrum of $p(m)$ is described with two components as:

$$P(f) = \sum_{i=1}^{2} \frac{c_i^2}{\sqrt{2\pi\sigma_i^2}} \exp\left(\frac{(f-f_i)^2}{2\sigma_i^2}\right). \tag{5.2}$$

Where f_i, σ_i and c_i represent the centre frequency, standard deviation and power of the frequency drift, caused by the Mayer signal ($i = 1$) and respiratory signal ($i = 2$), respectively. Taking the inverse Fourier transform of $\sqrt{P(f)}$, using a random phase, $p(m)$ is generated as:

$$p(m) = \{\mathcal{F}^{-1}\left[\sqrt{P(f)}e^{j\theta}\right], \quad \theta \backsim \mathcal{U}[0, 2\pi)\}, \tag{5.3}$$

where $\mathcal{F}^{-1}$ is the inverse Fourier operator and $\mathcal{U}$ represents the uniform distribution. $p(m)$ is then normalized with the mean value set to the mean RR interval; i.e., $60/H_{\text{mean}} \times f_s$ and the standard deviation (std) set to the RR interval std; i.e., $60/H_{\text{std}} \times f_s$ (H_{mean} and H_{std} are the mean and std HR in bpm). Then, we define the systolic peaks (negative peaks) of the s_{AP} signal as:

$$\check{\text{s}}_{\text{AP}}(n) = -\text{a}_{\text{AP}}, \quad n = \sum_{i=1}^{j} p(i) \quad j = 1, ..., N_{\text{p}} \tag{5.4}$$

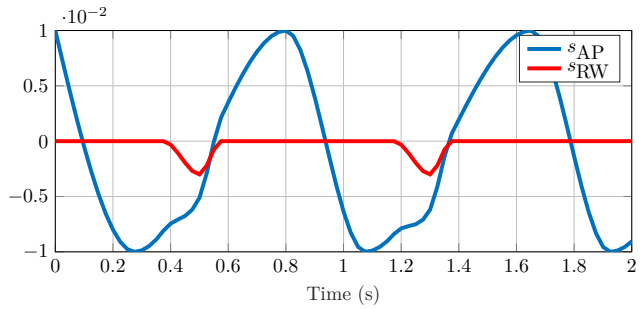

FIGURE 5.2: Sample modelled s_{AP} signal with added reflected wave, s_{RW}. Related variables are set to $f_{\mathrm{s}} = 40$, $a_{\mathrm{AP}} = 0.01$, $a_{\mathrm{RW}} = 30\%$, $\mathrm{T_{refl}}$= 0.2s and $\mathrm{r_{SD}}$= 0.7.

where $N_{\mathrm{p}} < N$ is the number of samples in $p(m)$ that satisfy our final signal length, N. Now, having the systolic peaks in our raw AP signal, we place diastolic peaks (positive peaks) between the predefined systolic peaks with the amplitude set to $+\mathrm{a_{AP}}$ and the systolic-to-diastolic duration ratio of $\mathrm{r_{SD}}$. The value of $\mathrm{r_{SD}}$ is the ratio between 1) the diastolic peak to systolic peak drop time and 2) the systolic peak to diastolic peak rise time. This helps us include different systolic and diastolic durations in our model. Finally, we perform a piecewise cubic spline interpolation to fill the remaining values in the $\mathrm{\check{s}_{AP}}$ signal.

The next step is to add a reflected wave, $\mathrm{s_{RW}}$, to the AP signal. Since the reflected waves, in theory, have the same shape as the incident waves but are inverted in time, we cut the diastolic-to-diastolic waveform, then invert it in time and scale the shape to the amplitude of a_{RW} (measured in the percentage of a_{AP}) and then add it to the $\mathrm{\check{s}_{AP}}$ signal with a systolic peak to reflect the peak delay of $\mathrm{T_{refl}}$. The result will be the $\mathrm{s_{AP}}$ signal; i.e.,

$$\mathrm{s_{AP}} = \mathrm{\check{s}_{AP}} + \mathrm{s_{RW}}. \tag{5.5}$$

Sample $\mathrm{s_{AP}}$ and $\mathrm{s_{RW}}$ signals are presented in Fig.5.2.

5.3.2 White Gaussian Noise

NiRS signals usually contain high amounts of WGN originating from the instruments at the measurement site. As the name suggests, WGN is characterized as being uniformly distributed in the frequency domain and, therefore, is easily detected in bandwidths that are clear from the influence of any other known components. This feature will be used to set the noise power. In mathematical terms,

$$\mathrm{s_{GN}}(n) \backsim \mathcal{N}(0, \sigma_n^2), \tag{5.6}$$

where $\mathcal{N}$ is a normal distribution with a zero mean and variance of σ_n^2.

5.3.3 Low-frequency Components

LF components is a general term we use to refer to the two main low-frequency elements of NiRS signals which are 1) Mayer and respiration waves (frequencies of around 0.1Hz and 0.25Hz, respectively) and 2) VLF components (<0.1Hz).

5.3.3.1 Mayer and Respiratory Waves

These two elements are known to be present in NiRS signals as reported in the literature [167, 168]. To clarify, in Section 5.3.1, we mentioned the frequency drifts that these signals cause in HR and here we discuss the amplitude changes in NiRS signals caused by the same sources. Here, we generate $p_1(n)$ as per (5.3) (with a different realization of θ and length N), then normalize it to a zero mean and unit variance. We define the Mayer and respiratory amplitude changes by

$$\mathrm{s}_{\mathrm{MR}}(n) = p_1(n), \tag{5.7}$$

which will be added to other LF components discussed in this section.

5.3.3.2 VLF Components

The VLF (<0.1Hz) components of the NiRS signal correlate with similar components in blood-oxygenation level dependent (BOLD) fMRI data [169]. Although the source of these signals is unclear, they are thought to be associated with changes in vascular dilation, vaso-motion, and Mayer waves [169]. We take advantage of the correlation between VLF BOLD fMRI and VLF NiRS signals by adopting the approaches proposed in the literature to model the VLFs in the fMRI BOLD signal [159]. The VLF part of our synthetic model is defined as:

$$\mathrm{s}_{\mathrm{VLF}}(n) = \sum_{k=1}^{K} A(k)\cos(2\pi\phi(k)n), \tag{5.8}$$

where K is the number of VLF components, A is a $1 \times \mathrm{K}$ vector of amplitudes and $\phi(k) = f_1 + (f_2 - f_1)/(K-1).(k-1)$, where f_1 and f_2 are the low and high frequency limits of the VLF elements. Finally,

$$\mathrm{s}_{\mathrm{LFC}} = s_{\mathrm{MR}} + s_{\mathrm{VLF}}, \tag{5.9}$$

5.3.4 Haemodynamic Response

The haemodynamic response function (HRF) indicates the oxy- and deoxy-haemoglobin changes occurring during certain stimulation tasks. The nature of this signal has been investigated thoroughly in the literature using data from fMRI BOLD [170, 171] and

NiRS techniques [172]. The concept of adding HRF to a resting state signal and simulating brain activation with an experimental paradigm is well understood [168, 172, 173]. The HRF varies considerably in different tasks so, any accurate model would depend on the specific experimental protocol. For illustration, we use the HRF model in [170], i.e.,

$$\begin{aligned} y(n) &= b_1 n^{n_1} e^{-n/m_1} - a_2 b_2 n^{n_2} e^{-n/m_2}, \\ b_i &= 1/\max\left(n^{n_i} e^{-n/m_i}\right). \end{aligned} \tag{5.10}$$

Where $y(n)$ is the HRF time series. The convolution of $y(n)$ with the boxcar function of the stimuli paradigm, $u(n)$, i.e.,

$$s_{\mathrm{HRF}}(n) = y(n) * u(n). \tag{5.11}$$

This will give us the haemodynamic response time series, $s_{\mathrm{HRF}}(n)$. Then, the amplitude of s_{HRF}, a_{HRF}, should be set before we add it to the modelled signal.

It is also reported that systemic parameters like HR and BR change depending on the task [174]. This can easily be implemented in the present model by allowing time-varying parameters for H_{mean} and f_2 synchronized to the s_{HRF} signal.

The final model of the synthetic NiRS signal depends on a total of 25 tunable parameters: sampling frequency, six variables for constructing $P(f)$ in (5.2), heart rate parameters, $\mathrm{r_{SD}}$ ratio, two reflected wave parameters, noise power, four parameters for determining K, A and ϕ in (5.8), two amplitude parameters in (5.1) and six parameters for the haemodynamic response.

5.4 Parameter Estimation

In this section we discuss parameter selection for our proposed model. For parameters considered in the literature we give reported values. In addition, the T1 dataset is used to calculate parameter values, see Table 5.1.

5.4.1 Measuring Power Parameters

An adequate amount of noise power, σ_{n}^2, needs to be selected to obtain a realistic model. For this purpose, we use a signal-to-noise ratio factor. For our in vivo signal, we define the noise factor as follows. Knowing the heartbeat frequency, the arterial pulsation signal is extracted with an infinite impulse response (IIR) bandpass filter with a bandwidth of 0.4Hz centred around the heart rate. The power of the resulting signal is called P_{AP}. Another IIR filter is applied to the frequency band of 6-12Hz under the assumption that this spectrum only contains WGN. The output signal power is called P_{GN}. Then, we

TABLE 5.1: Model Parameters

Parameter		Literature	T1	E1/E2
Device	f_s(Hz)	—	39.0625	39.0625/10
AP	$f_1(\times 10^{-2}\text{Hz})$	10 [168]	$[11, 10, 95, 98, 10]$	10
	$f_2(\times 10^{-2}\text{Hz})$	25 [168]	$[32, 27, 22, 22, 24]$	personalized
	c_1 $(\times 10^{-3})$	$\frac{c_1^2}{c_2^2} = 0.5$ [157]	$[28, 32, 28, 24, 32]$	29
	$c_2(\times 10^{-3})$		$[30, 30, 26, 25, 33]$	29
	σ_1(mHz)	10 [157]	$[25, 34, 18, 35, 33]$	29
	σ_2(mHz)	10 [157]	$[25, 36, 21, 29, 30]$	29
	a_{AP}	—	0.01	0.01/3
	H_{mean}(bpm)	70 [168]	$[76, 71, 71, 68, 73]$	personalized
	H_{std}(bpm)	5.0 [157]	$[3.5, 4.8, 4.0, 3.3, 4.4]$	5.0
	$a_{\text{RW}}(\%)$	—	[35, 15, 30, 20, 15]	30/NA
	T_{refl} $(\times 10^{-2}\text{s})$	—	[22, 12, 19, 5, 5]	20/NA
	r_{SD}	—	[0.4, 0.4, 0.6, 0.5, 0.6]	0.60/0.56
WGN	σ_{n}^2 $(\times 10^{-5})$	—	[2.6, 18.7, 1.6, 0.9, 9.8]	personalized
LF	K	—	100	100
	A	—	$\mathcal{U}[-1, 1]$	$\mathcal{U}[-1, 1]$
	f_1(Hz)	—	0.01	0.01
	f_2(Hz)	—	0.09	0.09
	a_{LFC} $(\times 10^{-2})$	—	[24, 4, 3, 2, 8]	personalized
HRF	n_1	5.0 [170]	NA	4.0
	n_2	12.0 [170]	NA	12.0
	m_1	1.1 [170]	NA	1.2
	m_2	0.9 [170]	NA	0.9
	a_2	0.35 [170]	NA	0.4
	a_{HRF}	1%-5% [173]	NA	NA/3%

define the AP SNR factor as:

$$\text{Q}_{\text{AP}} = 10 \log_{10} \frac{P_{\text{AP}}}{P_{\text{GN}}}. \tag{5.12}$$

Finally, the model parameter, σ_{n}^2 is set to achieve the required Q_{AP} value.

In order to set a_{LFC} to a realistic LF component signal power in our model, we use the same power-ratio strategy as (5.12). Using the T1 dataset, an IIR bandpass filter is applied to the frequency band of 0.01-0.26Hz (i.e., the LF band) to obtain a signal power of P_{LFC}; then, the SNR factor for the LF signal is defined as:

$$\text{Q}_{\text{LFC}} = 10 \log_{10} \frac{P_{\text{LFC}}}{P_{\text{GN}}}. \tag{5.13}$$

After an appropriate value is set for Q_{LFC}, a non-linear least-squares minimization problem is solved to find the right a_{LFC} for the LF components.

5.4.2 Overall Parameter Selection

The resting state model parameters are summarized in Table 5.1, in which the values suggested by the literature are compared to the measurements from the T1 dataset. The differences between the reported values for c_1, c_2, σ_1 and σ_2 of the AP signal are presumed to be the result of differences between ECG and NiRS signals. The last column of Table 5.1 provides an idea of the range of values one can use to run the

model. The E1 column of Table 5.1 is a combination of published parameter values and T1 measurements, which we will use to generate an E1-equivalent dataset using the model. We have not mentioned any default values for four of the major parameters in the model. These parameters have either subject-specific or channel-specific values, referred to as *personalised* in the table and should be selected for each individual run of the model.

5.5 Model Validation

In this section we will first illustrate a sample model output for visual comparison then use an entropy estimate to statistically compare the similarities between the model output and measured NiRS recordings in resting state using the E1 dataset. Finally, we will evaluate model outputs by comparing them with a task-included dataset.

Figure 5.3 shows an example where an in vivo NiRS recording is compared with its synthetic equivalent in time and frequency domains.

5.5.1 Validation Tool

Here, we use cross-fuzzy entropy (CFEn) as our validation tool for the assessment of model outputs. CFEn is a measure of synchrony or regularity between two time-series. CFEn is used here to measure the similarity between our model output and in vivo data. CFEn is the negative natural logarithm of the conditional probability that the two sequences which are similar for m points will remain similar for $m+1$ points. Cross fuzzy entropy was developed by [175] and then generalized in [176] by modifying cross sample entropy [177] and avoiding the two-state classification of similarity by the Heaviside function. Instead, cross-fuzzy entropy uses a fuzzy function to associate a membership grade for the similarity of two vectors. We denote the cross-fuzzy entropy of two time series $\mathbf{u} = [u_1, u_2, \ldots, u_N]$ and $\mathbf{v} = [v_1, v_2, \ldots, v_N]$ each with unit variance and N equally spaced time samples as $\mathrm{CFEn}_{\mathbf{vu}}(m, r)$. Here, m is the embedding dimension described above and r is the similarity tolerance factor.

In order to use CFEn as a validation tool for our model, we first choose the appropriate parameters for this entropy measure and then run different simulations comparing the model output and in vivo signals. The embedding dimension, m, determines the length of the sequences to be reconstructed. To have a sensible approximation it is advised to have $10^m \leq N \leq 30^m$, N being the number of samples [175, 178]. Considering the sampling frequency and acquisition period described in 5.2, we will set $m = 3$ for all our analyses, which is similar to the approach taken in [176] for analysing an EEG dataset. In all entropy estimations like approximate entropy, cross sample entropy and cross-fuzzy entropy, r is recommended to be $0.1 - 0.3$ times the data std [176, 177, 179].

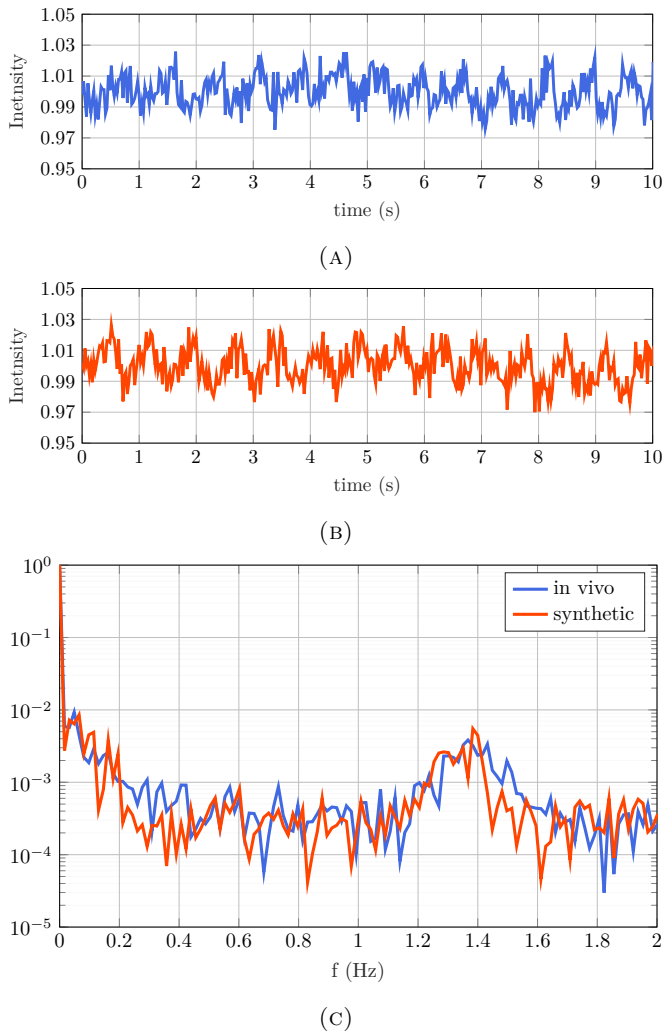

FIGURE 5.3: Visual comparison between sample channel from E1 and its synthetic NiRS equivalent. (a), (b) and (c) show an in vivo recording, synthetic-equivalent and frequency-domain comparison, respectively. The frequency domain signals are calculated using one-minute-long time domain signal. Parameters σ_{n}^2, a_{LFC}, H_{mean} and BR are measured as 2.2×10^{-5}, 0.05, 80bpm and 0.22Hz respectively. All the other parameters are set to their default E1 values as per Table 5.1.

Since in cross sample entropy the data is normalized to a unit std, we will set $r = 0.2$ as per [177].

5.5.2 Validation Using CFEn

For entropy-based validation, we first create a self-similarity index, $\check{\rho}$, for each individual channel from E1. Then, we compare $\check{\rho}$ to that of synthetically produced equivalents, ρ.

Let $\check{\mathrm{s}}_i$ for $i = 0, 1, \ldots, 758$ represent all the channels with a source-detector distance of $2 - 5$cm from our E1 dataset described in Section 5.2. In order to calculate a self-regularity index for the channels, we divide each five-minute long $\check{\mathrm{s}}_i$ sequence into 5

one-minute sequences of $\check{\mathrm{s}}_{i,j}$ for $j = 1, \ldots, 5$. Then, we define

$$\check{\rho}_i = \min_{j \in [2,3,4,5]} \mathrm{CFEn}_{\check{\mathrm{s}}_{i,1}\check{\mathrm{s}}_{i,j}}(3, 0.2), \tag{5.14}$$

as a measure of self-regularity for each channel. Analysing the data based on the chosen CFEn parameters and NiRS signal characteristics, we exclude the channels with self-regularity indexes, $\check{\rho}$, greater than 0.7. Note that a higher regularity index indicates lower self-similarity within channels. This leaves us with $n = 157$ channels for model validation.

For case I, using $\mathrm{Q_{AP}}$, $\mathrm{Q_{LFC}}$, HR and BR information for each channel we produce a one-minute-long synthetic equivalent signal using our model. Let

$$\rho_i = \min_{j \in [2,3,4,5]} \mathrm{CFEn}_{\mathrm{s}_i\check{\mathrm{s}}_{i,j}}(3, 0.2), \tag{5.15}$$

where s_i is the model output corresponding to the inputs for $i = 0, 1, \ldots, n$ channels. The second CFEn elements will be the same recorded sequences as in (5.14).

Figure 5.4a shows ρ plotted against $\check{\rho}$ for case I. Since we generated the synthetic equivalent signals based on whole 5-minute-long in vivo sequences, we expect to see higher similarity and a lower regularity index, between some of the synthetic and in vivo signals compared to the within-channel similarity measures. These are the channels that fall below the equal-regularity line in Fig. 5.4.

In order to demonstrate the practicality of using cross-fuzzy entropy in assessing NiRS data similarity, we run an additional set of simulations (case II), where we randomly compare in vivo measurements. That is, for the same $\check{\rho}_i$ in (5.14), the corresponding ρ_i is calculated as the minimum cross-entropy between all the one-minute segments of channel i compared with a random one-minute recording of another channel. The result is shown in Fig. 5.4b where most of the points show low similarity and fall over our 0.7 CFEn threshold. That is, we show that the similarity between the synthetic signal and the in vivo signal it models is significantly higher than the similarity between two separate in vivo signals.

Finally, we perform a statistical test to show the significance of equivalence between synthetic signals and in vivo measurements. To maintain the independence of samples we only use one randomly selected single channel per subject, as illustrated in Fig. 5.4a. The equivalence margin, δ, is set to 0.15. The value of δ is chosen based on 1) the within-channel EEG CFEn values reported by [176] as an external reference of CFEn variability in biomedical signals and 2) the within channel NiRS CFEn values calculated using our dataset. The equivalence tests were performed in the form of two one-sided

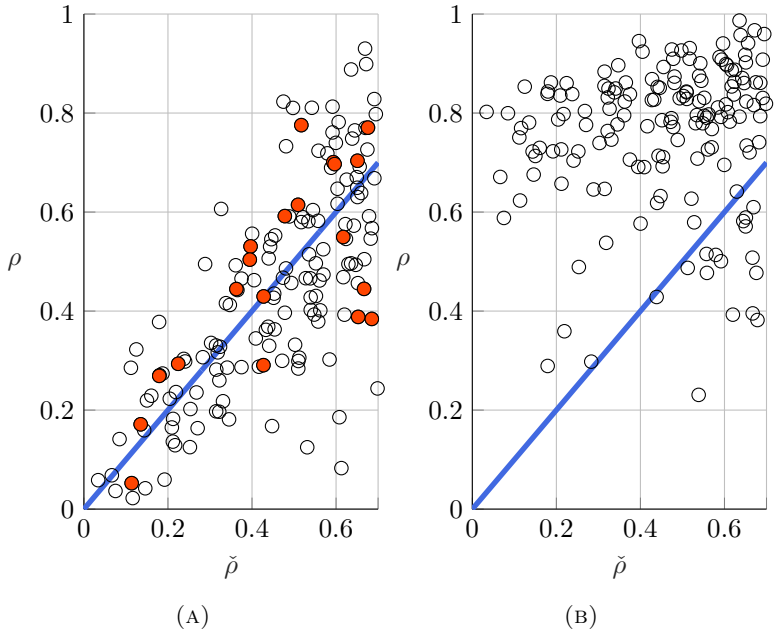

FIGURE 5.4: CFEn regularity index for (a) Case I, simulated vs in vivo and (b) case II, random in vivo vs in vivo. Filled circles in (a) indicate a single randomly chosen channel for each subject.

t-tests (TOST) with the null hypothesis:

$$\mathrm{H}_0 : \mu_{\check{\rho}} - \mu_\rho < -\delta \quad \text{or} \quad \mu_{\check{\rho}} - \mu_\rho > \delta, \tag{5.16}$$

where μ indicates the population mean [180]. The null hypothesis was rejected for case I ($p < 0.001$), showing that the model outputs are as equivalent to the in vivo recordings as a later set of recordings on the same channel.

5.5.3 Incorporating HRF Data in the Model

In order to show the utility of our model in the presence of stimuli, we used a dataset from [181] that is available online at [182]. We refer to this dataset as Experiment 2 (E2). It was obtained from a single participant performing a finger-tapping task. The total recording time was 756s, where the task and rest periods were ∼10s and ∼20s, respectively, with 20 task repetitions. The NiRS device used in the experiment was a Hitachi ETG-4000 with 24 channels and light sources of 695nm and 830nm wavelength operating at a 10Hz sampling frequency. Note that E2 has only been used here for its HRF component and that functional NiRS or HRF are not the key interests for this thesis and rather the AP component is used here to study vascular health. Measured parameter values for E2 are reported in Table 5.1. Note that the reflected wave information could not be extracted due to the low sampling frequency. A sample 695nm-wavelength channel from E2 was selected, which reflects the underlying activation due to the stimulation

(see Fig. 5.5a). To process both the in vivo and synthetic signals we first extracted the haemodynamic responses to the stimuli by applying a bandpass filter at 0.01-0.2Hz and then averaging it with respect to the stimulus onsets (see Fig. 5.5b). Then, an equivalent synthetic haemodynamic response was generated using the E2 HRF values in Table 5.1 and stimuli onset and offset information from the database. The synthetic HRF response was added to ten different synthetic signals generated with values presented under the colum heading E2 in Table 5.1 plus f_2, H_{mean}, σ_{n}^2 and a_{LFC} set to 0.27Hz, 86bpm, 0.059 and 1.42, respectively. Note that E2 dataset is in optical density units and the difference between E1 and E2 a_{AP} causes the differences in power parameters. Now, to extract the haemodynamic response from the synthetic signals, the same filtering and averaging process as used with the in-vivo signal was applied. The extracted HRF is shown in Fig. 5.5b.

5.6 Synthetic Signal and Vascular Health Indices

In this section we aim to calculate different cerebrovascular health indices using synthetic NiRS signals. To this end, we first introduce a new automatic NiRS peak detection algorithm to locate the systolic and reflected peaks in the NiRS signal. This algorithm can then be used to calculate health indices from synthetic and in vivo NiRS signals.

5.6.1 NiRS Peak Detection

Here we propose an algorithm for automatic detection of the forward and reflected NiRS peaks i.e., t_{sys} and t_{refl}, respectively. For a given signal, s, the proposed algorithm uses the second derivative to locate key points in the signal. This is based on similar approaches that have been proposed for locating inflection point in the pressure waveforms [110]. After preprocessing; i.e., averaging, filtering and rotating the signal around the x-axis (to give the reflected-wave peak and systolic peak positive values), the second derivative of s (s_2) is calculated. Next, the following time points are defined on the s and s_2 signals: $\{t_{\text{p1}}, t_{\text{p2}}, ...\}$, the time of the peaks on the s signal and $\{t_{\text{zc1}}, t_{\text{zc2}}, ...\}$ the time of zero-crossings on the s_2 signal. If the number of s_2 zero-crossings is less than 4, the channel is excluded. Otherwise,

$$t_{\text{sys}} = \min\left(t_{\text{p1}}, t_{\text{zc2}}\right). \tag{5.17}$$

Then, to define t_{refl} the algorithm only checks the time period between t_{zc3} and t_{zc4}. If s has a positive peak, t_{refl} is set as the time point corresponding to this peak (t_{pi}). Otherwise, it is set as the time when s_2 reaches its minimum, t_{min} (all within the specified

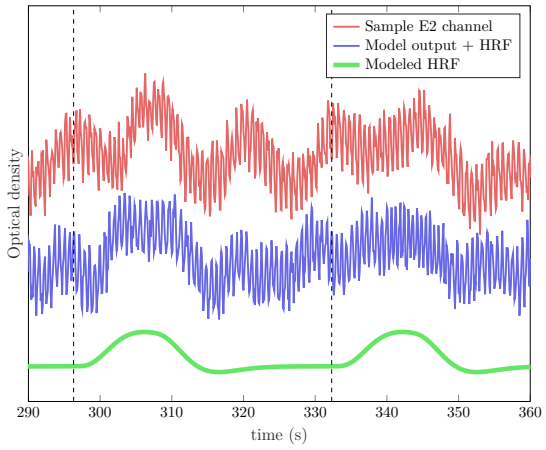

(A)

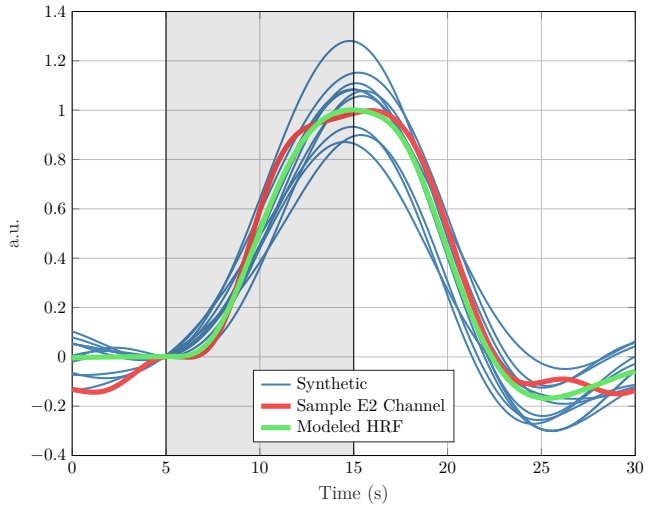

(B)

FIGURE 5.5: In vivo, sample synthetic signal with stimulation and haemodynamic response in red, blue and green, respectively. (a) Time-domain signal with vertical lines showing stimulus onsets and (b) averaged signals with grey area showing the activation period.

time period between t_{zc3} and t_{zc4}). That is:

$$t_{\text{refl}} = \begin{cases} t_{\text{pi}} & \text{if } s \text{ contains a positive peak} \\ t_{\text{min}} & \text{else} \end{cases}. \tag{5.18}$$

Then, we calculate the timing index as:

$$\text{TI}_{\text{NiRS}} = \frac{1}{t_{\text{refl}} - t_{\text{sys}}}. \tag{5.19}$$

Examples of the use of the proposed algorithm are shown in Fig. 5.6. It shows the algorithm applied to in vivo (left column Fig. 5.6) and theoretical summation signals (right

column of Fig. 5.6). Three main types of AP signals, s, are shown in this figure where the detected t_{sys} and t_{refl} values correspond to either a peak point or an inflection point on the recorded signal. The theoretical summation signals are formed by adding three waveforms: 1) an incident forward-travelling waveform 2) a reflected waveform and 3) a re-reflected waveform (which is also travelling towards the periphery). The purpose of the theoretical summation signals is to better visualize where the underlying waveforms reach their peak and how the algorithm performs in terms of detecting the peak times. For each theoretical summation case the underlying waveforms are arranged so that the resulting observed signal (black lines on the right column of Fig. 5.6) resembles an in vivo case (left column of Fig. 5.6).

At this stage, we have developed a mathematical model of the NiRS signal and introduced an algorithm for the automatic detection of the systolic and reflected peaks in an averaged NiRS signal. Now, we aim to examine the effects of system parameters on the accuracy of the peak detection algorithm. Further, we will use the same model to examine the application of AI and PI indices in the context of the NiRS signal.

5.6.2 Effects of Signal Parameters on Reflection Time Measurement Accuracy

Case I

For this case, we generated the simplest form of NiRS signal, in which only T_{refl} values change with age. This case will provide an indication of the performance of the proposed peak detection algorithm and a baseline for comparison with other cases.

Model Inputs: The sampling rate, f_{s}, was set to 100 to obtain smooth results. Parameters f_1, c_1, c_2, σ_1 and σ_2 were set to the default values in Table 5.1. Signal amplitude, a_{ap}, was set to 1 for easier visualization and wherever E1 data is involved in this section it was scaled accordingly to match the signal amplitude used here. All the LF parameters except a_{LFC} were set to default values. An HRF was not considered in this section. Other inputs were set as follows: f_2 (breathing rate) $= 0$, $H_{\text{std}} = 60$, $\sigma_{\text{n}}^2 = 0$, $a_{\text{RW}} = 10\%$ and $r_{\text{SD}} = 0.5$. See Table 5.2 for the list of values used for the input variables. In order to model changes in T_{refl} with age, we used the Formula 3.12 which calculates T_{refl} based on R, C, Z_0, PWV and d_0, which we will refer to as the *secondary inputs*. We set the secondary inputs similarly to Section 3.3.2 (where they were used to simulate the reflection time of the radial blood pressure signal). However, to adjust for secondary input variable changes from the radial artery to smaller cerebral vessels, we multiplied R, C, Z_0, PWV and d_0 by the factors of 8, 0.6, 1.5, 1.2 and 0.5, respectively. These numbers may not accurately describe the arteries that the NiRS technique acquires signals from; however, they result in a similar range of T_{refl} values that of the in vivo NiRS signals (in the next chapter, the in vivo TI_{NiRS} values will be

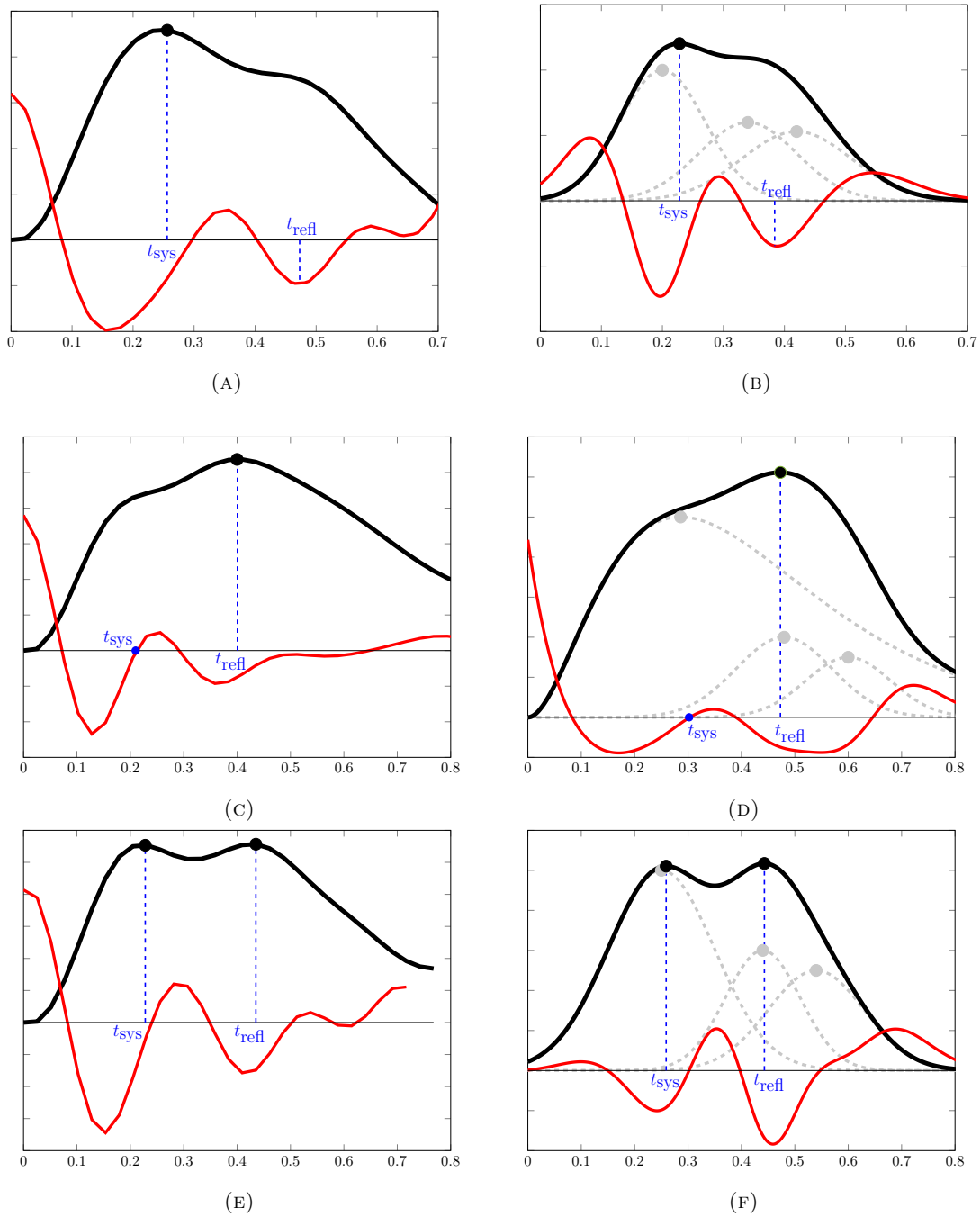

FIGURE 5.6: Three main types of in vivo AP signals (left column) and equivalent simulated signals (right column). Black lines represent observed blood volume signals (s) and the red lines are their second derivatives (s_2). Grey lines represent the underlying forward, reflected and re-reflected waveforms.

discussed in greater detail). Besides, values for the secondary inputs that match the NiRS recordings, which also depend on the measurement location, are not reported in the literature nor is it clear how smaller arteries and arterioles contribute to the NiRS signal. The age values were set to vary from 20 to 80 years, which resulted in T_{refl} values (digitized at 10ms sampling intervals) that ranged from 120-350ms (see Fig. 3.2b for simulated T_{refl} changes for men and women in the radial artery).

Results: Since no randomness was included in this case, two simulations were run for each integer age value one for male and one for female inputs. That is, a total of 122 90-second-long NiRS signals were produced. The signals were averaged using the diastolic points and rotated around the x-axis, then were input to the peak detection algorithm without any bandpass filtering. The T_{refl} values were detected correctly in 92.6% of the waveforms and the mean squared error (MSE) for this case was 6.6(ms)^2 (see Fig. 5.7a).

Case II

This case includes all the input variables except WGN (no bandpass filtering was used in the preprocessing step). The model inputs are the same as those used in case I except that f_2 (breathing rate) was set to a uniformly distributed number between 12 and 20 breaths per minute. The HR was set based on reported resting HR data; see Fig. 5.8 [183]. H_{std} was set to the default value of 5bpm based on Table 5.1 and r_{SD} was set to 0.6. a_{LFC} was selected randomly from E1 for each simulation. See Table 5.2 for the list of values used for the input variables.

Results: 122 random waveforms were generated for different ages and genders. The waveforms were averaged and input to the peak detection algorithm. The accuracy of T_{refl} detection and the T_{refl} MSE were 61.5% and 37.5(ms)^2, respectively (see Fig. 5.7b).

Case III

For this case, WGN was added to the parameters used in case II. After selecting random samples from E1 for each simulation, their a_{LFC} and σ_{n}^2 values were used to generate a synthetic signal. a_{RW} was set to linearly increase from 25% to 40% for the age range of 20 to 80 years.

Results: 225 random waveforms were generated and bandpass filtered at $0.5-6.5$Hz before averaging. A sample synthetic NiRS signal for this case is shown in Fig. 5.9 in different stages of construction and processing. The MSE for this case was 266.4(ms)^2; i.e., a mean $\approx$17ms error, which is less than the sampling interval used in both in-vivo datasets in this chapter. The results for this case are shown in Fig. 5.5.

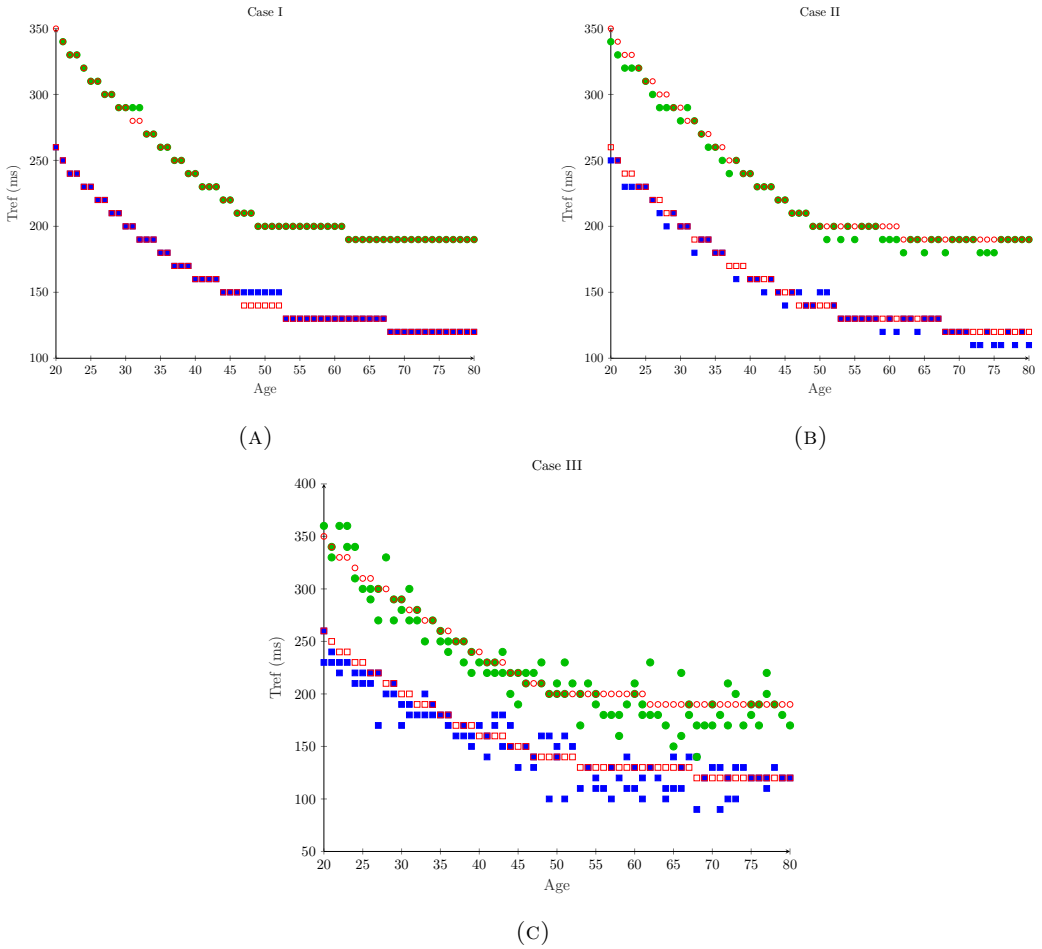

FIGURE 5.7: Simulation results for (a) case I, (b) case II and (c) case III. Green circles and blue squares show simulation outputs for men and women respectively. Red circles and squares show input T_{refl} values for men and women, respectively.

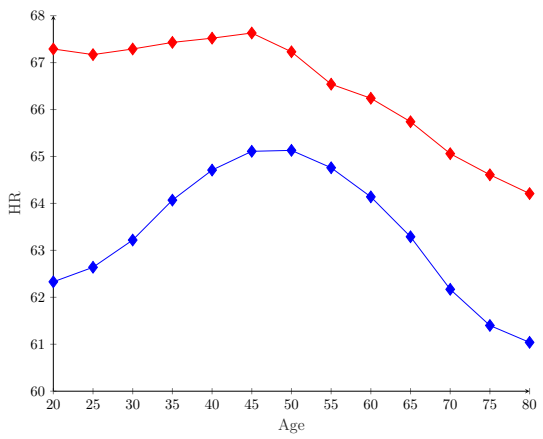

FIGURE 5.8: Resting-state HRs reported in [183] for men and women in blue and red diamonds, respectively. The blue and the red lines show interpolated HR values for men and women, respectively.

TABLE 5.2: Model parameters used in Section 5.6.2

Parameter		Case I	Case II	Case III	Case IV	Case V	Case VI
Device	f_s(Hz)	100	100	100	100	$[25-125]$	100
AP	$f_1(\times 10^{-2}\text{Hz})$	10	10	10	10	10	10
	$f_2(\times 10^{-2}\text{Hz})$	0	$\mathcal{U}[20, 33.3]$	$\mathcal{U}[20, 33.3]$	26.7	26.7	$\mathcal{U}[20, 33.3]$
	c_1 $(\times 10^{-3})$	29	29	29	29	29	29
	$c_2(\times 10^{-3})$	29	29	29	29	29	29
	σ_1(mHz)	29	29	29	29	29	29
	σ_2(mHz)	29	29	29	29	29	29
	a_{AP}	1	1	1	1	1	1
	H_{mean}(bpm)	60	Fig. 5.8	Fig. 5.8	75	75	$\mathcal{U}[60, 100]$
	H_{std}(bpm)	0	5	5	0	0	5
	a_{RW}(%)	10	10	25–40	30	30	25–40
	T_{refl} $(\times 10^{-2}\text{s})$	12–35	12–35	12–35	20	20	12–35
	r_{SD}	0.5	0.6	0.6	0.6	0.6	0.6
WGN	σ_{n}^2	0	0	E1	$[0.02-1]$	0.01	E1 fixed
LF	K	100	100	100	100	100	100
	A	$\mathcal{U}[-1, 1]$	$\mathcal{U}[-1, 1]$	$\mathcal{U}[-1, 1]$	$\mathcal{U}[-1, 1]$	$\mathcal{U}[-1, 1]$	$\mathcal{U}[-1, 1]$
	f_1(Hz)	0.01	0.01	0.01	0.01	0.01	0.01
	f_2(Hz)	0.09	0.09	0.09	0.09	0.09	0.09
	a_{LFC}	0	E1	E1	0.3	0.3	E1 fixed

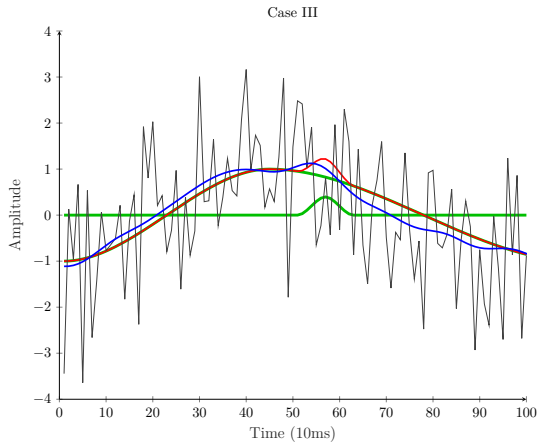

FIGURE 5.9: The first cycle of a 90-second synthetic signal before adding LF components (WGN) is in green. The reflected waves is also shown in green. The red signal is the sum of the two green signals, which is the synthetic NiRS signal before noise was added. The black line is the final synthetic signal before averaging and bandpass filtering, after which it is represented by a blue line.

Case IV

Here, we will examine the accuracy of the peak detection algorithm when changing the noise level. All parameters are set to default except a_{LFC} and σ_{n}^2 (see Table 5.2 for the list of used values). A single set of secondary variables from Case I was used which correspond to a 50-year-old male and result in a fixed T_{refl} value equal to 200ms. Hence, given a fixed T_{refl} value we will change σ_{n}^2 from 0.02 to 1 and observe the performance of the algorithm in detecting systolic and reflected peaks. Note that the range of a_{LFC} and σ_{n}^2 values are different in Table 5.2 and Table 5.1 due to the signal amplitude differences.

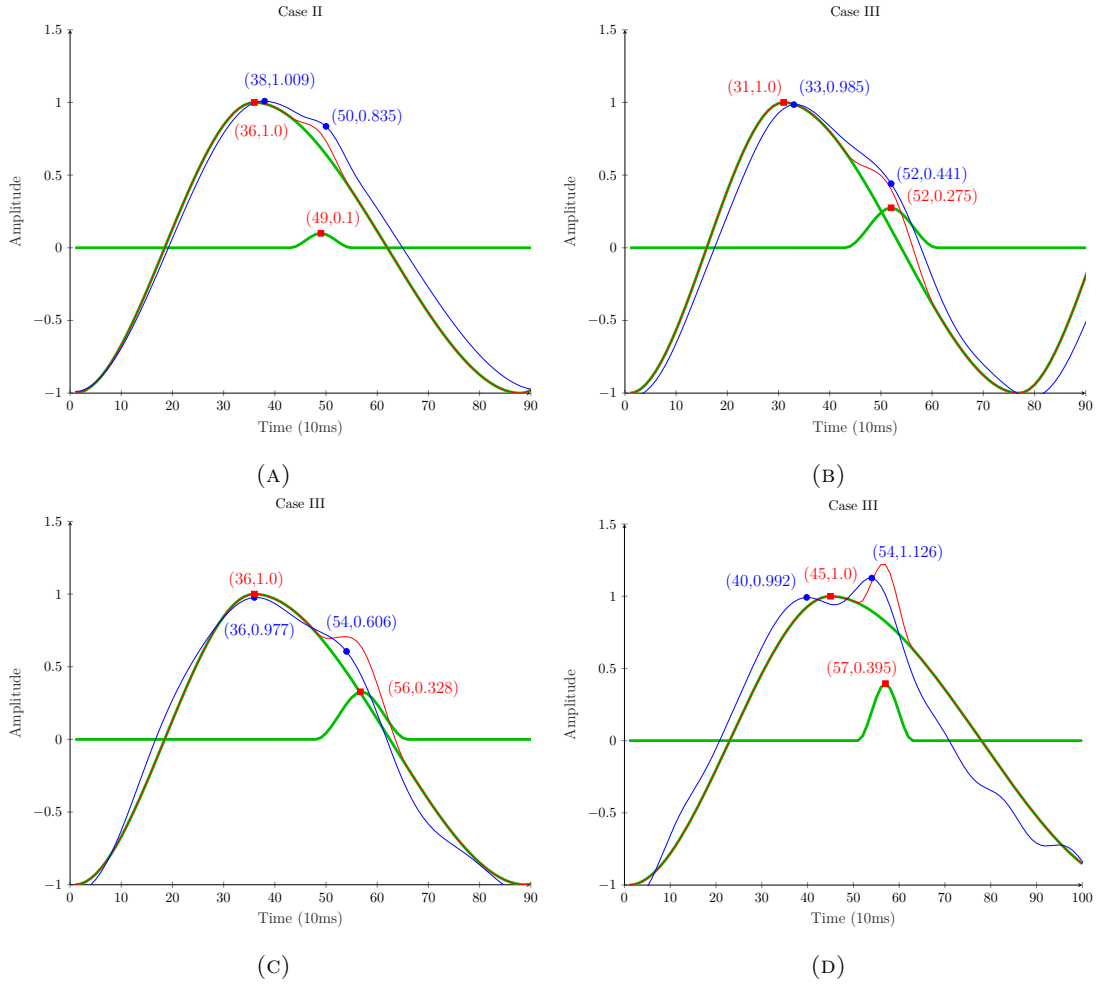

FIGURE 5.10: First cycle of the synthetic signals before adding LF components, WGN, and reflected waves (green lines). The reflected wave is also in green and the first cycle of the clean signal is in red. The signal after adding noise, averaging and bandpass filtering is shown in blue. The input systolic and reflected peak locations are marked with red squared. The blue circles show the detected systolic and reflected peaks. (a) case II, female, age 60 years, input reflection time 130ms, calculated reflection time 120ms. (b) case III, female, age 28 years, input reflection time 210ms, calculated reflection time 190ms. (c) case III, male, age 51 years, input reflection time 200ms, calculated reflection time 180ms. (d) case III, female, age 78 years, input reflection time 120ms, calculated reflection time 140ms.

Results: Five equally-distanced σ_{n}^2 values between 0.02 and 1 were chosen and 30 waveforms were generated for each unique σ_{n}^2 value. This produced a total of 150 randomly-generated waveforms which were then processed as described earlier. The results for this case are calculated as MSE and shown in Fig. 5.11a.

Case V

In this case, we will examine the accuracy of the peak detection algorithm when changing the sampling frequency, f_{s}. The sampling frequency is often an adjustable parameter of the recording device and although low sampling rates will not let us examine the reflected

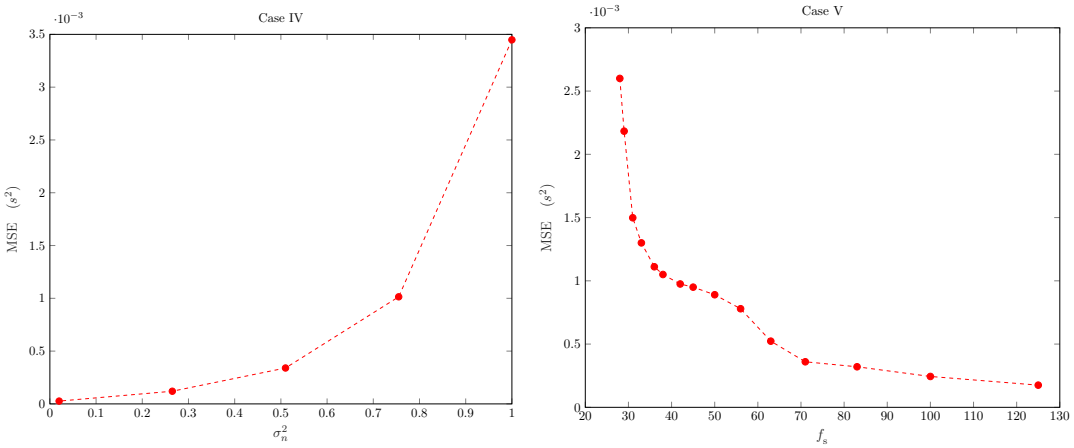

(A) (B)

FIGURE 5.11: Case IV and V simulation results. The performance of the peak detection algorithm is measured with MSE as noise level (Case IV) and sampling frequency (Case V) change.

waves, the high sampling rates will also result in unwanted data points and huge data files. All input parameters except f_s are set similarly to Case IV (see Table 5.2 for the list of used values) which correspond to a fixed T_{refl} value of 200ms. The sampling frequency was changed between 28 and 125Hz. It is common for commercial NiRS devices to operate in sampling frequencies lower than 25 samples per second, however, we were unable to access the performance of the peak detection algorithm for $f_s < 25$Hz because of the limitations in the synthetic signal model. That is because the model uses the frequency band of 6-12Hz for WGN analysis.

Results: Fifty random waveforms with $f_s = 500$ were created and then each down-sampled by factors of 4 to 18 to generate a total of 750 waveforms for analysis. Each waveform was processed as described earlier and fed to the peak detection algorithm. The MSE values were calculated for the results and are shown Fig. 5.11b.

Observations

In the simulation results shown in Fig. 5.7 there is a tendency to underestimate the reflection time. Here, we provide sample signals for each case in which the model underestimates (Figs 5.10a, 5.10b and 5.10c) or overestimates (Fig. 5.10d) the reflection time. These samples are not from the simulation sets reported earlier but they were generated in the same way. The averaged signal systolic peak is dislocated as a result of WGN and HR variability, with H_{std} set to 5bpm for cases II and III (i.e., all the detected systolic peaks matched the individual systolic peaks of the signal in case I). The location of the reflected peak is affected similarly by the WGN and HR variability and also by summation with the incident wave. Generally, the slope of the incident wave when added to the reflected wave makes the final reflected peak appear closer to the

systolic peak. This is the case in Figs 5.10a, 5.10b and 5.10c when the systolic peaks are aligned between the single cycle (red) and averaged signal (blue). Other factors, such as filtering may result in dislocating the peaks, especially in older subjects where the reflected peak is closer to the systolic peak and is larger in amplitude and filtering softens the waveform (see Fig. 5.10d).

As expected, the results for Case IV (shown in Fig. 5.11a) confirm that increased noise level reduces the accuracy of the proposed peak detection algorithm in locating systolic and reflected peaks. Case V results, as shown in Fig. 5.11b, indicate that increased sampling frequency reduces the peak detection error. This is explained by more intense detail recording in higher sampling frequencies.

5.6.3 Effect of Changes in HR and Age on Calculated TI and AI Indices

This section discusses TI and AI changes with age and HR in a simulated dataset.

Case VI

For this case the input variables are similar to that of case III, except that only a single random value was selected for a_{LFC} and a single value of σ_{n}^2 was used for all the simulated signals. The HR was selected randomly between 60 and 100bpm (a uniform distribution was used), which is the clinical range for normal resting HR [184]. Setting random fixed values for a_{LFC} and σ_{n}^2 helped us better visualize the age-related and HR-related changes in TI and AI. After using the peak detection algorithm, TI was calculated using Equation (5.6.1) and the near-infrared spectroscopy augmentation index ($\mathrm{AI}_{\mathrm{NiRS}}$) was calculated in a similar way to Equation (3.13); i.e.,

$$\mathrm{AI} = \frac{s(t_{\mathrm{refl}}) - s(t_{\mathrm{dia}})}{s(t_{\mathrm{sys}}) - s(t_{\mathrm{dia}})}, \tag{5.20}$$

where t_{sys} and t_{refl} are as defined in Section 5.6.1 and t_{dia} is the end-diastolic point on the averaged and rotated NiRS signal; i.e., the AP signal.

Results: The results for 400 randomly-generated signals are shown in Fig. 5.12. The results confirm the validity of Equations (3.12) and (3.19), which were the main contribution of Chapter 3. They match the results from the literature, as discussed in detail in Section 3.5. As shown in Fig. 5.12, AI is negatively correlated with HR (similar results were reported in [137]) and positively with age (see Table 2.2 for related literature). Furthermore, from Fig. 5.12b, we notice that the curve describing the relationship between AI and age becomes less steep at ages above 55 years. Similar trends have been reported in the literature [2, 111, 123]. On the contrary, TI does not show a noticeable change with HR, which was proven mathematically in Chapter 3 (see (3.12) and see

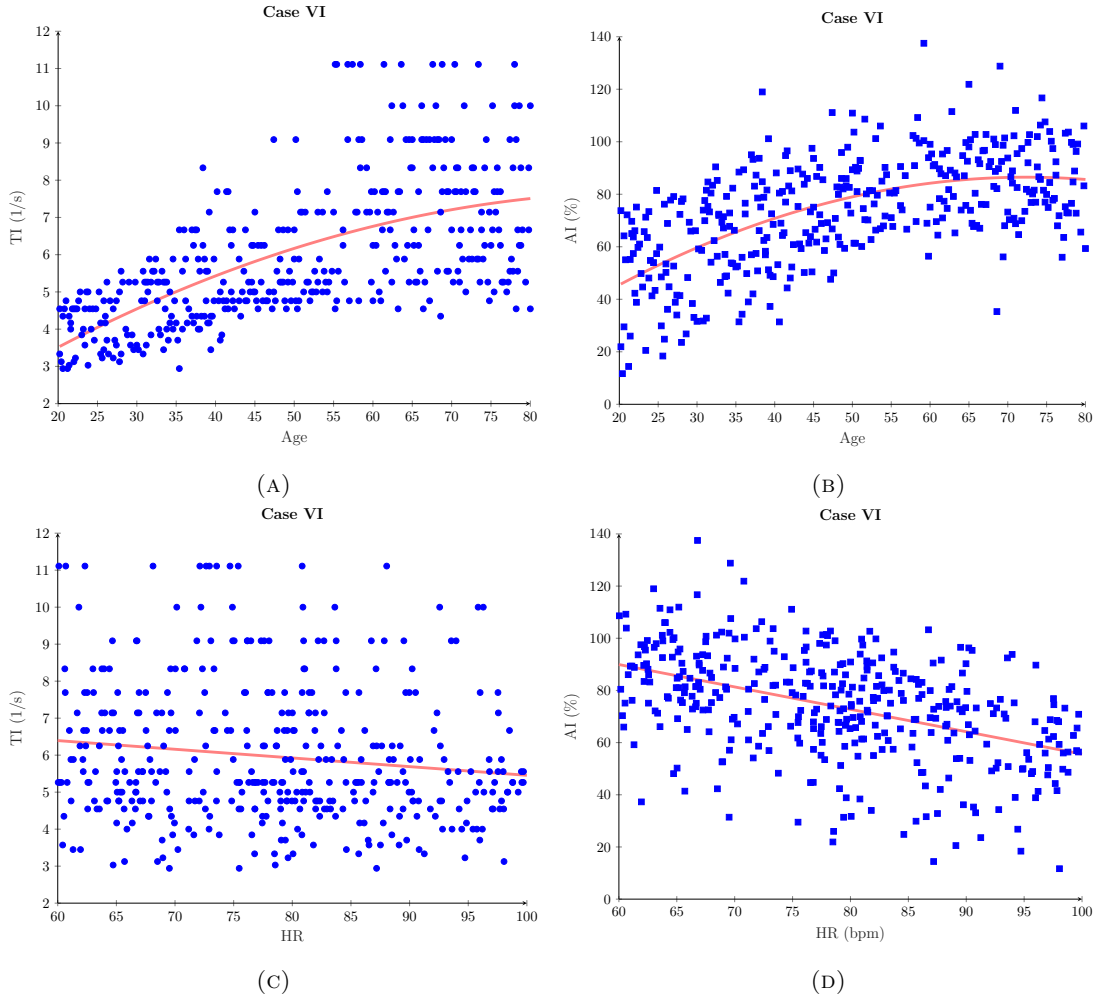

FIGURE 5.12: Case VI simulation results. Red lines show least-squares second-order and first-order polynomials fitted to the age and HR data, respectively.

[107] for similar published results). The TI shows a similar flattening curve as AI (see Fig. 5.12a), which has also been reported in the literature [46, 106, 115].

5.6.4 Measuring PI in a NiRS Signal

We defined PIs for TCD and MRI signals in Equations (2.23) and (2.27), respectively. Here, we want to evaluate the possibility of calculating a pulsatility index for NiRS signals. In an unprocessed NiRS signal the mean value does not correspond to blood volume changes unlike TCD and MRI where the mean value shows the mean blood flow velocity and mean blood flow, respectively. As discussed in Section 5.3.3, VLF components and Mayer waves at 0.1Hz and lower frequencies influence the NiRS signal independently of the mean blood volume value. This means that in an unfiltered signal, the NiRS signal's mean value varies considerably, making the the peak-to-mean ratio also change considerably. Filtering the NiRS signal, which is a common processing step and removes the LF components, sets the signal mean to zero and again the peak to mean

ratio becomes meaningless. Therefore, the pulsatility index in its current definition can not be applied to a NiRS signal to acquire meaningful information.

5.7 Discussion

Assumptions were made to build our simplified NiRS signal model. The key assumptions made in this chapter were as follows.

- The frequency drifts of the AP signal had the same characteristics as the ECG-RR interval signal. This assumption holds based on 1) the nature of the AP signal discussed in Section 5.3.1 and 2) the analysis done by [10, 86] which considered simultaneous ECG and NiRS measurements.

- The effects of Mayer and respiratory amplitude changes on the signal amplitude can be modelled by a Gaussian function in the frequency domain. This assumption is based on the inherent natural behaviour of the physiological phenomena. A similar assumption is made in [157] in modelling the frequency drifts of components of the same signal.

- Mayer, respiratory and VLF waves can be combined into a single component (i.e, the LF component) and described with a single amplitude parameter, a_{LFC}. Our data analysis shows that a good level of accuracy can be achieved with this method. However, simultaneous ECG, respiration and NiRS monitoring can help to better understand these components and, possibly, to separate them.

- We assumed that the frequency drifts and amplitude changes caused by the Mayer and respiratory waves are not synchronized. Therefore, different realizations of θ in Equation (5.3) were used for each component. This assumption was made as the nature of these components has not yet been explored in terms of NiRS signals.

In Section 5.6, we introduced a new NiRS peak detection algorithm which was then applied to synthetic signals for the calculation of $\mathrm{T_{refl}}$, TI and AI. The model is able to simulate TI and AI changes with age and HR that match in vivo results reported in the literature. Nonetheless, the simulations were limited by the knowledge of the secondary inputs; i.e., R, C, Z_0, PWV and d_0. These inputs were set based on the information provided in Chapter 3; however, they were multiplied by certain values to adjust for changes that the NiRS signal may have. The secondary inputs were used to calculate reflection times which had the same trend as shown in Fig. 3.2 for the radial artery.

5.8 Conclusion

In this chapter, we proposed a NiRS signal model. The model includes LF elements, AP, reflected waves, Mayer and respiration waves. Appropriate default values based on recorded NiRS data analysis and the literature were proposed. A new NiRS peak detection algorithm was introduced and synthetic NiRS signals were generated by the model resembling a wide age change in the data. Using the proposed peak detection algorithm reasonable accuracy was demonstrated in calculating reflection times using the NiRS signal. Further, the calculated TI and AI values showed similar correlations with age and HR as have been reported in the literature. These promising results obtained using synthetic signals motivated us to apply the timing index to NiRS measurement in a clinical study.

Chapter 6

Indexing Cerebrovascular Health Using NiRS

6.1 Introduction

In this chapter, we use the transmission line (TL) model of Chapter 3 and the TI_{TCD} index proposed in Chapter 4 along with our understanding of the NiRS signal discussed in Chapter 5 to propose a new timing index for NiRS. The new index is then calculated in a sample of 38 participants and compared with the existing PReFx index in terms of correlations with age, CRF, AI_{TCD} and PI_{MRI}.

Cerebrovascular compliance is commonly assessed non-invasively using indices derived from blood pressure and flow readings. TCD ultrasound and MRI are the modalities most widely used to acquire cerebrovascular compliance and cerebrovascular health indices. While it is possible to estimate compliance using TCD blood flow velocity [73], the method relies on estimates of vascular cross-sectional area, arterial inflow and venous outflow, which are not readily measurable. The TCD indices, such as PI_{TCD} and AI_{TCD}, are the preferred TCD cerebrovascular health indicators [53, 54, 145]. Of these two, PI_{TCD} is the most commonly used TCD index due to its ease of calculation. However, AI_{TCD} has been shown to have a stronger correlation with cerebrovascular health indicators such as age and CRF [185]. PI_{MRI} is the commonly adopted MRI-based cerebrovascular health measure [74]. While PI_{MRI} has a high spatial resolution for localized measurements, MRI is less commonly used as it is both costly and time-consuming, making it unsuitable for simple and routine monitoring of vascular health in the general population.

NiRS is a relatively new technology that measures regional blood volume changes based on absorption of NiR light, mainly by oxygenated blood inside cerebral arteries [10, 11]. NiRS offers high temporal resolution and is sufficiently sensitive to detect changes in blood volume during the cardiac cycle. Therefore, NiRS allows local studies

of cerebrovascular behaviour and possible assessment of cerebrovascular health [10]. The recently proposed PReFx is the first NiRS-based approach to the indexing of cerebrovascular compliance [10]. PReFx measures the deformation of the blood volume waveform during the systolic relaxation phase due to the presence of reflected waves. It has been demonstrated to correlate with CRF and inversely correlate with age [10, 86, 91]. PReFx is an area measurement in the averaged NiRS signal. The PReFx algorithm assumes that the first positive peak after the diastolic minimum is the systolic peak, which may not be the case when the systole reaches its maximum in an inflection point rather than a peak. Therefore, we are motivated to use an index that can be easily applied to NiRS signals. In Chapters 3 and 4, we showed that the TI is a strong predictor of vascular health based on both blood pressure and blood flow velocity measurements and reported significant correlations between TI and vascular health factors such as age and CRF. In Chapter 3 we showed that based on a tube-based model of the arterial tree, the TI is directly controlled by the vascular ageing factors including compliance, resistance and PWV [154]. As such, we propose a new near-infrared spectroscopy timing index (TI_{NiRS}) to directly measure the timing of reflected waves. Here, we define the TI_{NiRS} as the inverse of the time interval between the systolic and reflected waveform peaks in the NiRS signal.

6.2 Methods

6.2.1 Protocol and Data Collection

Thirty eight adults (23 female, 15 male, age range = 24-67 years, mean age = 41.7 years) were recruited from the Newcastle, Australia. They provided informed consent prior to assessment. The study protocol was approved by the University of Newcastle Human Research Ethics Committee and is registered in the Australian and New Zealand Clinical Trials Registry (ACTRN12619000144112). Each participant attended the Hunter Medical Research Institute and the University of Newcastle Callaghan campus over two consecutive days and participated in three scanning sessions. Participants were asked to refrain from consuming caffeine before their scans. Height, weight, age, sex and resting HR were recorded for each participant and a physical activity questionnaire was completed.

TCD ultrasound (DopplerBox X; Compumedics DWL, Singen, Germany) was used to record resting-state cerebral blood flow velocity from the right and left MCAs. Participants were also scanned on a 3T MRI scanner (Magnetom Prisma, Siemens Healthineers, Erlangen, Germany) equipped with 64-channel receive only head coil, while a standard built-in dual channel body coil was used for RF transmission. Blood flow was quantified using a phase contrast flow quantification sequence (TR = 26.5ms, TE = 6.9ms, slice

thickness = 5mm, matrix 256 × 256) of a single excitation with a velocity encoding value of 120cm s^{-1} on the MCAs [147]. Finally, participants were instructed to relax and sit still for 300 seconds of resting-state NiRS recording. A frequency-domain NiRS (ISS ImagentTM, Champaign, Illinois, USA) was used at a 110MHz modulation frequency and sampling rate of 39.0625Hz. The set-up montage covered the frontal lope and consisted of four detectors each crossed with 16 time-multiplexed sources (eight of which operated at 690nm and the other eight at 830nm), making a total of 64 channels. Participants were asked to wear an Equivital EQ02 LifeMonitor sensor belt during this session, which recorded ECG and NiRS signals simultaneously.

During the TCD imaging session, resting-state HR was measured using an HR monitor device (Omron HEM-7320). Participants assumed a sitting position for approximately five minutes during headpiece set-up before recording commenced. During TCD recording, the HR was measured once per minute for three minutes. The mean of these three HR measurements was used as the resting-state HR.

6.2.2 Calculating The Indices

6.2.2.1 $\mathbf{PI_{MRI}}$

MRI phase contrast (PC) images were processed using the scanner software (Siemens Syngo) by manually placing a region of interest around the image of the MCA and quantifying the flow. The PI_{MRI} was then obtained by subtracting the minimum flow from the maximum flow and dividing it by the mean flow over the cardiac cycle [74], i.e.,

$$PI_{MRI} = \frac{Q_{max} - Q_{min}}{\overline{Q}}, \tag{6.1}$$

where Q indicates the flow and the bar sign indicates the mean value, as previously mentioned in Equation (2.27). Three subjects did not have an MRI scan and among the remaining subjects, PI_{MRI} was calculated either for both MCAs ($n = 21$) or for just a single MCA ($n = 14$) based on data quality. The indices from right and left MCAs were then averaged for each subject.

6.2.2.2 $\mathbf{AI_{TCD}}$

Calculation of AI_{TCD} requires identification of three characteristic points on an averaged Doppler waveform. Peak systole (V_{sys}) peak diastole (V_{dia}) and the peak of the reflected wave (V_{refl}) are the parameters required to calculate the augmentation index [53]:

$$AI_{TCD} = \frac{V_{refl} - V_{dia}}{V_{sys} - V_{dia}}. \tag{6.2}$$

Thus, the timing of the diastolic peaks was first determined automatically in Matlab® using a peak detector function. Then, each signal was averaged with respect to its diastolic peaks, resulting in an averaged signal covering the duration of a single cardiac cycle. The systolic and reflected peaks were set manually on the averaged signal. The TCD data for two subjects were excluded from analysis due to noise. $\mathrm{AI}_{\mathrm{TCD}}$ was calculated using data from both MCAs (and averaged) for 34 subjects and from a single MCA two subjects, depending on data quality.

6.2.2.3 Evaluating CRF

CRF was determined using the non-exercise test model proposed in [151]. It involves a self-reported physical activity score, age, sex, body mass index and resting HR. See Table 4.1 and Equation (4.4) for the physical activity questionnaire and CRF formula, respectively.

6.2.2.4 NiRS Indices

Two different indices were derived from the NiRS recordings: the pulse relaxation function (PReFx) and the proposed near-infrared spectroscopy timing index ($\mathrm{TI}_{\mathrm{NiRS}}$). The pre-processing of the recordings was done similarly for both methods and was adopted from [10] using the "*p_pod*" function [186] which is a Matlab-based software module developed by the same group. Specifically, channels with source detector distances of 2-6cm were selected and went through a quality-control process passing 1283 channels out of the original $38 \times 64 = 2432$ channels. These channels were then normalized by dividing by their mean values and then bandpass filtered to 0.5-5.0Hz. The resulting signal was averaged with respect to the ECG R peaks and then rotated around the x-axis (see Fig. 6.1). The result is called the AP signal, s. The rotation was performed so that the systolic peak would appear as a positive peak and the shape of the signal would look similar to that of a blood pressure, flow or volume signal. This facilitates understanding of the waveform. The arterial pulsation signals were visually inspected and channels that did not have a pulse shape were removed (i.e., low blood volume at the beginning and end representing diastole, and an increase in-between representing systole). Some 964 channels passed the pre-processing stage for further analysis.

PReFx: The pulse relaxation function is calculated based on the methods explained in [10]. In brief, s_{D1} and s_{D2} peaks are found as minima in the s signal in the first and the second cardiac cycles and s_{S} is found as the first local maximum after s_{D1} (see Fig. 6.2). $\{s_{\mathrm{D1}}, s_{\mathrm{D2}}\}$ and s_{S} are intended to represent the diastolic and systolic peaks, respectively. However, s_{S} is not necessarily a systolic peak; see Fig.6.2b where s_{S} is the reflected peak and the systolic peak indicated by an arrow. Then, the area enclosed by

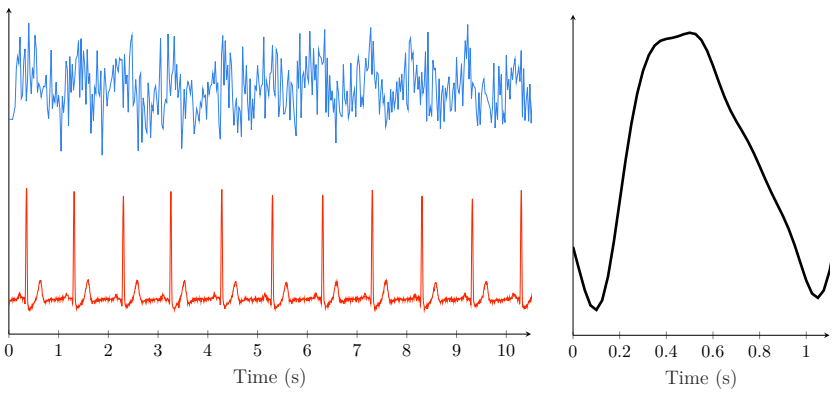

(A) (B)

FIGURE 6.1: (a) Ten-second long raw NiRS signal (blue) and simultaneously recorded signal from ECG lead I (red). (b) Averaged and flipped NiRS s signal.

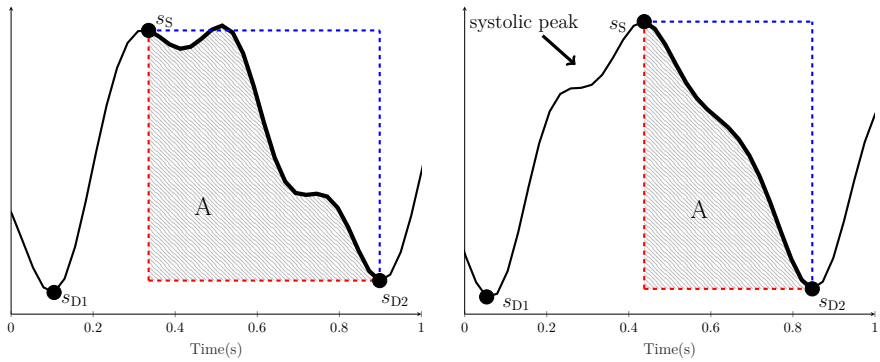

(A) (B)

FIGURE 6.2: Examples of calculating PReFx for two different s signals. The signal s is shown in black, the s_S, s_{D1} and s_{D2} peaks are marked with black circles, and the blue and red rectangles are formed with s_S and s_{D2} at their diagonals. The shaded area, A, is the area enclosed by s between s_S and s_{D2} and the red sides of the rectangle. The calculated PReFx values for (a) and (b) are 0.136 and 0.081, respectively.

the s signal between s_S and s_{D2} is calculated as A and inserted into:

$$\text{PReFx} = \frac{A}{B} - 0.5. \tag{6.3}$$

Where B is the area of a rectangle formed by s_S and s_{D2} at its diagonal ends (i.e. the rectangle formed by blue and red lines in Fig. 6.2). Note that if the drop in volume between peaks was linear, PReFx would equal zero. After communicating with the authors of [10], channels with PReFx value outside the interval of $[-0.1, 0.4]$ were removed and other channels were manually excluded from the calculations where reflected peaks were selected by the algorithm (see Fig. 6.2b for an example). A total of 245 additional channels were removed in this process. Finally, for each subject with more than ten PReFx values, an averaged PReFx value was calculated as the index of vascular compliance. We were able to calculate PReFx for 29 of the 38 subjects.

$\mathbf{TI_{NiRS}}$: We defined the timing index as the inverse of the time between the forward and reflected waveform peaks. In order to find the timing of these peaks, named t_{sys} and t_{refl} for peak systole and peak reflection, respectively, for a given signal, s, we used the automated algorithm introduced in Chapter 5. The algorithm uses the second derivative, s_2, to locate key points in the signal and was described in detail in Section 5.6.1. After all channels were processed for a subject, channels with t_{sys} and t_{refl} outside their mean ± 1.5 std or outside a predefined threshold were excluded from further calculations. The predefined threshold for t_{sys} was any value <125ms and for t_{refl}, it was any value >500ms. Then, if ten or more channels remained, the mean t_{sys} and t_{refl} values for that participant were used to calculate the timing index as:

$$\text{TI}_{\text{NiRS}} = \frac{1}{t_{\text{refl}} - t_{\text{sys}}}. \tag{6.4}$$

Of the original 38 subjects, we were able to calculate a TI for 32 of them.

6.2.3 Statistical Analysis

Statistical analysis was carried out in Matlab® using the inbuilt *corr* function. Lilliefors test of normality with a 5% significance level was used to assess the data distribution. Age and PI_{MRI} were found to be non-normally distributed ($p = 0.0072$ and 0.0020, respectively). All the other distributions were normal. Pearson or Spearman correlation coefficients were calculated for normally-distributed and non-normally-distributed data, respectively. False discovery rate correction was used to adjust significance levels with an initial $\alpha = 0.05$.

6.3 Results

The correlations of the proposed NiRS timing index and existing NiRS PReFx index with the indices derived from other imaging modalities, age and CRF are reported in Table 6.1. Corresponding scatter-plots are shown in Fig. 6.3. Least-squares linear models have not been provided for cases with small slopes. Significant correlations after correcting for multiple comparisons are marked with an asterisk. Note that PReFx is an index of vascular compliance whereas TI_{NiRS} is an index of vascular stiffness that is inversely proportional to compliance. Therefore, the two indices show opposite signs when correlated with the same factors. The proposed systolic peak and reflected wave peak detection algorithm for TI_{NiRS} detected 228 channels (out of 964 input channels) with a systolic peak corresponding to an inflection point (mean participant age for these channels is 42.5 years).

TABLE 6.1: Correlation matrix with correlation coefficients (p-values) [95% confidence interval]. Asterisks indicate statistically significant correlations after correction for multiple comparisons using a false discovery rate

	CRF	Age	AI_{TCD}	PI_{MRI}
TI_{NiRS}	-0.44* (0.011) [$-0.70, -0.10$]	0.53* (0.002) [$0.23, 0.74$]	0.46* (0.010) [$0.12, 0.68$]	0.45* (0.012) [$0.09, 0.70$]
PReFx	0.24 (0.2032) [$-0.16, 0.52$]	-0.40 (0.0295) [$-0.70, 0.06$]	-0.26 (0.1729) [$-0.61, 0.13$]	-0.01 (0.9783) [$-0.41, 0.43$]

TABLE 6.2: AI_{TCD} correlation matrix. p-values are not reported

	CRF	Age	AI_{TCD}	PI_{MRI}
AI_{NiRS}	-0.21	0.19	0.11	-0.27

6.4 Results for Other NiRS Indices

Although the intention of this chapter was to propose a NiRS timing index, for completeness, we present the results of the NiRS augmentation index. Using the systolic and reflected peaks detected by the proposed peak detection algorithm, AI_{NiRS} was calculated as per Equation (5.20). The correlations of AI_{NiRS} with other vascular health indicators are shown in Table 6.2 without statistical tests. Based on the discussion in Section 4.1, AI has some limitations as it correlates with several biological factors not directly related to vessel properties including sex, heart rate, food intake, hydration status, height, weight and body composition [2]. The correlation of AI_{NiRS} with HR was studied in Section 5.6.3 using synthetic NiRS signals. These limitations combined with the higher noise power present in NiRS signals compared to TCD and MRI ones, explain the low correlations in Table 6.2.

Note that the PI currently defined as the peak-to-peak value divided by the mean value (e.g., (2.27)), will not produce interpretable results for the NiRS signals as discussed in Section 5.6.4.

6.5 Discussion

The NiRS indices are designed to measure vascular stiffness which is well correlated with age [15] and CRF [1]. Thus, a common approach with any vascular index is to compare its relationship with age and CRF [10, 187] and here we have investigated the same. The PReFx correlation coefficient reported here for age is consistent with existing studies; however, the correlation with CRF is lower than previously reported. PReFx correlations

with age and CRF in the adult population have so far been studied by the same research group using two different datasets [10, 86]. Reported correlations with age are $r = -0.39$ (mean age = 69.87 years) [10] and $r = -0.43$ (mean age = 47.8 years) [86]; a correlation of $r = -0.60$, mean age = 58.8 years was reported in [91] for a combination of the two datasets. Our reported correlation, $r = -0.40$ ($p = 0.030$), although consistent with the previous values, is not significant. Reported correlations with CRF are $r = 0.416$ [10] and $r = 0.32$ [86], however, our correlation with CRF of $r = 0.24$ ($p = 0.203$) was not significant. Given that the mean age for our sample is 41.7 years, we suspect that the PReFx measure has a lower correlation in younger subjects than older ones. In addition, based on the performance of the PReFx algorithm on the current data, we have identified two potential sources that can distort the PReFx calculation and potentially cause lower correlations. Firstly, there are cases where the PReFx algorithm detects reflected peaks instead of systolic peaks as the s_{S} points. The PReFx algorithm assumes the first local maximum after the minimum peak, i.e. s_{S}, to be the systolic peak, which is not accurate when the true systolic peak is in the form of an inflection point (e.g., see Figs 6.2b and 5.6b). Based on our analysis these cases account for almost one-fourth of all channels (228 of the 964 studied channels) and are more likely to occur in older participants in which the reflected wave moves faster and reaches the incident wave sooner than in younger participants. The second problem occurs in channels with a notch in the signal after the systolic and reflected peaks, which is most likely caused by closure of the aortic valve (similar to the dicrotic notch seen in the pressure waveform [188]). This notch can appear as a large deformation in the signal (see Fig. 6.2a for an example), which will change PReFx values independently of vascular health factors. Among the aforementioned two potential causes of low correlation for PReFx, the first was eliminated in the results reported in Table 6.1 by discarding channels where s_{S} was assigned to the reflected peak. However, if all the channels are included in the calculations, it will remove the significant correlation of PReFx with age i.e., $r = -0.19$.

While no previous NiRS studies have reported a timing index, the correlations of $\mathrm{TI}_{\mathrm{NiRS}}$ with age and CRF match those of the TCD and pressure waves in Chapters 3 and 4 [154, 185]. The proposed $\mathrm{TI}_{\mathrm{NiRS}}$ shows significant correlations with age ($r = 0.53$, $p = 0.002$) and CRF ($r = -0.44$, $p = 0.011$), while the correlations of $\mathrm{TI}_{\mathrm{TCD}}$ with age and CRF are $r = 0.70$ and $r = -0.79$, respectively [185].

Based on a previously proven association between $\mathrm{PI}_{\mathrm{MRI}}$ and SVD [74], we expect NiRS indices to correlate with $\mathrm{PI}_{\mathrm{MRI}}$ (which is an indicator of vascular health). PReFx showed no significant correlation with $\mathrm{PI}_{\mathrm{MRI}}$ ($r = -0.01$, $p = 0.978$), whereas $\mathrm{TI}_{\mathrm{NiRS}}$ correlated significantly with $\mathrm{PI}_{\mathrm{MRI}}$ ($r = 0.45$, $p = 0.012$). $\mathrm{PI}_{\mathrm{MRI}}$ indicates vascular health by measuring the pulsatility of the blood flow. High pulsatility means that fast-travelling reflected waves join incident waves and contribute to increased maximum flow peaks. Similarly, $\mathrm{TI}_{\mathrm{NiRS}}$ reaches greater values when the reflected wave peak is closer

to the systolic peak and pulsatility is high. PReFx also changes based on the location of the reflected wave, high PReFx values correspond to channels with high deformation from a perfect sinusoidal waveform; i.e., the existence of a reflected peak. However, the presence of a dicrotic notch may also affect the PReFx index by distorting the wave shape while having no effect on PI or TI. Thus, in channels with a prominent dicrotic notch, the PReFx may be high while pulsatility is low, which may explain the lower correlation for PReFx.

$\mathrm{TI_{NiRS}}$ showed a significant correlation with $\mathrm{AI_{TCD}}$ ($r = 0.46$, $p = 0.010$), while the correlation of PReFx with$\mathrm{AI_{TCD}}$ was not significant ($r = -0.26$, $p = 0.173$). The augmentation index is a widely accepted index used in both blood pressure and flow velocity (TCD) signals, and is a strong predictor of vascular ageing and stiffening [53, 71, 121, 145]. The AI captures the augmentation of the incident wave by the reflected wave, with smaller values reflecting no augmentation when the arteries are healthy and the propagation speed is low. TI indexes this delay between the incident and reflected waves directly, which is why $\mathrm{AI_{TCD}}$ and $\mathrm{TI_{NiRS}}$ are significantly correlated. The PReFx also correlates with AI as larger PReFx values can correspond to late reflected waves leaving a peak on the systolic-to-diastolic segment of the AP signal and thus increasing the area under the curve. Nevertheless, the correlation may be weakened when the presence of a dicrotic notch increases PReFx regardless of the reflected wave.

Overall, NiRS blood volume waveforms are believed to closely resemble changes in blood pressure [10], which is also supported by the use of NiR light in photoplethysmography and its morphological similarity to the arterial blood pressure waveform [11, 189]. Thus, we believe that the proposed NiRS timing index is affected similarly by vascular health parameters in the same way as the timing index derived from the blood pressure waveforms [154]. As blood pressure can not be readily measured in cerebral vessels, a NiRS-based timing index can provide an alternative approach.

6.6 Conclusion

In this chapter we presented a novel NiRS based cerebrovascular stiffness index, $\mathrm{TI_{NiRS}}$. The $\mathrm{TI_{NiRS}}$ correlates significantly with age, CRF and other cerebrovascular health indices derived from TCD and MRI data, indicating it has high performance in tracking changes in the cerebrovascular system. The $\mathrm{TI_{NiRS}}$ offers a potentially valuable means of indexing vascular health and has superior cost, portability and widespread implementation potential compared with existing techniques.

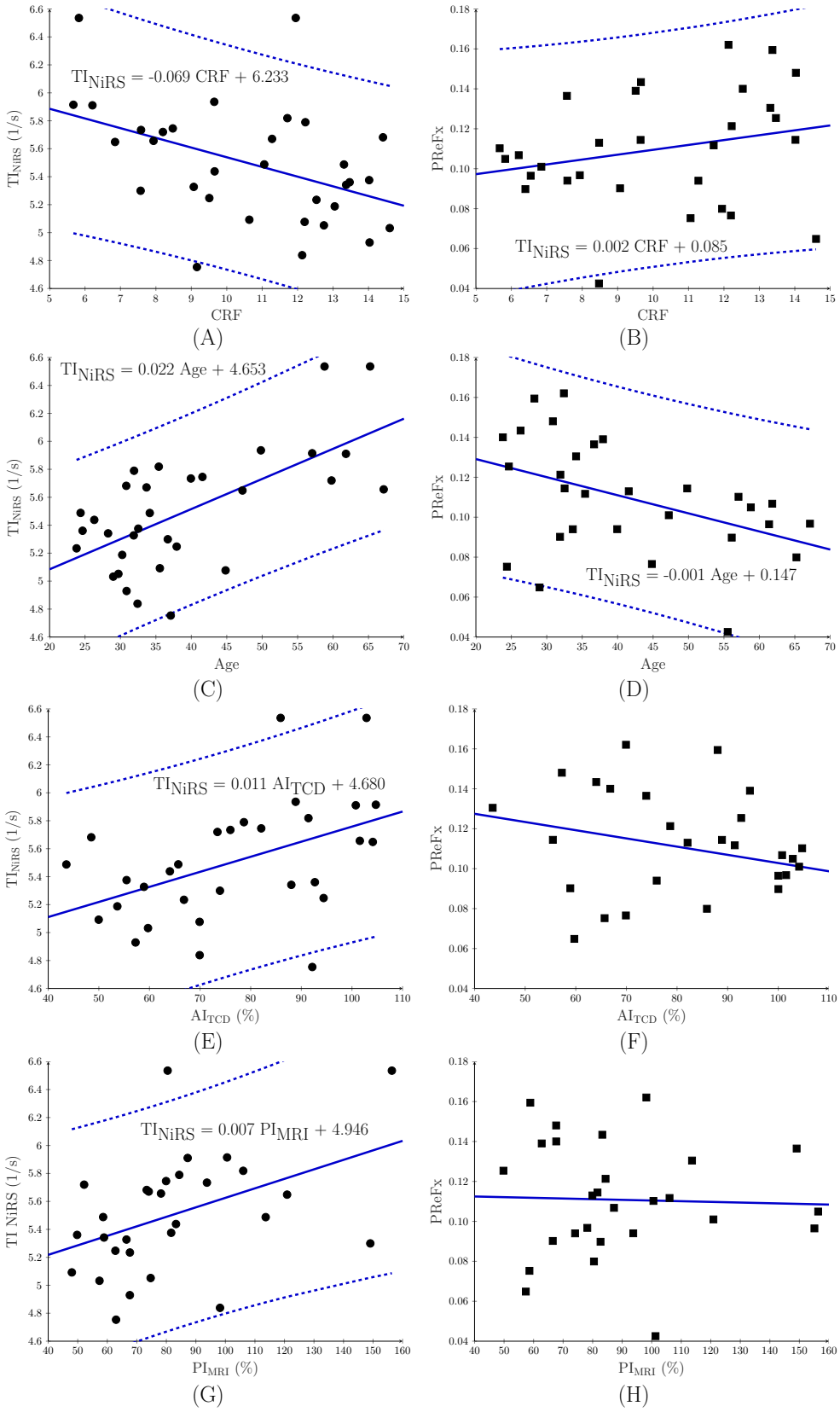

FIGURE 6.3: Scatter-plots of the correlations with least-squares models fitted. Solid blue lines show the linear fit and the dashed lines show the 95% confidence interval. Line equations and confidence intervals have been provided when the correlation is significant.

Chapter 7

Conclusions and Future Work

7.1 Summary of the Main Chapters

This thesis investigated the non-invasive measurement of cerebrovascular health. Chapter 1 outlined current barriers to effectively assessing cerebrovascular compliance.

Chapter 2 outlined the biology of vascular health and the medical implications of vascular stiffening (loss of compliance). A background to mathematical modelling of the vascular system and blood haemodynamics were presented. The various non-invasive measurements used to survey vascular health were outlined, being pressure, flow velocity (using TCD) and flow (using MRI).

In Chapter 3, we considered pressure waves and proposed mathematical models of the wave reflection time (T_{refl}) and AI. The models are based on both TL and WK equivalents of the arterial system and help to interpret commonly observed trends in T_{refl} and AI, such as the flattening with age and changes in AI according to HR. In particular, the model gives us insight into the phenomenon known as the "distal movement of the reflected site". In this chapter we showed that the wave reflection is more than a round trip and that the capacitive and resistive properties of vessels beyond the reflection site can cause a considerable delay in the arrival of reflected waves, which is often interpreted as an apparent distal movement of the reflection site. The chapter particularly focused on pressure waveforms, and the proposed model was evaluated using carotid and radial T_{refl} and AI values reported in the literature.

The results of Chapter 3 motivated the use of a timing based index of vascular stiffness for cerebral vessels in which pressure waves cannot be measured directly. In Chapter 4, a new TCD-based cerebrovascular health index, TI_{TCD}, was proposed. TI_{TCD} is the inverse of T_{refl}, for which associations with vascular compliance, vascular resistance and PWV were demonstrated in Chapter 3. TI_{TCD} was calculated for TCD MCA blood flow velocity data along with the currently used indices of PI_{TCD} and AI_{TCD} on two different datasets containing vascular health data such as age, CRF and PI_{MRI}. The new TI_{TCD}

outperformed the existing AI_{TCD} and PI_{TCD} in terms of correlations with CRF and PI_{MRI}. It had a similar correlation with age as did AI_{TCD}, which was much higher than the correlation of PI_{TCD} with age. In addition, based on data from an aged sample with high CRF levels, it was hypothesized that, unlike AI_{TCD}, TI_{TCD} is a predictor of vascular health independent of age.

In Chapter 5 we considered the suitability of a new imaging technology, near-infrared spectroscopy, for indexing vascular health. Firstly, a mathematical model of NiRS signals was proposed. The proposed model incorporates various elements of NiRS signals such as LF components, AP signals, reflected waves, and Mayer and respiratory waves, and is capable of producing synthetic personalized NiRS data. The CFEn regularity measure was used to assess model performance in a resting-state dataset, and synthetic HRF was added to simulate brain activation and compare it with in-vivo recordings. The purpose of the proposed model was, first, to provide a ground-truth NiRS signal that can facilitate the assessment of new and existing NiRS signal processing algorithms. Second, it can help to better understand the components of NiRS signals to inform the design of a new NiRS-based cerebrovascular health index. Later in this chapter, we proposed a NiRS peak-detection algorithm and, using synthetic signals, we examined the effects of system parameters on the accuracy of the algorithm's results. Finally, we used the model and peak-detection algorithm to examine the application of TI, AI and PI indices in the context of NiRS signals.

In Chapter 6, motivated by the results of Chapter 5, a new near-infrared spectroscopy timing index (TI_{NiRS}) of cerebrovascular health was assessed in a volunteer population. It should be mentioned that indexing cerebrovascular health with NiRS is a new approach. Only a single approach to indexing vascular compliance existed previously, called PReFx. The TI_{NiRS} is based on a similar concept as TI_{TCD}, which was introduced in Chapter 4. That is, the inverse of the time difference between the systolic and reflected peaks. The peak detection algorithm of Chapter 5 was used to locate the peaks/inflection points on the NiRS signals. The TI_{NiRS} showed significant correlations with other factors of vascular ageing including CRF, age, AI_{TCD} and PI_{MRI}, whereas the existing PReFx index did not.

7.2 Significance

Vascular stiffening is an important health indicator linked with stroke, cognitive decline and age-related disabilities, making it particularly relevant in aged populations. The stiffness of cerebral arteries is commonly estimated using an index of blood haemodynamics. In this thesis, a new timing index (TI) was proposed. Through a TL-based mathematical model of the arterial system, it was shown that TI is related to both

PWV (which is the gold standard measure of vascular stiffness in the aorta) and vascular resistance and compliance. The TI was then applied to TCD MCA blood flow velocity waveforms and showed better overall performance than existing indices (AI and PI) in terms of correlating with cerebrovascular health indicators. Then, TI was applied to NiRS blood volume measurements, for which high levels of noise and different channel-to-channel signal power levels make amplitude-based indices less reliable. The TI was shown to be significantly correlated with age, CRF and indices derived from other brain imaging modalities. Our results indicate that TI is a strong predictor of vascular health and is potentially unaffected by factors such as HR and amplitude fluctuations, which influence existing indices independently of vascular stiffness. In addition, TI has a general definition, thereby providing a potential common ground for comparing vascular health measures across different imaging modalities.

Certain brain imaging devices that measure blood haemodynamics are used to obtain data from which indices of cerebrovascular health can be derived. MRI and TCD are the two most commonly used modalities for this purpose, whereas the capabilities of NiRS in the field of cerebrovascular health were only recently discovered. Unlike NiRS technology, MRI and TCD are either expensive and importable or operator-dependent. Therefore, NiRS can potentially overcome the current barriers to the development of inexpensive, easy-to-use devices for routine cerebrovascular health monitoring. This requires researchers to focus on the development of more advanced NiRS analysis algorithms. We believe that the proposed NiRS signal model can be an important part of this process. Also, the algorithms proposed for systolic and reflected-wave peak and inflection point detection, and subsequent derivation of the $\mathrm{TI}_{\mathrm{NiRS}}$ along with the existing PReFx index form a starting point for the development of more advanced NiRS-based cerebrovascular health measures.

7.3 Future Work

In this section we discuss opportunities for future research based on the topics covered in this thesis.

The most common TCD index reported in the literature is $\mathrm{PI}_{\mathrm{TCD}}$. However, for cases such as cerebrovascular health, $\mathrm{AI}_{\mathrm{TCD}}$ has proven to be a more reliable index. We believe that one of the reasons for the lower popularity of $\mathrm{AI}_{\mathrm{TCD}}$ in TCD studies is that although $\mathrm{PI}_{\mathrm{TCD}}$ can be easily calculated and, in many cases is a direct output of the measurement device, $\mathrm{AI}_{\mathrm{TCD}}$ calculation requires the identification of systolic and reflected peaks (the same points are required to measure the proposed $\mathrm{TI}_{\mathrm{TCD}}$, see Chapter 4). Thus, the development of algorithms for automatic and, possibly, real-time detection of TCD systolic and reflected peaks is very important to the commonplace use of $\mathrm{AI}_{\mathrm{TCD}}$ and $\mathrm{TI}_{\mathrm{TCD}}$ in the future.

As discussed in Chapter 4, based on Experiment 1, for which CRF data was available, we tracked two aged individuals with high fitness levels (see Figs 4.2 and 4.3). Based on their data, we hypothesized that, unlike AI, which is a stronger age estimator, the proposed TI can estimate cerebrovascular health independently of age. This is an important aspect because an ideal index of vascular health would not necessarily be age-dependent because lifestyle choices significantly affect individuals' vascular health over time. Therefore, further experiments on wider age ranges and trained athletes are required, which should include VO_2 Max tests to gain more exact estimates of fitness levels. This would be useful for testing the independence of the proposed TI on age.

Furthermore, studying TI values on different parts of the brain or in general on different parts of the body would contribute to better understanding of vascular health changes with ageing and intra-subject variabilities. Such spatial studies on the brain have already been carried out for PReFx, leading to interesting results linking PReFx with white matter signal abnormalities and ageing in the cortex [162]. These studies of course require larger optical devices (e.g., 128 sources and 24 detectors used in [162] compared to 32 sources and 4 detectors used in our recordings) and MRI images mapped to the optical montages.

Finally, as discussed in Chapter 2, the brain is a substantially different medium for blood flow compared to the rest of the body. Therefore, modelling wave reflections and indices such as TI, PI and AI based on measurements taken from the brain requires careful considerations of CPP (specifically, ICP) and possible pulsation/damping due to CSF. Therefore, more complex assumptions need to be made to more accurately estimate these indices inside the cerebrum. Examples of advanced cerebrovascular models are present in the literature [190, 191]. However, the use of these models requires different MRI flow measurements of arterial inflow, venous outflow and CSF pulsation in the sub-arachnoid space and to add TCD and/or NiRS measurements with accurate spatial information to the model.

Bibliography

[1] C. A. Boreham, I. Ferreira, J. W. Twisk, A. M. Gallagher, M. J. Savage, and L. J. Murray, "Cardiorespiratory fitness, physical activity, and arterial stiffness," *Hypertension*, vol. 44, no. 5, pp. 721–726, 2004.

[2] G. F. Mitchell *et al.*, "Changes in arterial stiffness and wave reflection with advancing age in healthy men and women," *Hypertension*, vol. 43, no. 6, pp. 1239–1245, 2004.

[3] C. Vlachopoulos, K. Aznaouridis, and C. Stefanadis, "Prediction of cardiovascular events and all-cause mortality with arterial stiffness: A systematic review and meta-analysis," *Journal of the American College of Cardiology*, vol. 55, no. 13, pp. 1318 – 1327, 2010.

[4] G. Mancia *et al.*, "2013 ESH/ESC Guidelines for the management of arterial hypertension: The Task Force for the management of arterial hypertension of the European Society of Hypertension (ESH) and of the European Society of Cardiology (ESC)," *European Heart Journal*, vol. 34, no. 28, pp. 2159–2219, 06 2013.

[5] K. D. Kochanek, S. L. Murphy, J. Xu, and E. Arias, "Deaths: Final data for 2017," *National Vital Statistics Reports*, vol. 69, no. 9, 2019.

[6] A. Benetos *et al.*, "Influence of age, risk factors, and cardiovascular and renal disease on arterial stiffness: clinical applications," *American Journal of Hypertension*, vol. 15, no. 12, pp. 1101–1108, 12 2002.

[7] S. Sarkar, S. Ghosh, S. K. Ghosh, and A. Collier, "Role of transcranial Doppler ultrasonography in stroke," *Postgraduate Medical Journal*, vol. 83, no. 985, pp. 683–689, 2007.

[8] E. A. Warnert, K. Murphy, J. E. Hall, and R. G. Wise, "Noninvasive assessment of arterial compliance of human cerebral arteries with short inversion time arterial spin labeling," *Journal of Cerebral Blood Flow & Metabolism*, vol. 35, no. 3, pp. 461–468, 2015.

[9] S. Purkayastha and F. Sorond, "Transcranial Doppler ultrasound: Technique and application," *Seminars in Neurology*, vol. 32, pp. 411–420, 2012.

[10] M. Fabiani *et al.*, "Taking the pulse of aging: Mapping pulse pressure and elasticity in cerebral arteries with optical methods," *Psychophysiology*, vol. 51, no. 11, pp. 1072–1088, 2014.

[11] E. D. Chan, M. M. Chan, and M. M. Chan, "Pulse oximetry: Understanding its basic principles facilitates appreciation of its limitations," *Respiratory Medicine*, vol. 107, no. 6, pp. 789 – 799, 2013.

[12] N. Westerhof, J.-W. Lankhaar, and B. E. Westerhof, "The arterial windkessel," *Medical and Biological Engineering and Computing*, vol. 47, no. 2, pp. 131–141, 2008.

[13] "Cardiovascular physiology concepts," http://www.cvphysiology.com/, 2017, accessed: 2017-09-10.

[14] G. E. McVeigh, C. W. Bratteli, D. J. Morgan, C. M. Alinder, S. P. Glasser, S. M. Finkelstein, and J. N. Cohn, "Age-related abnormalities in arterial compliance identified by pressure pulse contour analysis," *Hypertension*, vol. 33, no. 6, pp. 1392–1398, 1999.

[15] R. R. Townsend *et al.*, "Recommendations for improving and standardizing vascular research on arterial stiffness," *Hypertension*, vol. 66, no. 3, pp. 698–722, 2015.

[16] F. Alberto U., "Modifications of the cardiovascular system with aging," *The American Journal of Geriatric Cardiology*, vol. 11, no. 1, pp. 30–34, 2002.

[17] O. Vardoulis, T. Papaioannou, and N. Stergiopulos, "On the Estimation of Total Arterial Compliance from Aortic Pulse Wave Velocity," *Annals of Biomedical Engineering*, vol. 40, pp. 2619–2626, 05 2012.

[18] Y. Obata *et al.*, "The Effects of Hemodynamic Changes on Pulse Wave Velocity in Cardiothoracic Surgical Patients," *BioMed Research International*, vol. 2016, 11 2016.

[19] A. Qasem and A. Avolio, "Determination of aortic pulse wave velocity from waveform decomposition of the central aortic pressure pulse," *Hypertension*, vol. 51, no. 2, pp. 188–195, 2008.

[20] J. Singer, J. N. Trollor, B. T. Baune, P. S. Sachdev, and E. Smith, "Arterial stiffness, the brain and cognition: A systematic review," *Ageing Research Reviews*, vol. 15, pp. 16 – 27, 2014.

[21] M. E. Wagshul, P. K. Eide, and J. R. Madsen, "The pulsating brain: A review of experimental and clinical studies of intracranial pulsatility," *Fluids and Barriers of the CNS*, vol. 8, no. 1, p. 5, Jan 2011.

[22] M. Ursino, "A mathematical study of human intracranial hydrodynamics part 1—the cerebrospinal fluid pulse pressure," *Annals of Biomedical Engineering*, vol. 16, no. 4, pp. 379–401, Jul 1988.

[23] B. L. C. Wright, J. T. F. Lai, and A. J. Sinclair, "Cerebrospinal fluid and lumbar puncture: A practical review," *Journal of Neurology*, vol. 259, no. 8, pp. 1530–1545, Aug 2012.

[24] W. Hartley, "A review of electrical equivalence models for the evaluation of intracranial pulsatility," 2015.

[25] L. A. Steiner and P. J. D. Andrews, "Monitoring the injured brain: ICP and CBF," *BJA: British Journal of Anaesthesia*, vol. 97, no. 1, pp. 26–38, 2006.

[26] U. Kawoos, R. M. McCarron, C. R. Auker, and M. Chavko, "Advances in intracranial pressure monitoring and its significance in managing traumatic brain injury," *International Journal of Molecular Sciences*, vol. 16, no. 12, pp. 28 979–28 997, 2015.

[27] M. M. Poels, K. Zaccai, G. C. Verwoert, and et. al., "Arterial stiffness and cerebral small vessel disease," *Stroke*, vol. 43, no. 10, pp. 2637–2642, 2012.

[28] T. M. De Silva and F. M. Faraci, "Contributions of aging to cerebral small vessel disease," *Annual Review of Physiology*, vol. 82, no. 1, pp. 275–295, 2020.

[29] J. M. Wardlaw, C. Smith, and M. Dichgans, "Mechanisms of sporadic cerebral small vessel disease: Insights from neuroimaging," *The Lancet Neurology*, vol. 12, no. 5, pp. 483–497, 2013.

[30] A. U. Ferrari, A. Radaelli, and M. Centola, "Invited review: Aging and the cardiovascular system," *Journal of Applied Physiology*, vol. 95, no. 6, pp. 2591–2597, 2003.

[31] N. Stergiopulos, J. J. Meister, and N. Westerhof, "Simple and accurate way for estimating total and segmental arterial compliance: The pulse pressure method," *Annals of Biomedical Engineering*, vol. 22, no. 4, pp. 392–397, 1994.

[32] N. Stergiopulos *et al.*, "Evaluation of methods for estimation of total arterial compliance," *American Journal of Physiology - Heart and Circulatory Physiology*, vol. 268, no. 4, pp. H1540–H1548, 1995.

[33] Y. Shim *et al.*, "Arterial windkessel parameter estimation: A new time-domain method," *Annals of Biomedical Engineering*, vol. 22, no. 1, pp. 66–77, 1994.

[34] R. Burattini and G. Gnudi, "Computer identification of models for the arterial tree input impedance: Comparison between two new simple models and first experimental results," *Medical and Biological Engineering and Computing*, vol. 20, no. 2, pp. 134–144, 1981.

[35] W. W. Nichols, C. R. Conti, W. E. Walker, and W. R. Milnor, "Input impedance of the systemic circulation in man," *Circulation Research*, vol. 40, no. 5, pp. 451–458, 1977.

[36] W. K. Laskey, H. G. Parker, V. A. Ferrari, W. G. Kussmaul, and A. Noordergraaf, "Estimation of total systemic arterial compliance in humans," *Journal of Applied Physiology*, vol. 69, no. 1, pp. 112–119, 1990.

[37] N. Stergiopulos, B. E. Westerhof, and N. Westerhof, "Total arterial inertance as the fourth element of the windkessel model," *American Journal of Physiology - Heart and Circulatory Physiology*, vol. 276, no. 1, pp. H81–H88, 1999.

[38] Z. Liu, K. P. Brin, and F. C. Yin, "Estimation of total arterial compliance: An improved method and evaluation of current methods," *Journal of American Heart Association*, vol. 251, no. 3, pp. H588–H600, 1986.

[39] G. Zhang, J.-O. Hahn, and R. Mukkamala, "Tube-load model parameter estimation for monitoring arterial hemodynamics," *Frontiers in Physiology*, vol. 2, no. 72, pp. 1–18, 2011.

[40] A. P. Avolio, "Multi-branched model of the human arterial system," *Medical and Biological Engineering and Computing*, vol. 18, no. 6, pp. 709–718, 1980.

[41] D. M. Pozar, *Microwave engineering.* Wiley, 2012.

[42] K. Barbe, W. V. Moer, and D. Schoors, "Analyzing the windkessel model as a potential candidate for correcting oscillometric blood-pressure measurements," *IEEE Transactions on Instrumentation and Measurement*, vol. 61, no. 2, pp. 411–418, Feb 2012.

[43] J. A. de la O Serna, W. V. Moer, and K. Barbé, "Using alternating kalman filtering to analyze oscillometric blood pressure waveforms," *IEEE Transactions on Instrumentation and Measurement*, vol. 62, no. 10, pp. 2621–2628, Oct 2013.

[44] H. Xiao, M. Butlin, I. Tan, and A. Avolio, "Effects of cardiac timing and peripheral resistance on measurement of pulse wave velocity for assessment of arterial stiffness," *Scientific Reports*, Jul 2017.

[45] M. Gao, H. M. Cheng, S. H. Sung, C. H. Chen, N. B. Olivier, and R. Mukkamala, "Estimation of pulse transit time as a function of blood pressure using a nonlinear arterial tube-load model," *IEEE Transactions on Biomedical Engineering*, vol. 64, no. 7, pp. 1524–1534, July 2017.

[46] T. S. Phan *et al.*, "Aging is associated with an earlier arrival of reflected waves without a distal shift in reflection sites," *Journal of American Heart Association*, vol. 5, no. 9, 2016.

[47] T. S. Phan, J. K.-J. Li, P. Segers, and J. A. Chirinos, "Misinterpretation of the determinants of elevated forward wave amplitude inflates the role of the proximal aorta," *Journal of the American Heart Association*, vol. 5, no. 2, 2016.

[48] T. Thenappan, K. W. Prins, M. R. Pritzker, J. Scandurra, K. Volmers, and E. K. Weir, "The critical role of pulmonary arterial compliance in pulmonary hypertension," *Annals of the American Thoracic Society*, vol. 13, no. 2, pp. 276–284, Feb 2016.

[49] N. Saouti, N. Westerhof, P. Postmus, and A. Vonk-Noordegraaf, "The arterial load in pulmonary hypertension," *European Respiratory Review*, vol. 19, no. 117, pp. 197–203, 2010.

[50] D. Flück *et al.*, "Effects of aging on the association between cerebrovascular responses to visual stimulation, hypercapnia and arterial stiffness," *Frontiers in Physiology*, vol. 5, p. 49, 2014.

[51] A. Kwater, J. Gąsowski, B. Gryglewska, B. Wizner, and T. Grodzicki, "Is blood flow in the middle cerebral artery determined by systemic arterial stiffness?" *Blood Pressure*, vol. 18, no. 3, pp. 130–134, 2009.

[52] T.-Y. Xu *et al.*, "Blood Flow Pattern in the Middle Cerebral Artery in Relation to Indices of Arterial Stiffness in the Systemic Circulation," *American Journal of Hypertension*, vol. 25, no. 3, pp. 319–324, 03 2012.

[53] K. Hirata, T. Yaginuma, M. F. O'Rourke, and M. Kawakami, "Age-related changes in carotid artery flow and pressure pulses," *Stroke*, vol. 37, no. 10, pp. 2552–2556, 2006.

[54] R. Gosling and D. King, "Arterial assessment by Doppler-shift ultrasound," *Proceedings of The Royal Society of Medicine-London*, vol. 67, no. 6, pp. 447–449, 1974.

[55] J. Legarth and E. Thorup, "Characteristics of Doppler blood-velocity waveforms in a cardiovascular in vitro model i the model and the influence of pulse rate," *Scandinavian Journal of Clinical and Laboratory Investigation*, vol. 49, no. 5, p. 451–457, Jan 1989.

[56] L. Legarth and E. Thorup, "Characteristics of Doppler blood-velocity waveforms in a cardiovascular in vitro model II the influence of peripheral resistance, perfusion pressure and blood flow," *Scandinavian Journal of Clinical and Laboratory Investigation*, vol. 49, no. 5, Sep 1989.

[57] M. Altmann *et al.*, "Middle cerebral artery pulsatility index is associated with cognitive impairment in lacunar stroke," *Journal of Neuroimaging*, vol. 26, no. 4, pp. 431–435, 2016.

[58] N. de Riva, K. P. Budohoski, P. Smielewski, M. Kasprowicz, C. Zweifel, L. A. Steiner, M. Reinhard, N. Fábregas, J. D. Pickard, and M. Czosnyka, "Transcranial Doppler pulsatility index: What it is and what it isn't," *Neurocritical Care*, vol. 17, no. 1, pp. 58–66, Aug 2012.

[59] J. Hashimoto, B. E. Westerhof, and S. Ito, "Carotid flow augmentation, arterial aging, and cerebral white matter hyperintensities," *Arteriosclerosis, Thrombosis, and Vascular Biology*, vol. 38, no. 12, pp. 2843–2853, 2018.

[60] T. Tarumi *et al.*, "Cerebral hemodynamics in normal aging: Central artery stiffness, wave reflection, and pressure pulsatility," *Journal of Cerebral Blood Flow & Metabolism*, vol. 34, no. 6, pp. 971–978, 2014.

[61] M. P. Pase, N. A. Grima, C. Stough, A. Scholey, and A. Pipingas, "Association of pulsatile and mean cerebral blood flow velocity with age and neuropsychological performance," *Physiology & Behavior*, vol. 130, pp. 23 – 27, 2014.

[62] Y. Ohta *et al.*, "Increased renal resistive index in atherosclerosis and diabetic nephropathy assessed by Doppler sonography," *Journal of hypertension*, vol. 23, no. 10, pp. 1905–1911, 2005.

[63] K. S. Heffeernan, W. K. Lefferts, and J. A. Augustine, "Hemodynamic correlates of late systolic flow velocity augmentation in the carotid artery," *International Journal of Hypertension*, vol. 2013, no. 6, 2013.

[64] A. J. Webb, M. Simoni, S. Mazzucco, W. Kuker, U. Schulz, and P. M. Rothwell, "Increased cerebral arterial pulsatility in patients with leukoaraiosis," *Stroke*, vol. 43, no. 10, pp. 2631–2636, 2012.

[65] C. S. Kidwell *et al.*, "Transcranial Doppler pulsatility indices as a measure of diffuse small-vessel disease," *Journal of Neuroimaging*, vol. 11, no. 3, pp. 229–235, 7 2001.

[66] H. Foerstl, S. Biedert, and W. Hewer, "Multiinfarct and alzheimer-type dementia investigated by transcranial Doppler sonography," *Biological Psychiatry*, vol. 26, no. 6, pp. 590 – 594, 1989.

[67] I. Heliopoulos, D. Artemis, K. Vadikolias, G. Tripsianis, C. Piperidou, and G. Tsivgoulis, "Association of ultrasonographic parameters with subclinical white-matter hyperintensities in hypertensive patients," *Cardiovascular Psychiatry and Neurology*, vol. 2012, p. 616572, 2012.

[68] K. A. Freeberg, N. P. McCarty, D. R. Seals, and D. H. Craighead, "Higher maximal cardiorespiratory fitness is associated with lower cerebrovascular stiffness in healthy mid-life and older adults," *The FASEB Journal*, vol. 34, no. S1, pp. 1–1, 2020.

[69] J. Y. Kim *et al.*, "Central aortic pressure and pulsatility index in acute ischemic stroke," *Journal of Neuroimaging*, vol. 25, no. 3, pp. 438–442, 2015.

[70] W. K. Lefferts, J. P. DeBlois, B. B. Gump, and K. S. Heffernan, "Carotid artery stiffness and cerebral pulsatility in children," *Artery Research*, vol. 22, pp. 64 – 67, 2018.

[71] K. Alyakhan, C. Debert, W. A. Whitelaw, J. M. Rawling, R. Frayne, and M. J. Poulin, "Differences between middle cerebral artery blood velocity waveforms of young and postmenopausal women," *The Journal of The North American Menopause Society*, vol. 13, no. 2, pp. 303–313, 2006.

[72] E. Carrera, D.-J. Kim, G. Castellani, C. Zweifel, P. Smielewski, J. D. Pickard, P. J. Kirkpatrick, and M. Czosnyka, "Cerebral arterial compliance in patients with internal carotid artery disease," *European Journal of Neurology*, vol. 18, no. 5, pp. 711–718, 2011.

[73] E. Carrera, D.-J. Kim, G. Castellani, C. Zweifel, P. Smielewski, J. D. Pickard, and M. Czosnyka, "Effect of hyper- and hypocapnia on cerebral arterial compliance in normal subjects," *Journal of Neuroimaging*, vol. 21, no. 2, pp. 121–125, 2011.

[74] J. Birnefeld *et al.*, "Cerebral arterial pulsatility is associated with features of small vessel disease in patients with acute stroke and TIA: A 4D flow MRI study," *J Neurol*, vol. 267, no. 3, pp. 721–730, 2020.

[75] G. A. Bateman, C. R. Levi, P. Schofield, Y. Wang, and E. C. Lovett, "The venous manifestations of pulse wave encephalopathy: Windkessel dysfunction in normal aging and senile dementia," *Neuroradiology*, vol. 50, no. 6, pp. 491–497, 2008.

[76] S. H. Pahlavian, X. Wang, S. Ma, H. Zheng, M. Casey, L. M. D'Orazio, X. Shao, J. M. Ringman, H. Chui, D. J. Wang, and L. Yan, "Cerebroarterial pulsatility and resistivity indices are associated with cognitive impairment and white matter hyperintensity in elderly subjects: A phase-contrast MRI study," *Journal of Cerebral Blood Flow & Metabolism*, p. 0271678X20927101, 2020.

[77] S. Petcharunpaisan, J. Ramalho, and M. Castillo, "Arterial spin labeling in neuroimaging," *World Journal of Radiology*, vol. 2, no. 10, pp. 384–398, 2010.

[78] G. A. Bateman, C. R. Levi, P. Schofield, Y. Wang, and E. C. Lovett, "Quantitative measurement of cerebral haemodynamics in early vascular dementia and alzheimer's disease," *Journal of Clinical Neuroscience*, vol. 13, no. 5, pp. 563 – 568, 2006.

[79] M. Holmgren, A. Wåhlin, T. Dunås, J. Malm, and A. Eklund, "Assessment of cerebral blood flow pulsatility and cerebral arterial compliance with 4D flow MRI," *Journal of Magnetic Resonance Imaging*, vol. 51, no. 5, pp. 1516–1525, 2020.

[80] D. A. Boas, L. E. Campbell, and A. G. Yodh, "Scattering and imaging with diffusing temporal field correlations," *Physical Review Letters*, vol. 75, no. 9, 1995.

[81] M. N. Kim, T. Durduran, S. Frangos, and et. al., "Noninvasive measurement of cerebral blood flow and blood oxygenation using near-infrared and diffuse correlation spectroscopies in critically brain-injured adults," *Neurocritical Care*, vol. 12, no. 2, pp. 173–180, Apr 2010.

[82] D. Irwin, "Influence of tissue absorption and scattering on diffuse correlation spectroscopy blood flow measurements," diploma thesis, University of Kentucky, 2011.

[83] W. B. Baker *et al.*, "Noninvasive optical monitoring of critical closing pressure and arteriole compliance in human subjects," *Journal of Cerebral Blood Flow & Metabolism*, vol. 37, no. 8, pp. 2691–2705, 2017.

[84] J. K. Choi, M. G. Choi, J. M. Kim, and H. M. Bae, "Efficient data extraction method for near-infrared spectroscopy (NiRS) systems with high spatial and temporal resolution," *IEEE Transactions on Biomedical Circuits and Systems*, vol. 7, no. 2, pp. 169–177, Apr 2013.

[85] G. Strangman, M. A. Franceschini, and D. A. Boas, "Factors affecting the accuracy of near-infrared spectroscopy concentration calculations for focal changes in oxygenation parameters," *NeuroImage*, vol. 18, no. 4, pp. 865 – 879, 2003.

[86] C. H. Tan *et al.*, "Mapping cerebral pulse pressure and arterial compliance over the adult lifespan with optical imaging," *Plos One*, vol. 12, no. 2, 2017.

[87] H. Obrig, "NiRS in clinical neurology — a 'promising' tool?" *NeuroImage*, vol. 85, pp. 535 – 546, 2014, celebrating 20 Years of Functional Near Infrared Spectroscopy (fNiRS).

[88] C.-Y. Tse, B. A. Gordon, M. Fabiani, and G. Gratton, "Frequency analysis of the visual steady-state response measured with the fast optical signal in younger and older adults," *Biological Psychology*, vol. 85, no. 1, pp. 79 – 89, 2010.

[89] J. Diedler *et al.*, "The limitations of near-infrared spectroscopy to assess cerebrovascular reactivity: The role of slow frequency oscillations," *Anesthesia & Analgesia*, vol. 113, no. 4, pp. 849–857, 2011.

[90] A. M. Chiarelli *et al.*, "Individual differences in regional cortical volumes across the life span are associated with regional optical measures of arterial elasticity," *NeuroImage*, vol. 162, pp. 199 – 213, 2017.

[91] C. H. Tan, K. A. Low *et al.*, "Optical measures of cerebral arterial stiffness are associated with white matter signal abnormalities and cognitive performance in normal aging," *Neurobiology of Aging*, vol. 84, pp. 200 – 207, 2019.

[92] A. M. Chiarelli *et al.*, "Assessment of cerebrovascular development and intraventricular hemorrhages in preterm infants with optical measures of the brain arterial pulse wave," *Journal of Cerebral Blood Flow & Metabolism*, vol. 39, no. 3, pp. 466–480, 2019.

[93] A. M. Chiarelli, K. A. Low *et al.*, "The optical effective attenuation coefficient as an informative measure of brain health in aging," *Photonics*, vol. 6, no. 3, p. 79, Jul 2019.

[94] G. Gratton, A. M. Chiarelli, and M. Fabiani, "From brain to blood vessels and back: A noninvasive optical imaging approach," *Neurophotonics*, vol. 4, no. 3, pp. 1 – 10, 2017.

[95] A. A. Laogun and R. G. Gosling, "In vivo arterial compliance in man," *Clinical physics and physiological measurement*, vol. 3, no. 3, pp. 201–212, 1982.

[96] J. Singer, J. N. Trollor, B. T. Baune, P. S. Sachdev, and E. Smith, "Arterial stiffness, the brain and cognition: A systematic review," *Ageing Research Reviews*, vol. 15, pp. 16 – 27, 2014.

[97] P. Lacolley, V. Regnault, P. Segers, and S. Laurent, "Vascular smooth muscle cells and arterial stiffening: Relevance in development, aging, and disease," *Physiological Reviews*, vol. 97, no. 4, pp. 1555–1617, 2017.

[98] S. J. Lucas, J. D. Cotter, P. Brassard, and D. M. Bailey, "High-intensity interval exercise and cerebrovascular health: Curiosity, cause, and consequence," *Journal of Cerebral Blood Flow & Metabolism*, vol. 35, no. 6, pp. 902–911, 2015.

[99] S. Ahmadi-Abhari *et al.*, "Physical activity, sedentary behavior, and long term changes in aortic stiffness: The whitehall II study," *Journal of the American Heart Association*, vol. 6, no. 8, p. e005974, 2017.

[100] A. D. Brown *et al.*, "Effects of cardiorespiratory fitness and cerebral blood flow on cognitive outcomes in older women," *Neurobiology of Aging*, vol. 31, no. 12, pp. 2047 – 2057, 2010.

[101] B. A. Kingwell, K. L. Berry, J. D. Cameron, G. L. Jennings, and A. M. Dart, "Arterial compliance increases after moderate-intensity cycling," *American Journal of Physiology-Heart and Circulatory Physiology*, vol. 273, no. 5, pp. H2186–H2191, 1997.

[102] H.-Y. Lee and B.-H. Oh, "Aging and arterial stiffness," *Circulation Journal*, vol. 74, no. 11, pp. 2257–2262, 2010.

[103] W. W. Nicholas and M. F. O'Rourke, *McDonald's Blood Flow In Arteries: Theoretical, Experimental and Clinical Principles*, 5th ed. Hodder Arnold, 2005.

[104] M. F. O'Rourke and R. P. Kelly, "Wave reflection in the systemic circulation and its implications in ventricular function," *Journal of Hypertension*, vol. 11, no. 4, pp. 327–337, 1993.

[105] A. J. Baksi *et al.*, "A meta-analysis of the mechanism of blood pressure change with aging," *Journal of the American College of Cardiology*, vol. 54, no. 22, pp. 2087–2092, 2009.

[106] J. Sugawara, K. Hayashi, and H. Tanaka, "Distal shift of arterial pressure wave reflection sites with aging," *Hypertension*, vol. 56, no. 5, pp. 920–925, 2010.

[107] Y. Zhang, Y. Zheng, Z. Ma, and S. Y., "Radial pulse transit time is an index of arterial stiffness," *Hypertension Research*, vol. 34, no. 7, pp. 884–887, 2011.

[108] J. P. Murgo, N. Westerhof, J. P. Giolma, and S. A. Altobelli, "Aortic input impedance in normal man: Relationship to pressure wave forms." *Circulation*, vol. 62, no. 1, pp. 105–116, 1980.

[109] R. D. Latham, N. Westerhof, P. Sipkema, B. J. Rubal, P. Reuderink, and J. P. Murgo, "Regional wave travel and reflections along the human aorta: A study with six simultaneous micromanometric pressures." *Circulation*, vol. 72, no. 6, pp. 1257–1269, 1985.

[110] P. Segers *et al.*, "Assessment of pressure wave reflection: Getting the timing right!" *Physiological Measurement*, vol. 28, no. 9, pp. 1045–1056, aug 2007.

[111] C. M. McEniery, Yasmin, I. R. Hall, A. Qasem, I. B. Wilkinson, and J. R. Cockcroft, "Normal vascular aging: Differential effects on wave reflection and aortic pulse wave velocity: The Anglo-Cardiff Collaborative Trial (ACCT)," *Journal of the American College of Cardiology*, vol. 46, no. 9, pp. 1753 – 1760, 2005.

[112] W. W. Nicholas and B. M. Singh, "Augmentation index as a measure of peripheral vascular disease state," *Current Opinion in Cardiology*, vol. 17, no. 5, pp. 543–551, 9 2002.

[113] J. P. Lekakis, N. A. Zakopoulos, A. D. Protogerou, T. G. Papaioannou, V. T. Kotsis, V. C. Pitiriga, M. D. Tsitsirikos, K. S. Stamatelopoulos, C. M. Papamichael, and M. E. Mavrikakis, "Arterial stiffness assessed by pulse wave analysis in essential hypertension: Relation to 24-h blood pressure profile," *International Journal of Cardiology*, vol. 102, no. 3, pp. 391 – 395, 2005.

[114] B. E. Westerhof and N. Westerhof, "Magnitude and return time of the reflected wave: The effects of large artery stiffness and aortic geometry," *Journal of Hypertension*, vol. 30, no. 5, pp. 932–939, 2012.

[115] B. E. Westerhof, J. P. van den Wijngaard, J. P. Murgo, and N. Westerhof, "Location of a reflection site is elusive," *Hypertension*, vol. 52, no. 3, pp. 478–483, 2008.

[116] M. F. O'Rourke and W. W. Nichols, "Changes in wave reflection with advancing age in normal subjects," *Hypertension*, vol. 44, no. 6, pp. E10–E11, 2004.

[117] R. Burattini and K. B. Campbell, "Effective distributed compliance of the canine descending aorta estimated by modified T-tube model." *The American journal of physiology*, vol. 264 6 Pt 2, pp. H1977–87, 1993.

[118] B. E. Westerhof and N. Westerhof, "Uniform tube models with single reflection site do not explain aortic wave travel and pressure wave shape," *Physiological Measurement*, vol. 39, no. 12, p. 124006, dec 2018.

[119] A. Mousavi *et al.*, "Tapered vs. uniform tube-load modeling of blood pressure wave propagation in human aorta," *Frontiers in Physiology*, vol. 10, p. 974, 2019.

[120] J. E. Davies *et al.*, "Attenuation of wave reflection by wave entrapment creates a horizon effect in the human aorta," *Hypertension*, vol. 60, no. 3, pp. 778–785, 2012.

[121] K. Kohara *et al.*, "Radial augmentation index: A useful and easily obtainable parameter for vascular aging," *American Journal of Hypertension*, vol. 18, no. S1, pp. 11S–14S, 01 2005.

[122] R. Kelly, C. Hayward, A. Avolio, and M. O'Rourke, "Noninvasive determination of age-related changes in the human arterial pulse." *Circulation*, vol. 80, no. 6, pp. 1652–1659, 1989.

[123] F. Fantin, A. Mattocks, C. J. Bulpitt, W. Banya, and C. Rajkumar, "Is augmentation index a good measure of vascular stiffness in the elderly?" *Age and Ageing*, vol. 36, no. 1, pp. 43–48, 11 2006.

[124] I. Wilkinson, S. Fuchs, I. Jansen, J. Spratt, G. Murray, J. Cockcroft, and D. Webb, "Reproducibility of pulse wave velocity and augmentation index measured by pulse wave analysis," *Journal of Hypertension*, vol. 16, no. 12, pp. 2079–2084, 1998.

[125] H. D. Sesso *et al.*, "Systolic and diastolic blood pressure, pulse pressure, and mean arterial pressure as predictors of cardiovascular disease risk in men," *Hypertension*, vol. 36, no. 5, pp. 801–807, 2000.

[126] N. Bjarnegård, C. Bengtsson, J. Brodszki, G. Sturfelt, O. Nived, and T. Länne, "Increased aortic pulse wave velocity in middle aged women with systemic lupus erythematosus," *Lupus*, vol. 15, no. 10, pp. 644–650, 2006.

[127] P. Segers *et al.*, "Noninvasive (input) impedance, pulse wave velocity, and wave reflection in healthy middle-aged men and women," *Hypertension*, vol. 49, no. 6, pp. 1248–1255, 2007.

[128] S. S. Franklin, W. Gustin, N. D. Wong, M. G. Larson, M. A. Weber, W. B. Kannel, and D. Levy, "Hemodynamic patterns of age-related changes in blood pressure," *Circulation*, vol. 96, no. 1, pp. 308–315, 1997.

[129] E. R. Gozna, A. E. Marble, A. Shaw, and J. G. Holland, "Age-related changes in the mechanics of the aorta and pulmonary artery of man." *Journal of Applied Physiology*, vol. 36, no. 4, pp. 407–411, 1974.

[130] A. P. Avolio, S. G. Chen, R. P. Wang, C. L. Zhang, M. F. Li, and M. F. O'Rourke, "Effects of aging on changing arterial compliance and left ventricular load in a northern chinese urban community." *Circulation*, vol. 68, no. 1, pp. 50–58, 1983.

[131] M. Willemet and J. Alastruey, "Arterial pressure and flow wave analysis using time-domain 1-D hemodynamics," *Annals of Biomedical Engineering*, vol. 43, no. 1, pp. 190–206, Jan 2015.

[132] H. Shima, K. Ohno, K. ich Michi, K. Egawa, and R. Takiguchi, "An anatomical study on the forearm vascular system," *Journal of Cranio-Maxillofacial Surgery*, vol. 24, no. 5, pp. 293 – 299, 1996.

[133] G. London, A. Guerin, B. Pannier, S. Marchais, A. Benetos, and M. Safar, "Increased systolic pressure in chronic uremia. role of arterial wave reflections." *Hypertension*, vol. 20, no. 1, pp. 10–19, 1992.

[134] J. Nurnberger *et al.*, "Augmentation index is associated with cardiovascular risk," *Journal of Hypertension*, vol. 20, no. 12, pp. 2407–2414, 2002.

[135] G. M. London, B. Pannier, and M. E. Safar, "Arterial stiffness gradient, systemic reflection coefficient, and pulsatile pressure wave transmission in essential hypertension," *Hypertension*, vol. 74, no. 6, pp. 1366–1372, 2019.

[136] I. B. Wilkinson, H. MacCallum, P. C. Hupperetz, C. J. van Thoor, J. R. Cockcroft, and D. J. Webb, "Changes in the derived central pressure waveform and pulse pressure in response to angiotensin ii and noradrenaline in man," *The Journal of Physiology*, vol. 530, no. 3, pp. 541–550, 2001.

[137] I. B. Wilkinson, H. MacCallum, L. Flint, J. R. Cockcroft, D. E. Newby, and D. J. Webb, "The influence of heart rate on augmentation index and central arterial pressure in humans," *The Journal of Physiology*, vol. 525, no. 1, pp. 263–270, 2000.

[138] K. Takazawa, N. Tanaka, K. Takeda, F. Kurosu, and C. Ibukiyama, "Underestimation of vasodilator effects of nitroglycerin by upper limb blood pressure," *Hypertension*, vol. 26, no. 3, pp. 520–523, 1995.

[139] W. W. Nichols *et al.*, "Effects of age on ventricular-vascular coupling," *American Journal of Cardiology*, vol. 55, pp. 1179–1184, 1985.

[140] S. Purkayastha and F. Sorond, "Transcranial Doppler ultrasound: Technique and application," *Seminars in Neurology*, vol. 32, no. 4, pp. 411–420, 2012.

[141] M. Czosnyka, H. K. Richards, H. E. Whitehouse, and J. D. Pickard, "Relationship between transcranial Doppler-determined pulsatility index and cerebrovascular resistance: An experimental study," *Journal of Neurosurgery*, vol. 84, no. 1, pp. 79–84, 1996.

[142] L. A. Lipsitz, S. Mukai, J. Hamner, M. Gagnon, and V. Babikian, "Dynamic regulation of middle cerebral artery blood flow velocity in aging and hypertension," *Stroke*, vol. 31, no. 8, pp. 1897–1903, 2000.

[143] H.-Y. Hsu, C.-M. Chern, J.-S. Kuo, T. B.-J. Kuo, Y.-T. Chen, and H.-H. Hu, "Correlations among critical closing pressure, pulsatility index and cerebrovascular resistance," *Ultrasound in Medicine & Biology*, vol. 30, no. 10, pp. 1329 – 1335, 2004.

[144] L. A. Calviello *et al.*, "Estimation of pulsatile cerebral arterial blood volume based on transcranial Doppler signals," *Medical Engineering & Physics*, vol. 74, pp. 23 – 32, 2019.

[145] G. F. Mitchell *et al.*, "Arterial stiffness, pressure and flow pulsatility and brain structure and function: The Age, Gene/Environment Susceptibility – Reykjavik Study," *Brain*, vol. 134, no. 11, pp. 3398–3407, 11 2011.

[146] M. Vyas *et al.*, "Augmentation Index and Central Aortic Stiffness in Middle-Aged to Elderly Individuals," *American Journal of Hypertension*, vol. 20, no. 6, pp. 642–647, 06 2007.

[147] J. Ramalho and M. Castillo, *Vascular Imaging of the Central Nervous System: Physical Principles, Clinical Applications, and Emerging Techniques.* Wiley-Blackwell, 2014.

[148] R. Wong *et al.*, "Cognitive dysfunction is associated with abnormal responses in cerebral blood flow in patients with single ventricular physiology: Novel insights from transcranial Doppler ultrasound," *Congenital Heart Disease*, vol. 14, no. 4, pp. 638–644, 2019.

[149] R. S. Nealon *et al.*, "Impaired cerebrovascular responsiveness and cognitive performance in adults with type 2 diabetes," *Journal of Diabetes and its Complications*, vol. 31, no. 2, pp. 462 – 467, 2017.

[150] G. Bateman, "Pulse-wave encephalopathy: A comparative study of the hydrodynamics of leukoaraiosis and normal-pressure hydrocephalus," *Neuroradiology*, vol. 44, no. 9, pp. 740–748, Sep 2002.

[151] R. Jurca *et al.*, "Assessing cardiorespiratory fitness without performing exercise testing," *American Journal of Preventive Medicine*, vol. 29, no. 3, pp. 185–193, 2005.

[152] R. Aaslid, T. Lundar, K. Lindegaard, and H. Nornes, "Estimation of cerebral perfusion pressure from arterial blood pressure and transcranial Doppler recordings," *Intracranial Pressure VI*, pp. 226–229, 1986.

[153] G. V. Varsos, M. Kasprowicz, P. Smielewski, and M. Czosnyka, "Model-based indices describing cerebrovascular dynamics," *Neurocritical Care*, vol. 20, no. 1, pp. 142–157, Feb 2014.

[154] R. Ghorbani Afkhami and S. J. Johnson, "Wave reflection: More than a "round trip"," *medRxiv*, 2020, [Last Accessed: Dec 20th 2020].

[155] C. D. Gatzka *et al.*, "Correction of carotid augmentation index for heart rate in elderly essential hypertensives," *American Journal of Hypertension*, vol. 14, no. 6, pp. 573–577, 06 2001.

[156] M. Masuda *et al.*, "Evaluation of blood flow velocity waveform in common carotid artery using multi-branched arterial segment model of human arteries," *Biomedical Signal Processing and Control*, vol. 8, no. 6, pp. 509 – 519, 2013.

[157] P. E. McSharry, G. D. Clifford, L. Tarassenko, and L. A. Smith, "A dynamical model for generating synthetic electrocardiogram signals," *IEEE Transactions on Biomedical Engineering*, vol. 50, no. 3, pp. 289–294, March 2003.

[158] V. Barrès, A. Simons, and M. Arbib, "Synthetic event-related potentials: A computational bridge between neurolinguistic models and experiments," *Neural Networks*, vol. 37, pp. 66 – 92, 2013.

[159] T. E. Lund, K. H. Madsen, K. Sidaros, W.-L. Luo, and T. E. Nichols, "Non-white noise in fMRI: Does modelling have an impact?" *NeuroImage*, vol. 29, no. 1, pp. 54 – 66, 2006.

[160] S. Prince, V. Kolehmainen, J. P. Kaipio, M. A. Franceschini, D. Boas, and S. R. Arridge, "Time-series estimation of biological factors in optical diffusion tomography," *Physics in Medicine and Biology*, vol. 48, no. 11, pp. 1491–1504, may 2003.

[161] G. Themelis *et al.*, "NiRS measurement of the pulsatile component of cerebral blood flow and volume from the arterial oscillations," in *Biomedical Optics*. Optical Society of America, 2006, p. SH26.

[162] C. H. Tan *et al.*, "Optical measures of cerebral arterial stiffness are associated with white matter signal abnormalities and cognitive performance in normal aging," *Neurobiology of Aging*, 2019.

[163] T. Weber *et al.*, "Wave reflections, assessed with a novel method for pulse wave separation, are associated with end-organ damage and clinical outcomes," *Hypertension*, vol. 60, no. 2, pp. 534–541, 2012.

[164] A. D. Hughes and K. H. Parker, "Forward and backward waves in the arterial system: Impedance or wave intensity analysis?" *Medical & Biological Engineering & Computing*, vol. 47, no. 2, p. 207, Feb 2009.

[165] L. R. John, "Forward electrical transmission line model of the human arterial system," *Medical and Biological Engineering and Computing*, vol. 42, no. 3, pp. 312–321, May 2004.

[166] L. Mason, *Signal processing methods for non-invasive respiration monitoring.* University of Oxford Oxford, 2002.

[167] T. J. Huppert, S. G. Diamond, M. A. Franceschini, and D. A. Boas, "HomER: A review of time-series analysis methods for near-infrared spectroscopy of the brain," *Appl Opt*, vol. 48, no. 10, pp. D280–298, Apr 2009.

[168] M. A. Yücel, J. Selb, C. M. Aasted, P. Lin, D. Borsook, L. Becerra, and D. A. Boas, "Mayer waves reduce the accuracy of estimated hemodynamic response functions in functional near-infrared spectroscopy," *Biomed. Opt. Express*, vol. 7, no. 8, pp. 3078–3088, Aug 2016.

[169] R. Cooper, L. Gagnon, D. M. Goldenholz, D. A. Boas, and D. N. Greve, "The utility of near-infrared spectroscopy in the regression of low-frequency physiological noise from functional magnetic resonance imaging data," *NeuroImage*, vol. 59, no. 4, pp. 3128 – 3138, 2012.

[170] G. H. Glover, "Deconvolution of impulse response in event-related BOLD fMRI," *NeuroImage*, vol. 9, no. 4, pp. 416 – 429, 1999.

[171] M. A. Lindquist and T. D. Wager, "Validity and power in hemodynamic response modeling: A comparison study and a new approach," *Human Brain Mapping*, vol. 28, no. 8, pp. 764–784, 2007.

[172] I. Schelkanova and V. Toronov, "Optimal quantitation of the cerebral hemodynamic response in functional near-infrared spectroscopy," *Opt. Express*, vol. 18, no. 18, pp. 19 386–19 395, Aug 2010.

[173] A. M. Chiarelli, E. L. Maclin, M. Fabiani, and G. Gratton, "A kurtosis-based wavelet algorithm for motion artifact correction of fNiRS data," *NeuroImage*, vol. 112, pp. 128 – 137, 2015.

[174] F. Scholkmann, T. Hafner, A. J. Metz, M. Wolf, and U. Wolf, "Effect of short-term colored-light exposure on cerebral hemodynamics and oxygenation, and systemic physiological activity," *Neurophotonics*, vol. 4, no. 4, pp. 1 – 13, 2017.

[175] W. Chen, Z. Wang, H. Xie, and W. Yu, "Characterization of surface EMG signal based on fuzzy entropy," *IEEE Transactions on Neural Systems and Rehabilitation Engineering*, vol. 15, no. 2, pp. 266–272, June 2007.

[176] H. Xie, Y. Zheng, J. Guo, and X. Chen, "Cross-fuzzy entropy: A new method to test pattern synchrony of bivariate time series," *Information Sciences*, vol. 180, no. 9, pp. 1715 – 1724, 2010.

[177] J. S. Richman and J. R. Moorman, "Physiological time-series analysis using approximate entropy and sample entropy," *American Journal of Physiology-Heart and Circulatory Physiology*, vol. 278, no. 6, pp. H2039–H2049, 2000.

[178] S. M. Pincus and A. L. Goldberger, "Physiological time-series analysis: What does regularity quantify?" *American Journal of Physiology-Heart and Circulatory Physiology*, vol. 266, no. 4, pp. H1643–H1656, 1994.

[179] J. F. Restrepo, G. Schlotthauer, and M. E. Torres, "Maximum approximate entropy and r threshold: A new approach for regularity changes detection," *Physica A: Statistical Mechanics and its Applications*, vol. 409, pp. 97 – 109, 2014.

[180] R. G. Afkhami, K. Low, F. Walker, and S. Johnson, "A dynamic model of synthetic resting-state brain hemodynamics," in *2018 26th European Signal Processing Conference (EUSIPCO)*, Sep. 2018, pp. 96–100.

[181] X. Cui, S. Bray, and A. L. Reiss, "Functional near infrared spectroscopy (NiRS) signal improvement based on negative correlation between oxygenated and deoxygenated hemoglobin dynamics," *NeuroImage*, vol. 49, no. 4, pp. 3039 – 3046, 2010.

[182] X. Cui, "Sample NiRS finger tapping data," 2019, http://www.alivelearn.net/?p=1621.

[183] K. Hodgkins, "Fitbit heart rate data shows which people have the best cardiac health," 2018, https://www.digitaltrends.com/health-fitness/fitbit-resting-heart-rate-study/ [Last Accessed: July 8th 2020].

[184] T. Opthof, "The normal range and determinants of the intrinsic heart rate in man," *Cardiovascular Research*, vol. 45, no. 1, pp. 177–184, 01 2000.

[185] R. G. Afkhami, R. Wong, S. Ramadan, F. R. Walker, and S. Johnson, "Indexing cerebrovascular health using Transcranial Doppler ultrasound," *MedRxiv*, 2020.

[186] University of Illinois, "University of illinois cognitive neuroimaging laboratory optical brain imaging software," 2017, [Last Accessed: March 23rd 2020]. [Online]. Available: https://www.nitrc.org/projects/uofi-cnl-opt/

[187] E. Patvardhan, K. S. Heffernan, J. Ruan, M. Hession, P. Warner, R. H. Karas, and J. T. Kuvin, "Augmentation index derived from peripheral arterial tonometry correlates with cardiovascular risk factors," *Cardiology Research and Practice*, vol. 2011, 2011.

[188] M. Nirmalan and P. M. Dark, "Broader applications of arterial pressure wave form analysis," *Continuing Education in Anaesthesia Critical Care & Pain*, vol. 14, no. 6, pp. 285–290, 02 2014.

[189] M. Reisner, Andrew, P. Shaltis, Phillip A., D. McCombie, and P. Asada, H Harry, "Utility of the Photoplethysmogram in Circulatory Monitoring," *Anesthesiology: The Journal of the American Society of Anesthesiologists*, vol. 108, no. 5, pp. 950–958, 05 2008.

[190] K. Ambarki, O. Baledent, G. Kongolo, R. Bouzerar, S. Fall, and M. E. Meyer, "A new lumped-parameter model of cerebrospinal hydrodynamics during the cardiac cycle in healthy volunteers," *IEEE Transactions on Biomedical Engineering*, vol. 54, no. 3, pp. 483–491, March 2007.

[191] J. Kim, N. Thacker, P. Bromiley, and A. Jackson, "Prediction of the jugular venous waveform using a model of CSF dynamics," *American Journal of Neuroradiology*, vol. 28, no. 5, pp. 983–989, 2007.